Article

Brain-wide cell-type-specific transcriptomic signatures of healthy ageing in mice

https://doi.org/10.1038/s41586-024-08350-8

Received: 10 July 2023

Accepted: 6 November 2024

Published online: 1 January 2025

Open access

Check for updates

Kelly Jin[1], Zizhen Yao[1], Cindy T. J. van Velthoven[1], Eitan S. Kaplan[1], Katie Glattfelder[1], Samuel T. Barlow[1], Gabriella Boyer[1], Daniel Carey[1], Tamara Casper[1], Anish Bhaswanth Chakka[1], Rushil Chakrabarty[1], Michael Clark[1], Max Departee[1], Marie Desierto[1], Amanda Gary[1], Jessica Gloe[1], Jeff Goldy[1], Nathan Guilford[1], Junitta Guzman[1], Daniel Hirschstein[1], Changkyu Lee[1], Elizabeth Liang[1], Trangthanh Pham[1], Melissa Reding[1], Kara Ronellenfitch[1], Augustin Ruiz[1], Josh Sevigny[1], Nadiya Shapovalova[1], Lyudmila Shulga[1], Josef Sulc[1], Amy Torkelson[1], Herman Tung[1], Boaz Levi[1], Susan M. Sunkin[1], Nick Dee[1], Luke Esposito[1], Kimberly A. Smith[1], Bosiljka Tasic[1]✉ & Hongkui Zeng[1]✉

Biological ageing can be defined as a gradual loss of homeostasis across various aspects of molecular and cellular function[1,2]. Mammalian brains consist of thousands of cell types[3], which may be differentially susceptible or resilient to ageing. Here we present a comprehensive single-cell RNA sequencing dataset containing roughly 1.2 million high-quality single-cell transcriptomes of brain cells from young adult and aged mice of both sexes, from regions spanning the forebrain, midbrain and hindbrain. High-resolution clustering of all cells results in 847 cell clusters and reveals at least 14 age-biased clusters that are mostly glial types. At the broader cell subclass and supertype levels, we find age-associated gene expression signatures and provide a list of 2,449 unique differentially expressed genes (age-DE genes) for many neuronal and non-neuronal cell types. Whereas most age-DE genes are unique to specific cell types, we observe common signatures with ageing across cell types, including a decrease in expression of genes related to neuronal structure and function in many neuron types, major astrocyte types and mature oligodendrocytes, and an increase in expression of genes related to immune function, antigen presentation, inflammation, and cell motility in immune cell types and some vascular cell types. Finally, we observe that some of the cell types that demonstrate the greatest sensitivity to ageing are concentrated around the third ventricle in the hypothalamus, including tanycytes, ependymal cells, and certain neuron types in the arcuate nucleus, dorsomedial nucleus and paraventricular nucleus that express genes canonically related to energy homeostasis. Many of these types demonstrate both a decrease in neuronal function and an increase in immune response. These findings suggest that the third ventricle in the hypothalamus may be a hub for ageing in the mouse brain. Overall, this study systematically delineates a dynamic landscape of cell-type-specific transcriptomic changes in the brain associated with normal ageing that will serve as a foundation for the investigation of functional changes in ageing and the interaction of ageing and disease.

Defining and distinguishing global, region-specific and cell-type-specific functional changes with ageing is an essential step towards understanding the normal ageing process as well as the interaction between normal ageing and disease pathology. In the past decade, there have been concerted efforts to document and catalogue various molecular and cellular hallmarks of ageing that are conserved across different model systems[1,2]. Emerging studies of brain ageing and neurodegeneration are beginning to reveal the presence of some of these hallmarks of ageing across the brain, including chronic inflammation mediated by microglia and other glial types in the brain[4,5], aberrant neuronal network activity[6,7], cellular senescence[8] and others[1]. Although these hallmarks provide a crucial foundational understanding of how individual cells age, our understanding of how a multicellular tissue as complex and heterogeneous as the brain ages is still rudimentary. We have barely begun to uncover the cellular hallmarks of ageing at the cell-type level, and how these changes ultimately contribute to the decline in health of the entire organism.

In recent years, several studies profiled transcriptomic changes during normal ageing across broad regions of the mouse brain at single-cell level[9,10], and many studies profiled more targeted, specific regions or

[1]Allen Institute for Brain Science, Seattle, WA, USA. ✉e-mail: bosiljkat@alleninstitute.org; hongkuiz@alleninstitute.org

cell types[4,11–17]. Whereas these studies varied in approach and scale, they consistently demonstrated heterogeneity in the age-associated transcriptomic changes among cell types. As such, detailed annotation and interrogation of all cell types in the brain will be crucial to fully characterize how different cell types, both neuronal and non-neuronal, change and interact with one another during ageing. Most recently, scaling single-cell transcriptomic approaches to the whole mouse brain has allowed us to define cell types in the brain at an unprecedented resolution and comprehensiveness, revealing the tremendous diversity of neuronal and non-neuronal cell types and their gene expression profiles throughout the adult mouse brain[3,18–20]. These thorough studies of the adult brain now enable a systematic and comprehensive understanding of how the brain changes with age at molecular and cellular levels.

Here we used single-cell RNA sequencing (scRNA-seq) to profile many brain regions covering major parts of the brain that have complex cell-type compositions, in young adult (2 months old) and aged (18 months old) mice in both sexes. Together, these profiled regions cover roughly 35% of the entire volume of the mouse brain, making it the highest-coverage ageing mouse brain single-cell transcriptomics dataset published to date (Extended Data Fig. 1). The dataset includes roughly 1.2 million single-cell transcriptomes after quality control (QC), which were annotated using the Allen Brain Cell–Whole Mouse Brain atlas (ABC-WMB atlas)[3]. This approach allowed us to identify 172 unique transcriptomic subclasses (which are further subdivided into 434 supertypes and 847 clusters) and to interrogate them for age-associated gene expression changes. We also generated spatial transcriptomics datasets to confirm these cell-type-specific changes in specific regions of interest (ROI).

In this study, we observe numerous cell-type-specific changes in gene expression across non-neuronal and neuronal cell types, many of which occur in sparse populations of cell types that were often overlooked in previous scRNA-seq studies, in addition to well-established signatures of brain ageing[1]. These changes include (1) depletion of certain immature neuron (IMN) types in aged tissue, (2) decreased expression of neuronal signalling and structure genes across many neurons, oligodendrocytes and astrocytes, (3) increased expression of inflammatory and immune response genes in immune cells, as well as some other non-neuronal and neuronal types and (4) extensive gene expression changes in cell types surrounding the third ventricle (V3) of the hypothalamus. The V3-associated non-neuronal and neuronal cell types expressing many age-DE genes include tanycytes, ependymal cells and neuron types in the arcuate nucleus (ARH), dorsomedial nucleus (DMH) and paraventricular nucleus (PVH) that express *Agrp*, *Npy*, *Pomc*, *Crh*, *Lepr* and *Glp1r* genes, which encode neuropeptides or neuropeptide receptors involved in feeding behaviour and energy homeostasis. Taken together, our results systematically reveal a wide range of cell-type-specific patterns of ageing, identify age-specific cell-type clusters that show unique gene expression changes and highlight the V3 area of the hypothalamus as a potential hot spot for brain ageing.

Brain-wide single-cell and in situ RNA profiling

We profiled 16 broadly dissected regions across the young adult (P53–69; 2 months old) and aged (P540–553; 18 months old) female and male mouse brains using the 10x Genomics Chromium platform based on version 3 chemistry (10xv3). These 16 broad regions (Fig. 1a) were selected due to their known sensitivity to age and age-associated diseases in the literature[21]. They were grouped into six major brain structures: (1) isocortex, which includes prelimbic area + infralimbic area + orbital area, agranular insular area, anterior cingulate area (ACA) and retrosplenial area (RSP); (2) hippocampal formation (HPF), which includes hippocampus, parasubiculum + postsubiculum + presubiculum + prosubiculum + subiculum, and lateral and medial entorhinal areas (ENT); (3) hypothalamus (HY); (4) cerebral nuclei (CNU), which include the dorsal and ventral striatum, pallidum and striatum-like amygdalar nuclei; (5) midbrain, which includes periaqueductal grey + midbrain raphe nuclei as well as substantia nigra + ventral tegmental area; and (6) hindbrain, which includes the anterior or posterior part of the combined pons, motor-related and behavioural state-related areas. Brain regions for profiling and boundaries for dissections were defined by the Allen Mouse Brain Common Coordinate Framework version 3 (CCFv3)[22] (Fig. 1a). On the basis of the three-dimensional volumes in CCFv3, we estimate that these 16 broad dissection regions, encompassing roughly 110 CCF-defined brain regions cover roughly 35% of all grey matter areas within the whole mouse brain.

We performed scRNA-seq from 287 unique 10xv3 libraries, collected from a total of 108 mice (Supplementary Table 1). To ensure good representation of both neurons and non-neuronal cells, we used several forms of fluorescence-activated cell sorting (FACS) and unbiased cell sampling (labelled No FACS, Methods). All neuron-enriched libraries were FACS-isolated from the pan-neuronal *Snap25-IRES2-Cre/wt;Ai14/wt* transgenic mice, whereas the unbiased libraries were isolated from a mixture of transgene-positive and -negative mice (Supplementary Table 1). Our data collection strategy is summarized in Fig. 1b, and example images of gating strategies used for FACS sorting are shown in Extended Data Fig. 2. Low-quality cell transcriptomes were removed based on a combination of QC criteria (Methods and Extended Data Fig. 3a). After the QC filtering, we obtained 1,162,565 high-quality cells, of which roughly 59% (682,987 cells) originated from aged and the rest (479,578 cells) from adult brain tissue, with little variation in quality scores between aged and adult cells for most cell classes (Extended Data Fig. 3a–d).

We performed de novo clustering of all adult and aged cells together (Methods and Extended Data Fig. 3a). All the adult cells in this study had been thoroughly annotated as part of our recent mouse whole-brain taxonomy[3], allowing us to leverage the existing cell-type annotations to help annotate the aged cells (Methods). All cells in this study have at least four levels of annotation: cell class (the broadest level of annotation), subclass, supertype and cluster. All class, subclass and supertype labels match those from the ABC-WMB atlas, whereas the cluster labels presented here are unique to this study (Fig. 1c). In subsequent analyses, we used two primary strategies to characterize cell-type-specific age-associated changes: (1) using three computational methods to identify age-DE genes at subclass, supertype and/or cluster levels and (2) performing high-resolution clustering across all cells to identify ageing-enriched or ageing-depleted clusters (Fig. 1d).

Out of the total 338 subclasses defined in the ABC-WMB atlas[3], we identified 172 unique subclasses in the combined aged and adult dataset (missing subclasses are largely from brain regions not profiled in this study). These subclasses span 25 different cell classes (Fig. 1e and Supplementary Table 2) and show specific marker gene expression (Extended Data Fig. 4). Slightly more than half of all cells in this study are non-neuronal, and their proportions vary by brain regions (Extended Data Fig. 3e). Most non-neuronal cell types are shared between brain regions, whereas neurons differ among brain regions (Fig. 1e,f). The average number of donor mice per age for all subclasses is 14 ± 11 (mean ± s.d.). Most subclasses are well balanced between ages and sexes, although not perfectly due to QC procedures at various stages in the data generation and analysis pipeline (Fig. 1e,f and Supplementary Table 2).

We collected four Molecular Cartography datasets (a form of in situ spatial RNA profiling from Resolve Biosciences) to visualize and validate results discovered by scRNA-seq. For each spatial dataset, we selected a panel of 100 genes to profile preselected region(s) in male and female mouse coronal brain sections. These four datasets span a variety of brain regions in the isocortex, hippocampus, striatum, hindbrain, midbrain and hypothalamus, and will be referred to in the remainder of the text as Resolve spatial transcriptomics experiments 1–4 (RSTE1–4, Extended Data Fig. 5).

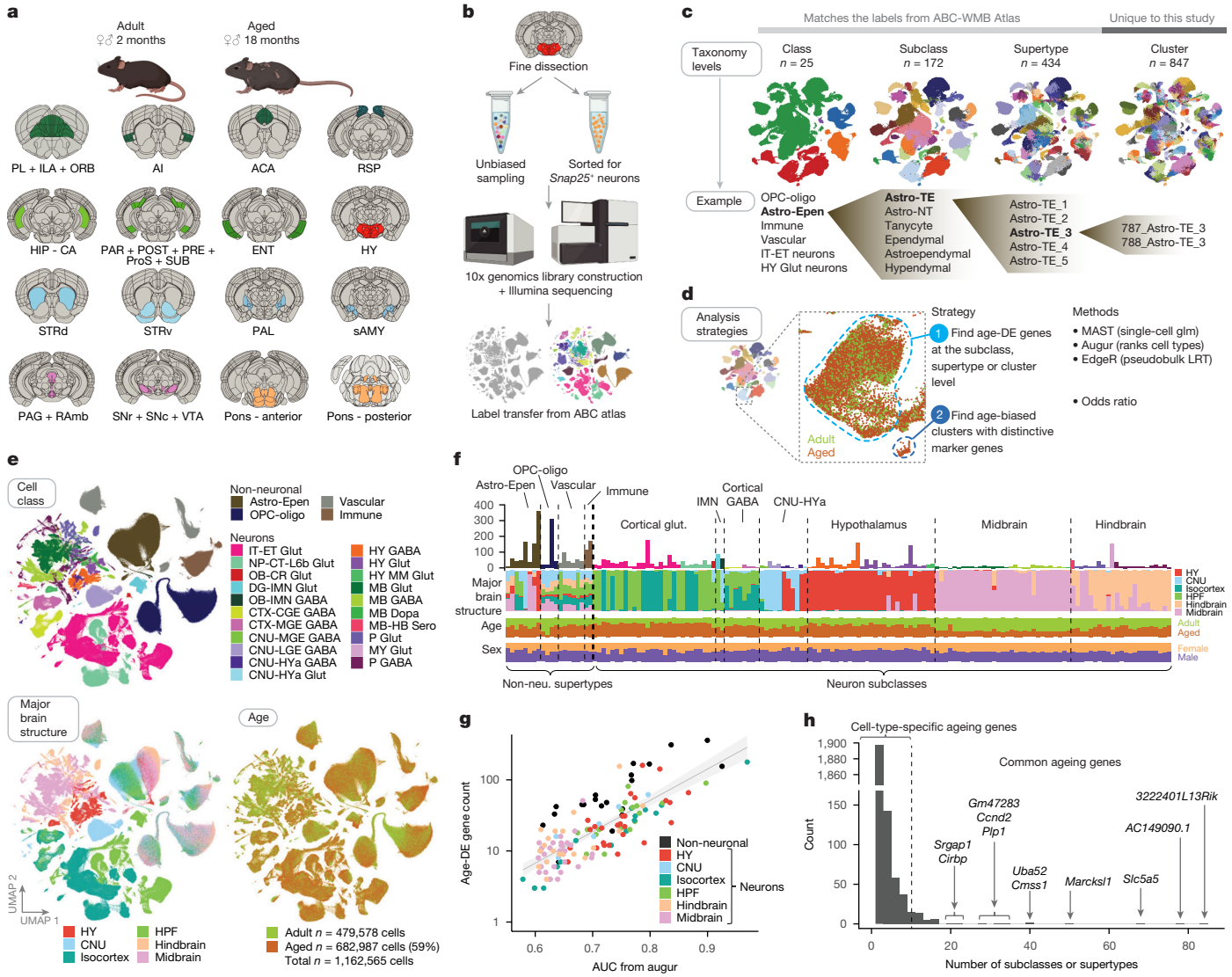

Fig. 1 | Transcriptomic cell types in young adult and aged mouse brains. **a**, Schematic of dissected brain regions profiled in this study, coloured by major brain structure. **b**, Schematic of library generation and cell annotation workflow. **c**, Diagram of cell annotation levels based on the ABC-WMB atlas. Bold text indicates the highlighted cell type that is expanded in the subsequent, finer annotation level. **d**, Schematic of general analysis strategy for identifying cell types vulnerable to ageing. **e**, UMAP representation of all single-cell transcriptomes included in this study, coloured by cell class, major brain structure and age. **f**, Summary of the number of all age-DE genes identified from each subclass (for neurons) and supertype (for non-neuronal cells). Bar graphs below age-DE gene counts represent breakdown of each group by major brain structure, age and sex. **g**, Relationship between the number of age-DE genes and Augur AUC score for all cell types represented in **f**. Linear model with 95% confidence interval of fit is shown by the light grey shading. **h**, Histogram of the number of cell types (subclasses for neurons; supertypes for non-neuronal cells) an age-DE gene is significant for. PL + ILA + ORB, prelimbic area + infralimbic area + orbital area; AI, agranular insular area; ACA, anterior cingulate area; RSP, retrosplenial area; HIP-CA, hippocampus; PAR + POST + PRE + ProS + SUB, parasubiculum + postsubiculum + presubiculum + prosubiculum + subiculum; ENT, lateral and medial entorhinal areas; HY, hypothalamus; STRd, dorsal striatum; STRv, ventral striatum; PAL, pallidum; sAMY, striatum-like amygdalar nuclei; PAG + RAmb, periaqueductal grey + midbrain raphe nuclei; SNr + SNc + VTA, substantia nigra, reticular part + substantia nigra, compact part + ventral tegmental area. Brain sections with anatomical parcellations in **a** and **b** are adapted from Allen Mouse Brain CCFv3 (https://atlas.brain-map.org/). Cartoon depictions of mice in **a** and Eppendorf tubes and laboratory instruments in **b** were created using BioRender (https://biorender.com).

Age-associated differential gene expression

To examine and model age-DE genes within different groups of cells, we primarily used model-based analysis of single-cell transcriptomics (MAST)[23] while including gene detection, QC scores and sex as covariates in the model (Methods). Age effect size, which can be interpreted as an estimate of $\log_2$(fold change) of gene expression with age, and adjusted *P* value were calculated from the model. A gene was found to be significantly differentially expressed with age if it showed an absolute (abs) age effect size greater than 1 and adjusted $P < 0.01$. Positive age effect sizes (greater than 1) roughly correspond to an increase of more than twofold in expression of that gene with ageing, whereas negative age effect sizes (below −1) roughly correspond to a decrease of more than 50%. Age effect sizes and adjusted *P* values from the MAST model for each significant gene are reported in Supplementary Table 3.

Given that non-neuronal diversity at the subclass level is less extensive compared to neurons, we began our interrogation of non-neuronal cells at the supertype level (20 supertypes total) and neurons at subclass level (132 subclasses total). We observed a wide range in numbers of age-DE genes (total unique 2,449) across all cell types, with larger numbers of age-DE genes seen in many non-neuronal types (Fig. 1f,g).

To confirm that our method of assessing age-associated changes with MAST is robust, we also conducted further analysis using (1) pseudo-bulk analysis[24], which groups scRNA-seq data into pseudo-bulk samples when performing differentially expressed gene analysis, and (2) Augur[25], a statistical method designed to prioritize cell types based on the ability to predict condition (that is, age) based on gene expression (Methods). Gene-level coefficients calculated from MAST (age effect sizes) correlated well with those calculated using the pseudo-bulk approach for most cell types (for example, Extended Data Fig. 6a,b), with a mean correlation coefficient of 0.72 for all cell types (Extended Data Fig. 6c). In addition, prediction area under the receiver-operating curve (AUC) scores from Augur correlated highly with the number of age-DE genes from MAST per supertype or subclass (Fig. 1g). Of note, there is no significant correlation between the number of age-DE genes and the number of cells in each type used for MAST analysis (Extended Data Fig. 6d). Taken together, these analyses provide greater confidence in the validity and robustness of the age-DE genes identified with MAST.

Most age-DE genes are cell-type-specific

Across all neuronal subclasses and non-neuronal supertypes, we found that most of the age-DE genes were significant in only one or two subclasses or supertypes (Fig. 1h), suggesting that most age-DE genes are cell-type specific. There are only a handful of age-DE genes with significant changes in many subclasses and/or supertypes (labelled genes in Fig. 1h), and we defined age-DE genes found in ten or more subclasses and/or supertypes as common age-DE genes (Fig. 1h and Extended Data Fig. 7).

Many common age-DE genes still show brain region and/or cell-type-specific differential expression (Extended Data Fig. 7). For example, 3222401L13Rik (a long intergenic non-coding RNA[26] surrounded by protocadherins in the genome) and *Slc5a5* are significantly upregulated in 84 and 68 types, respectively, almost all of which are midbrain, hindbrain and hypothalamic neuronal types. *AC149090.1* has increased expression with age in 78 types spanning both neuronal and glial types. *AC149090.1* is an orthologue of *Pisd*, which encodes phosphatidylserine decarboxylase, an enzyme involved in lipid metabolism[27] linked to mitochondrial disease[28]. This gene was also the top contributing gene in a recent study that built cell-type-specific transcriptomic age clocks from scRNA-seq data in the mouse SVZ[16]. There are also genes that have decreased expression with age across many subclasses. For example, *Ccnd1* and *Ccnd2*, which encode cell cycle regulator proteins cyclin D1 and D2, are downregulated in various hypothalamic neuronal subclasses, particularly those localized to the periventricular area. *Ccnd2* is also downregulated in certain cortical neurons and non-neuronal types. Altogether, these observations suggest that different cell types demonstrate unique age-associated gene expression profiles. As such, the remainder of the Results section highlights observations from individual cell types, beginning with non-neuronal types, followed by neurons and conclude with common themes observed across all cell types with age.

Ageing affects cells in adult neurogenesis niches

First, we examined age-DE genes in non-neuronal supertypes and IMN subclasses (Fig. 2a). Non-neuronal cell types are divided into four classes: (1) astrocyte and ependymal-like cell types (Astro-Epen), (2) oligodendrocytes and their precursors (OPC-Oligo), (3) vascular cells and (4) immune cells. Many Astro-Epen cell types are highly region-specific[3]. The two IMN subclasses present in our dataset are DG-PIR Ex IMN, which contains mostly IMNs from the dentate gyrus localized to the subgranular zone (SGZ) that give rise to glutamatergic dentate gyrus granule cells, and OB-STR-CTX Inh IMN, which contains IMNs originated in the subventricular zone (SVZ) that follow the rostral migratory stream and in the olfactory bulb differentiate into GABAergic granule cells.

For more abundant non-neuronal cell types, we also estimated changes in cell proportions with age in different brain structures using RSTE1 (Extended Data Fig. 8). At the more refined cluster level, to determine whether any of the clusters are age-biased (that is, composed of greater or fewer aged cells than expected by chance), we calculated odds ratio (OR) for each cluster based on the ratio of aged to adult cells within the cluster compared to the class (Methods). Clusters with $\log_2 OR < -2.5$ or $\log_2 OR > 2.5$ were considered ageing-depleted or -enriched, respectively (Fig. 2b).

We found a wide range of age-DE genes that vary widely across cell types. The supertypes with the greatest numbers of age-DE genes and the highest AUC scores from Augur include those that are closely associated with the ventricular system of the brain (Fig. 2c,d). Many of these cell types are located in known or potential regions of adult neurogenesis in the brain: the SVZ that lines the striatum, the SGZ of the dentate gyrus and the V3 of hypothalamus (Fig. 2c,d). These cells include tanycytes, ependymal cells, OB-STR-CTX Inh IMN and Astro-TE_5. Tanycytes lining V3 (Fig. 2c) are thought to have stem-cell-like activity in adulthood[29]. Astro-TE_5 is a telencephalic astrocyte supertype that specifically colocalizes with OB-STR-CTX Inh IMN in the SVZ (Fig. 2c). Gene ontology (GO) term enrichment analysis (Supplementary Table 4) across age-DE genes in these types reveals decreased expression of genes involved in regionalization, neurogenesis, and epithelium morphogenesis with ageing in OB-STR-CTX Inh IMN (Fig. 2e), whereas Astro-TE_5 shows increased expression of genes involved in cell–cell adhesion (for example, cadherin gene *Cdh19*) and ion channel activity (for example, *Grin2a* and *Grid1*) (Fig. 2f and Extended Data Fig. 9a). The top gene expression change in Astro-TE_5 is a decrease in *Csmd1* (Fig. 2f), a gene that has been associated with cognitive decline and degenerative diseases such as Parkinson's[30] as well as brain complement activity and circuit development[31].

Furthermore, we found that Astro-TE_2 and DG-PIR Ex IMN, both small populations of cells restricted to the SGZ of dentate gyrus (Fig. 2c) that share common marker genes such as *Dscaml1* and *Sox4* in contrast to other astro-TE supertypes (Fig. 2g), are more depleted with age than expected by chance (Fig. 2b). These findings suggest that neurogenesis activity in the SGZ decreases significantly by 18 months of age in mice, consistent with previous studies[32,33].

Age-DE genes in remaining astrocyte supertypes are varied (Fig. 2f) but many are enriched in GO terms associated with neuron projection development, synaptic membrane compartments and ion channel activity (Extended Data Fig. 9a). We estimated the changes in cell proportions with age for the two most abundant astrocyte supertypes in the brain, Astro-TE_3 and Astro-NT_2 (Fig. 2f). Astro-TE_3, the major astrocyte supertype in the telencephalon, does not significantly change in abundance with age, whereas Astro-NT_2, the major astrocyte supertype in non-telencephalic regions, shows a significant decrease with age in its abundance in the midbrain and hindbrain (Extended Data Fig. 8a).

Diverse responses of vascular cell types to ageing

Ageing leads to loss of integrity and function of the brain microvasculature[34,35]. We characterized age-associated changes in the vascular cell supertypes: arachnoid barrier cells (ABCs), two types of vascular leptomeningeal cells (VLMCs), endothelial cells, smooth muscle cells (SMCs) and pericytes. We observed diverse sets of age-DE genes in all vascular cell types (Fig. 2h) that show enrichment for different types of biological process and molecular function (Extended Data Fig. 9b). The GO terms indicate an upregulation of genes involved in major histocompatibility complex (MHC) class I (MHC-I) response in endothelial cells, such as histocompatibility (H2) genes *H2-Q6* and *H2-Q7*, and an upregulation of genes related to MHC class II (MHC-II) response in ABCs, for example, *Cd74*, *H2-Aa* and *H2-Ab1* (Fig. 2h). Furthermore, there is a downregulation of genes involved in collagen complex formation

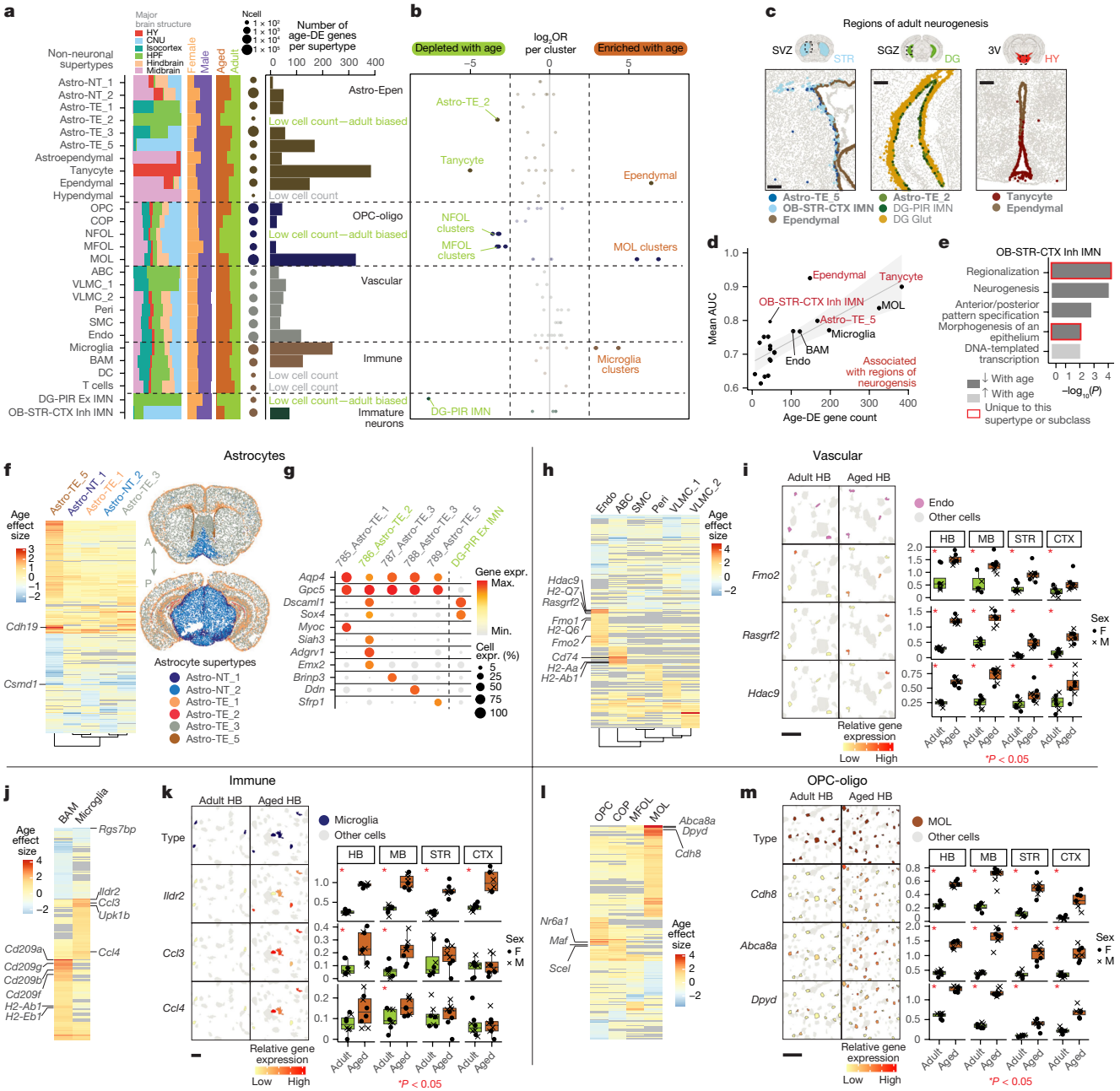

Fig. 2 | Age-DE genes across non-neuronal supertypes. a, Summary of the number of age-DE genes for each of the non-neuronal supertypes as well as two IMN subclasses, grouped by cell classes. Ncell, number of cells. **b**, The $\log_2$OR of aged versus adult cell membership of each cluster as compared to the total number of aged versus adult cell membership of the corresponding class. Each point represents one cell cluster. Rows correspond to the supertypes as labelled in **a**. **c**, Spatial localization taken from the ABC-WMB atlas MERFISH data of known and/or suspected regions of adult neurogenesis: SVZ, SGZ and V3 with major cell supertypes coloured. Brain sections with anatomical parcellations are adapted from Allen Mouse Brain CCFv3. Bold text indicates the cell types that are also highlighted in **d**. **d**, Relationship between the number of age-DE genes and Augur AUC score for each of the non-neuronal supertypes and IMN subclasses. The red colour denotes top supertypes or subclass associated with regions of neurogenesis. A linear model with a 95% confidence interval of fit is shown by the light grey shading. **e**, Select GO terms enriched in age-DE genes from OB-STR-CTX Inh IMN cells, with either increased (light grey) or decreased (dark grey) gene expression with ageing. This analysis was performed across all non-neuronal supertypes and neuronal subclasses. Terms that are unique to one cell type only are highlighted with a red border. Enriched GO terms were identified using a hypergeometric test and corrected for multiple testing as described in the Methods. **f**, Heatmap of age effect sizes of all age-DE genes that are significant in at least one Astro-TE or Astro-NT supertype, whose spatial localization is shown in brain sections taken from the ABC-WMB atlas. **g**, Dot plot of marker genes for all clusters in the Astro-TE subclass in comparison with the DG-PIR Ex IMN subclass. **h**,**j**,**l**, Heatmap of age effect sizes of all age-DE genes that are significant in at least one vascular (**h**), immune (**j**) or OPC-Oligo (**l**) supertype. **i**,**k**,**m**, Visualization and quantification of expression of *Fmo2*, *Rasgrf2* and *Hdac9* in endothelial cells (**i**), *Ildr2*, *Ccl3* and *Ccl4* in microglia (**k**) or *Cdh8*, *Abca8a* and *Dpyd* in MOL (**m**) from hindbrain (HB) of RSTE1. Significance between ages for spatial gene expression was tested using a two-sided Mann–Whitney *U*-test. Results in **i**, **k** and **m** represent $n = 4$ replicates (two biological and two technical) per sex, age and/or region examined over one experiment. Only samples with more than 20 cells of that cluster were included in the analysis, resulting in certain cell types per sex and/or age that have fewer than four replicates shown. For all boxplots, the minimum, centre and maximum bound of the box represent the 25th, 50th and 75th percentile of the data shown, respectively. The upper and lower whiskers represent the largest and smallest value within 1.5 times above or below the interquartile range, respectively. Specific sample sizes and *P* values are shown in the online source data file associated with this figure (the same for all spatial gene expression quantifications shown in other figures, as described in the Methods). DC, dendritic cell; Expr., expression; max., maximum; MB, midbrain; min., minimum. Scale bars, 200 µm (**c**), 20 µm (**i**,**k**), 50 µm (**m**).

and extracellular matrix organization in pericytes, SMCs and VLMCs (Extended Data Fig. 9b).

Endothelial cells show the greatest number of age-DE genes among all vascular types and are ranked highly with Augur (Fig. 2a,d,h). Among all endothelial age-DE genes, genes with the greatest effect sizes are *Rasgrf2* and *Hdac9*, whose increased expression was confirmed in situ (Fig. 2h,i). Increase in *Rasgrf2* expression in endothelial cells with age may act as a protective mechanism, as in human vascular endothelial cells it was suggested to act as an antiapoptotic, protective factor[36]. *Hdac9* gene upregulation was previously observed in the ischaemic brain and it exacerbated endothelial injury[37]. We also observed increased expression of *Fmo1* and *Fmo2* with age in endothelial cells (Fig. 2h,i and Extended Data Fig. 9b). Expression of human FMO genes has been correlated with various neurological diseases[38].

We detected significant loss of endothelial cells in some regions of the brain with age (Extended Data Fig. 8b). However, the loss of pericytes was more pronounced and observed in all regions profiled. This suggests that age-associated loss of brain vasculature integrity may be influenced more by loss of pericytes than other components of the neurovascular unit.

Pro-inflammatory age-enriched microglia clusters

Increased immune cell activation and dysfunction in the brain with age may be a cause or consequence of neurodegenerative pathology[39]. Owing to limited numbers of lymphoid and dendritic cells in our scRNA-seq dataset, we focused the analysis of immune cells on microglia and border-associated macrophages (BAMs), both of which show large numbers of age-DE genes and high AUC values from Augur (Fig. 2a,d).

BAMs show coordinated upregulation of many *Cd209* genes in aged mouse (Fig. 2j), which code for lectins that function in cell adhesion and pathogen recognition. An increased expression in *Cd209a* and *Cd209b* with ageing was confirmed in situ (Extended Data Fig. 9c). GO analysis uncovered upregulated terms with ageing that include *Cd209* genes, such as immune response, cell adhesion, virus receptor activity and monosaccharide binding (Extended Data Fig. 9c). We also observed upregulation of certain H2 genes that are indicative of an increase in MHC-II protein response, including *H2-Ab1* and *H2-Eb1* (Fig. 2j and Extended Data Fig. 9d).

In microglia with ageing, we observed upregulation of *Ildr2*, *Ccl3*, *Ccl4* and *Upk1b*, confirmed in situ in at least one region profiled, and downregulation of *Rgs7bp* (Fig. 2j,k and Extended Data Fig. 9e), consistent with previous single-cell studies of ageing in microglia[5,14]. *Upk1b* was included in the microglia 'sensome', a signature set of microglia genes encoding proteins that sense endogenous ligands and microbes[40]. These genes are associated with GO terms involving inflammatory response, cytokine production, NF-κB signalling, MHC-I protein complex and others (Extended Data Fig. 9f).

On further clustering of aged and adult BAMs and microglia, we identified six transcriptionally distinct clusters, five of which belong to microglia and express microglia markers including *Cx3cr1*, *P2ry12*, *Nav3* and *Trem2* (Extended Data Fig. 10a–c). The largest microglia cluster (841_Microglia) contains roughly 94% of all microglia cells and probably represents the homeostatic microglia observed in both adult and aged brains (Extended Data Fig. 10a,d). The four other microglia clusters are much smaller than cluster 841 and possibly represent different states of activated microglia. Cluster 840 is very region and sex biased, found mostly in male cerebral nuclei (specifically dorsal striatum) and uniquely expressing many genes including *Kcnd2* and *Fgf14* (Extended Data Fig. 10c,d).

We identified two ageing-enriched clusters, 842_Microglia and 843_Microglia (Extended Data Fig. 10c,d). Both clusters show increased expression of the antiapoptotic Bcl-2 family members *Bcl2a1a* and *Bcl2a1d*, which have been shown to increase in a variety of cell types with cell senescence[41], as well as increased expression of cell senescence marker *Cdkn1a* (Extended Data Fig. 10c), consistent with previous studies detecting the accumulation of senescent microglia in aged mouse brain[42,43]. In addition, we found cluster-specific markers resembling those found by Hammond et al. in their scRNA-seq study profiling microglia throughout mouse lifespan[4]. By performing label transfer from their dataset to ours (Methods), we aligned our clusters 842 and 843 to Hammond's two ageing-enriched microglia clusters, OA3 and OA2, respectively (bottom bar of Extended Data Fig. 10d). Similar cluster-specific genes are expressed in our two ageing-enriched clusters, including increased expression of *Ifit2*, *Ifit3*, *Oasl2* and other interferon-response genes in 842, and increased expression of inflammatory markers such as *Cst7* and *Lpl* in 843 (Extended Data Fig. 10c). GO analysis of unique marker genes in these two clusters revealed enrichment of interferon signalling terms in 842, and of other immune cell proliferation and activation terms such as tumour necrosis factor production and C1q complex in 843 (Extended Data Fig. 10e,f).

Whereas there were no significant changes in BAM abundance with age across brain regions, we observed significant increases in proportions of microglia in subcortical regions including midbrain and hindbrain, but not in the isocortex (Extended Data Fig. 8c). Reports of changes in numbers of microglia in rodents varied by region and study[44–47], and our data support the idea that changes in microglia abundance with age vary by brain regions.

Myelination-related changes in oligodendrocytes

The OPC-Oligo cell class contains oligodendrocyte precursor cells (OPCs) and transitioning and mature oligodendrocytes (MOLs). We resolved the oligodendrocyte population into the following supertypes: committed oligodendrocyte precursors (COPs), newly formed oligodendrocytes (NFOLs), myelin-forming oligodendrocytes (MFOLs) and MOLs, following Marques et al.[48] and the ABC-WMB atlas. MOLs are the myelinating cells that make up most of the white matter in the brain by creating and maintaining the myelin sheaths that encase and protect axons as they traverse the brain. Brain-wide decrease in white matter volume with normal ageing has been well-characterized[49,50] and correlates with cognitive decline[51,52].

Across these supertypes, we observed the greatest number of age-DE genes in MOLs (Fig. 2a,d). Age-DE gene signatures of OPCs and MOLs differ notably, whereas OPCs and COPs show more overlapping age-DE genes consistent with their developmental trajectory (Fig. 2l). There is a strong increase in expression of *Abca8a*, *Cdh8* and *Dpyd* in MOLs, confirmed in situ (Fig. 2l,m). Increased expression of *Abca8a* (ref. 53) and *Dpyd*[54] with ageing points to an alteration in myelin maintenance capacity in MOLs. We also observed and spatially confirmed the increased expression of *Maf* and *Nr6a1* in OPCs (Fig. 2l and Extended Data Fig. 9g). *Maf* encodes a transcription factor that heterodimerizes with transcription factor *Nrf2*, and altered brain expression of *Nrf2* and *Maf* has been associated with cognitive impairment and OPC senescence[55,56].

GO analysis showed an enrichment in transporter activity in downregulated OPCs and an enrichment of GO terms related to lipid biosynthesis and transport in both down- and upregulated age-DE genes in MOLs (Extended Data Fig. 9h,i). As myelin is primarily made of lipids, alterations in lipids suggest that myelin sheath integrity may be compromised with ageing, a pattern that was observed in the transcriptomes of human Alzheimer's disease brain cells[57].

Hindbrain enrichment of ageing oligodendrocytes

Of the four classes of non-neuronal cells, the OPC-Oligo class has the greatest number of age-biased clusters (Fig. 2b), including a bias towards adult cells in transitioning COP, NFOL and MFOL types, and a bias towards aged cells in two MOL clusters (Fig. 3a,b). We confirmed the loss of COP, NFOL and MFOL types with age in situ (Fig. 3c,d and

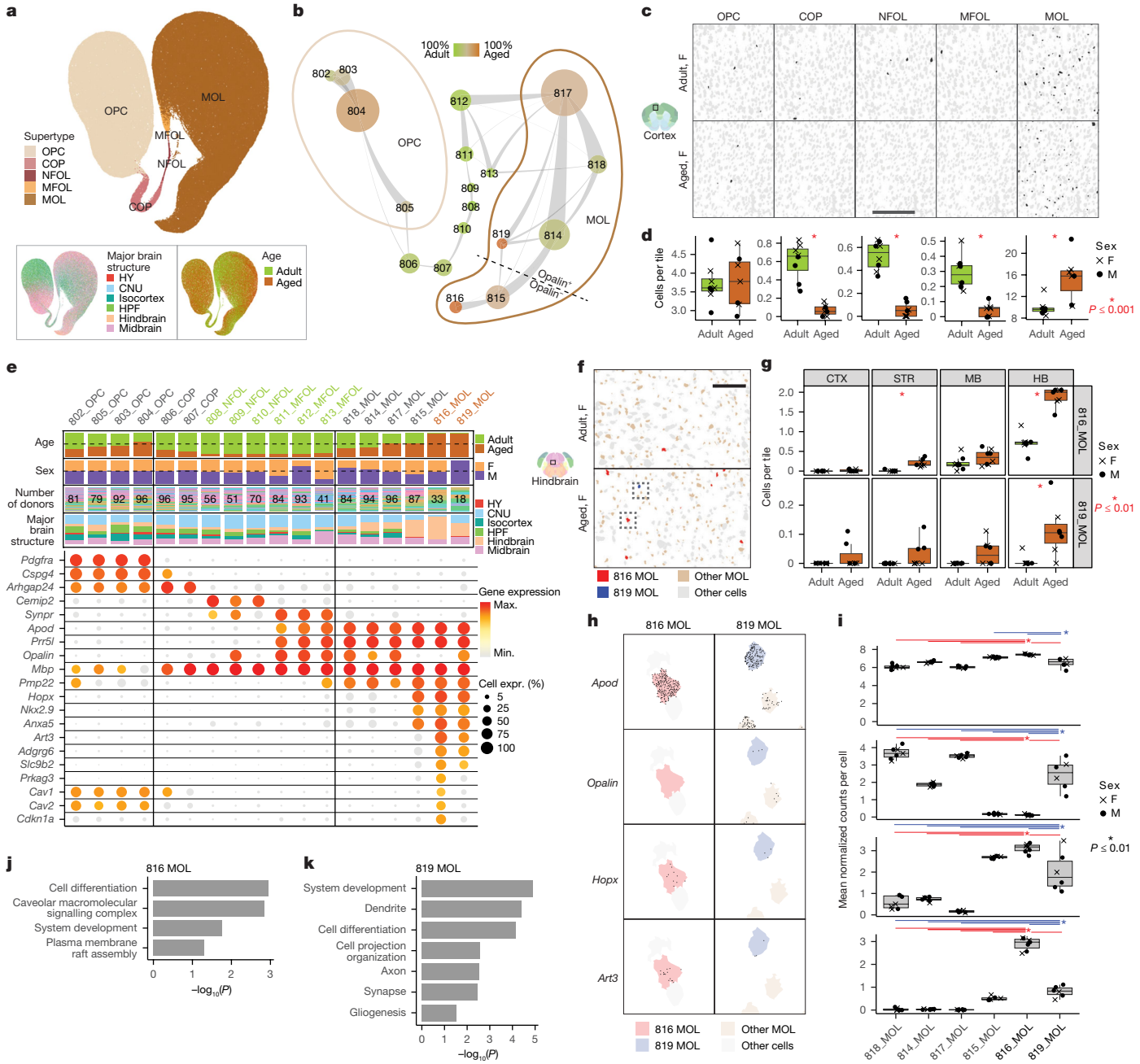

Fig. 3 | Ageing-enriched MOL clusters are observed in hindbrain. a, UMAP of all OPC and oligodendrocyte transcriptomes coloured by supertype, age and major brain structure. **b**, Constellation plot representing OPC and oligodendrocyte clusters using UMAP coordinates shown in **a**. **c**, Spatial locations of OPC-Oligo supertypes from representative samples in the isocortex from RSTE1. **d**, Quantification of OPC-Oligo supertype cell density in the isocortex. Density quantifications for three other regions are shown in Extended Data Fig. 8d. **e**, Bar graphs of each OPC-Oligo cluster by major brain structure, sex, donor and age (top) and dot plots of marker genes for each cluster (bottom). **f**, In situ spatial localization of ageing-enriched MOL clusters 816 and 819 in representative samples of aged and adult hindbrain from RSTE1. **g**, Quantification of density of MOL clusters 816 and 819 across four brain regions from RSTE1. CTX, isocortex; STR, striatum. Significance between changes in density from **d** and **g** are tested using a two-sided Mann–Whitney *U*-test. **h**, Zoom-in view of cells highlighted in **f** showing precise spatial locations of mRNA molecules of *Apod*, *Opalin*, *Hopx* and *Art3*. **i**, Quantification of expression of genes shown in **h** across all MOL clusters. Significance between clusters was tested using an analysis of variance and Tukey's honestly significant difference test. **j**,**k**, Select GO terms enriched in age-DE genes of MOL clusters 816 (**j**) and 819 (**k**). Results in **d**, **g** and **i** represent $n = 3$–4 replicates from RSTE1 per sex, age and region examined over one experiment. For **g** and **i**, only samples with more than ten cells of that cluster were included in the analysis, resulting in certain cell types per sex and/or age that have fewer than four replicates shown. For all boxplots, the minimum, centre and maximum bound of the box represent the 25th, 50th and 75th percentile of the data shown, respectively. The upper and lower whiskers represent the largest and smallest value within 1.5 times above or below the interquartile range, respectively. Scale bars, 200 µm (**c**), 100 µm (**f**).

Extended Data Fig. 8d), suggesting diminished production of new MOLs with age. We observed expected expression of OPC marker genes such as *Cspg4* and *Pdgfra* in all OPC clusters, *Arhgap24* in COP, *Cemip2* in NFOL, *Synpr* in MFOL and *Apod* and *Prr5l* across MFOL and MOL clusters (Fig. 3e). As expected, *Mbp* expression is higher in maturing and mature cells than in OPCs.

The two ageing-enriched MOL clusters, 816 and 819, are mostly derived from hindbrain regions, as is their closest, unbiased MOL

cluster, 815, which all express unique markers that are absent in other MOL clusters, including *Hopx*, *Nkx2-9* and *Anxa5* (Fig. 3b,e). Clusters 815 and 816 do not express *Opalin*, a gene commonly considered as a MFOL- and MOL-specific marker. The ageing-enriched clusters 816 and 819 have specific marker genes unique to them, including *Art3*, *Adgrg6*, *Prkag3* and *Slc9b2*. Cluster 816 also shows unique expression of the cell senescence marker *Cdkn1a*. Whereas senescent astrocytes and microglia have been observed in the ageing brain, whether oligodendrocytes undergo cellular senescence with ageing remains unclear to date[8].

Across the four regions profiled (isocortex, striatum, midbrain, hindbrain), we identified an enrichment of cells mapping most similarly to ageing clusters 816 and 819 in the aged hindbrain samples, consistent with hindbrain enrichment observed from scRNA-seq data (Fig. 3f,g). There are more 816 cells than 819 cells in the spatial data, similar to those in the scRNA-seq data. It is worth noting that whereas 819 appears to be a male-biased cluster in the scRNA-seq data, the in situ cells most closely mapping to it are detected in both male and female animals. Marker gene levels in the spatial data resemble those in scRNA-seq, including low *Opalin* expression in 815 and 816, expression of *Hopx* in hindbrain-enriched clusters, as well as *Art3* and *Cdkna1* expression in 816 (Fig. 3h,i).

GO enrichment analysis on marker genes specific to clusters 816 and 819 separately revealed broad terms of system development and cell differentiation enriched in both sets of marker genes (Fig. 3j,k). For 816, there is a unique enrichment of genes involved in the caveolar macromolecular signalling complex, including *Cav1* and *Cav2* (Fig. 3e), and an enrichment of genes related to plasma membrane raft assembly. For 819, there is an enrichment of neuronal structure (dendrite, axon and synapse) genes, as well as an enrichment of genes related to gliogenesis.

Altogether, these results confirm the previously observed decrease in MOL development with age and identify two previously undescribed ageing-enriched MOL clusters that are predominantly found in the hindbrain, one of which is *Opalin*-negative and shows markers of cellular senescence.

Changes in ependymal cells and tanycytes with age

Two cell types showing the greatest transcriptomic changes with age are ependymal cells and tanycytes (Fig. 2d), which are small populations of specialized glia that line specific ventricles in specific regions of the brain. They are related to astrocytes and belong to the Astro-Epen class in the ABC-WMB atlas (Fig. 4a). Ependymal cells are ciliated glia that line all the ventricles within the brain and the central canal of spinal cord and assist in the circulation of cerebrospinal fluid throughout the ventricular system[58]. Tanycytes line the ventral and ventrolateral sides of V3 in the hypothalamus and possess a single long protrusion that projects into the nearby parenchyma[59]. Tanycytes have been shown to contribute to various functions in the hypothalamus, including forming the blood–brain barrier at circumventricular organs (CVOs, regions of the brain characterized by the presence of highly permeable vessels with fenestrated endothelium)[59,60], regulating nutrient sensing and hormone signalling[59], as well as showing adult neurogenic ability that may act as an adaptive mechanism in response to external factors such as physical activity and diet[61,62]. We found similar sets of age-DE genes and GO terms enriched with age in these two subclasses, but not the other Astro-Epen subclasses (Fig. 4b). We spatially identified tanycytes and ependymal cells lining V3 (Fig. 4c). There is a dorsal-to-ventral transition between the two cell subclasses based on marker genes *Gpr50* for tanycytes and *Tm4sf1* for ependymal cells (Extended Data Fig. 11a), allowing us to visually confirm and interrogate gene expression changes with age.

In ependymal cells and to a lesser extent in tanycytes, there is increased expression with ageing of many interferon-response genes, such as *Ifi27*, *Ifit1*, *Ifit3* and *Oasl2* (Fig. 4b). We confirmed increased expression of *Oasl2* and *Ifit1* in ependymal cells in situ (Fig. 4d). There is also increased expression in genes involved in the MHC-I response, including *B2m*, *Bst2*, *H2-K1* and *H2-D1*, across both cell subclasses but more strongly in ependymal cells (Fig. 4b). These age-DE genes contribute to an enrichment of GO terms related to immune response, MHC-I protein complex, as well as interferon-mediated signalling that is unique to ependymal cells (Extended Data Fig. 11b).

Among genes with the strongest decrease in expression with ageing in both cell subclasses are the cell cycle gene *Ccnd2* and cadherin-associated protein gene *Ctnna2*, which were also confirmed in situ (Fig. 4b,d). *Ccnd2* has been shown to play an important role in adult neurogenesis[63]. *Ctnna2* is involved in the regulation of neuron migration and neuron projection development[64]. GO analysis revealed enrichment of terms with decreased gene expression related to neurogenesis, neuron differentiation, dynein complex and microtubule-based movement in tanycytes (Extended Data Fig. 11b), suggesting a decrease in neurogenic potential in tanycytes with ageing.

To investigate changes with age at the finer cell-type level, we further clustered both tanycytes and ependymal cells. Because our original tanycyte scRNA-seq dataset was unbalanced towards a larger number of aged cells, we added adult cells from the ABC-WMB atlas dataset[3] that were originally excluded because they came from mice housed under reversed light/dark cycle (Methods). We confirmed that there is no significant effect of light/dark cycle on tanycyte clustering in uniform manifold approximation and projection (UMAP) space (Extended Data Fig. 11c).

After clustering, we defined six tanycyte and three ependymal clusters (Fig. 4e). The six tanycyte clusters showed unique sets of marker genes (Extended Data Fig. 11d) mostly aligning with different known subtypes of tanycytes[59,65]. To estimate the spatial location of each tanycyte cluster, we examined cluster labels from the adult tanycyte cells and their annotated locations in the ABC-WMB spatial atlas[3] (Extended Data Fig. 11e). We found representation of nearly all adult whole-brain tanycyte clusters: cluster 792 represents tanycytes from rostral V3, clusters 794 and 795 represent the most dorsal α1 subtype (aligned with the dorsomedial (DMH) and ventromedial (VMH) nuclei of the hypothalamus), 793 represents the α2 subtype (aligned with dorsal and mostly posterior ARH), 796 represents the β1 subtype (aligned with the ARH) and 797 probably represents a mixture of subtypes β1 and β2 (aligned with the median eminence, ME) (Fig. 4f and Extended Data Fig. 11e). Using these annotations, our correlation mapping of the RSTE3 data revealed concordance of some of these clusters in situ in both aged and adult tissue, supported by consistent tanycyte marker gene expression (Extended Data Fig. 11d,f). Specifically, we consistently detected clusters 795, 796 and 797 in RSTE3 (Fig. 4g), but not clusters 792, 793 and 794 due to the probable rarity of these types in the particular RSTE3 sections. Among the major tanycyte clusters detected in RSTE3, we found variation in age-DE gene expression along the dorsal–ventral axis. The most ventral cluster 797, which is made up of mostly β2 tanycytes, shows a greater increase in expression of *H2-K1*, whereas the more dorsal 795 (α1) and 796 (β1) clusters show a stronger increase in expression of *Ifi27* (Fig. 4h,i).

Among the tanycyte clusters, one cluster, 794, probably representing a subset of α1 tanycytes, appears to be depleted in aged tissue (Fig. 2b and Extended Data Fig. 11d). Cluster 794 expresses a glutamate transporter gene *Slc17a8*, regarded as a marker for α1 tanycytes[65]. This is the only tanycyte subtype that may have full neural stem cell or neurospherogenic potential[66,67], so loss of *Slc17a8* with age may be indicative of loss of neurogenic potential. Furthermore, GO terms enriched in the genes unique to this cluster are related to neuron structure, synapse, projection, and morphogenesis (Extended Data Fig. 11g). However, we did not find evidence of a loss of this cluster with age in situ. This could be due to inconsistent sampling of tanycyte clusters across the anterior to posterior axis of the V3 area.

The three ependymal cell clusters show unique gene markers and were isolated from different regions of the brain, with cluster 800

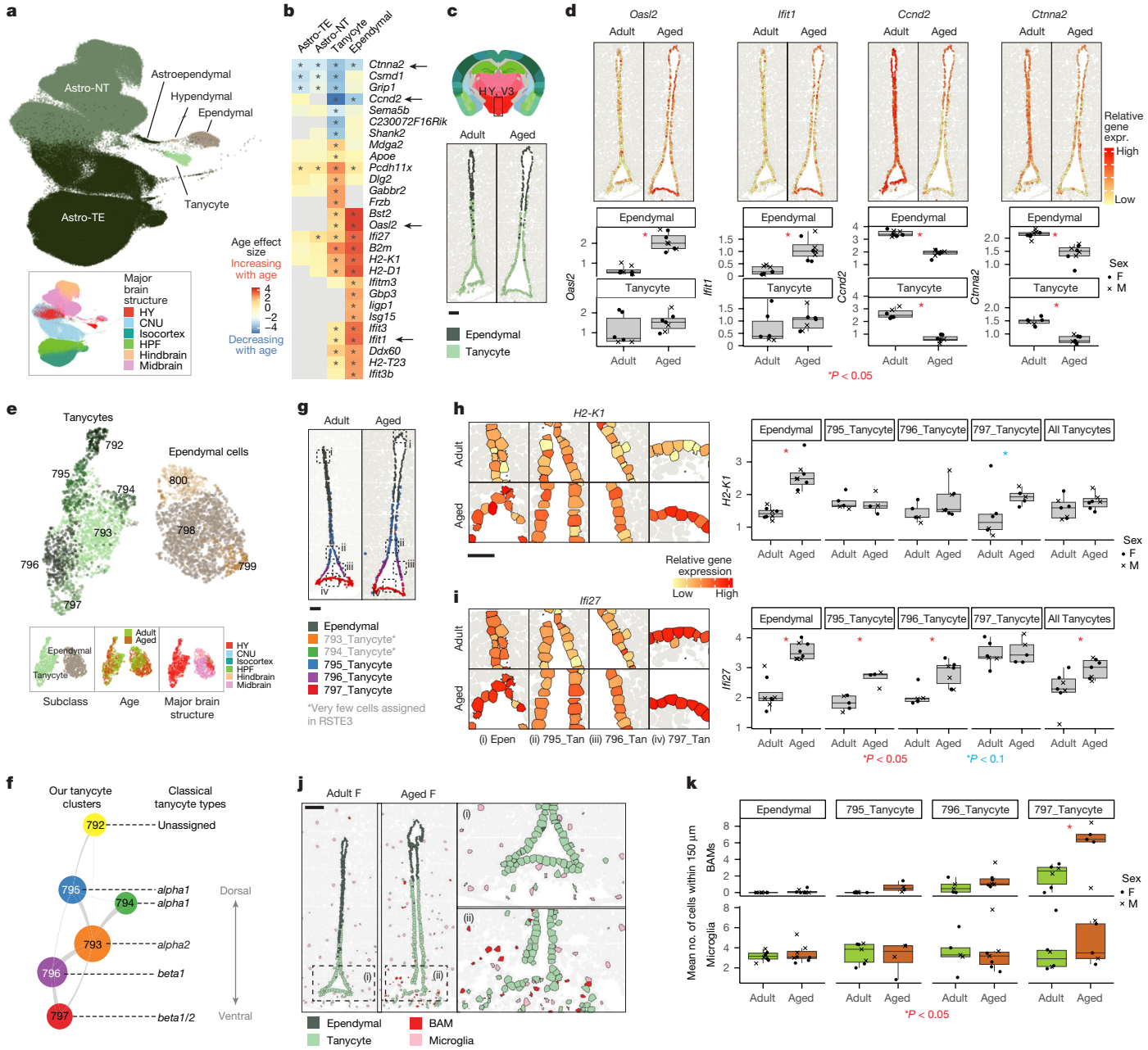

Fig. 4 | Age-associated changes in tanycytes and ependymal cells lining the V3. a, UMAP of all Astro-Epen cell subclasses coloured by subclass and major brain structure. **b**, Heatmap of age effect sizes of top age-DE genes in tanycytes and ependymal cells. The asterisk denotes statistical significance (see subclass level criteria in the Methods). **c**, Tanycyte and ependymal cell body locations in select samples from RSTE3. Brain section with anatomical parcellation is adapted from Allen Mouse Brain CCFv3. **d**, Spatial localization in representative samples from RSTE3 and corresponding gene expression quantification of *Oasl2*, *Ifit1*, *Ccnd2* and *Ctnna2* across ependymal cells and tanycytes in V3. Only samples with more than 20 cells of each subclass are included in the quantification. **e**, UMAP of tanycyte and ependymal cell transcriptomes with extra adult cells from ABC-WMB atlas included, coloured by cluster, subclass, age and brain structure. **f**, Constellation plot of tanycyte clusters in **e**, correlated with classical tanycyte subtypes. **g**, Spatial localization of tanycyte subtypes in V3 in example samples from RSTE3. **h**–**i**, Zoomed-in images (left) of boxed areas (**g**) and quantification (right) of gene expression of *H2-K1* (**h**) and *Ifi27* (**i**) in each subtype from RSTE3. **j**, Spatial localization of immune cells around V3 in example samples from RSTE3. **k**, Mean cell number of BAMs and microglia localized within 150 µm of different V3 cell types. Significance between ages for spatial gene expression was tested using a two-sided Mann–Whitney *U*-test. Results in **d**, **h**, **i** and **k** represent $n = 4$ biological replicates from RSTE3 per sex and/or age from hypothalamus region. Only samples with more than ten cells of that cluster were included in the analysis, resulting in certain cell types per sex and/or age that have fewer than four replicates shown. For all boxplots, the minimum, centre and maximum bound of the box represent the 25th, 50th and 75th percentile of the data shown, respectively. The upper and lower whiskers represent the largest and smallest value within 1.5 times above or below the interquartile range, respectively. Scale bars, 100 µm (**c**,**g**), 50 µm (**h**), 150 µm (**j**).

found in both midbrain and hindbrain, 798 found in mostly midbrain and hypothalamus, and 799 mostly found in midbrain (Extended Data Fig. 11h). Cluster 799 consists almost entirely of aged cells, and thus is assigned ageing-enriched (Fig. 2b and Extended Data Fig. 11h). Unique marker genes for this cluster include interferon-response genes *Iigp1*, *Irf7*, *Ifi44* and *H2-Q4*, all genes that are involved in innate immune response, immune response to virus, cytokine signalling, and other similar GO terms (Extended Data Fig. 11h,i), suggesting an upregulation of immune response with ageing in a distinct group of ependymal cells mostly located in the midbrain.

Given the upregulation of immune response genes in ependymal cells and tanycytes at V3, we next assessed if there is an increase in recruitment of immune cells to this area with ageing. We used spatial dataset RSTE3 and calculated the total number of microglia and BAMs within a 150 µm distance of each cell lining V3, grouping them into broad categories from dorsal to ventral positioning: ependymal cells, tanycyte clusters 795, 796 and 797. Although we did not find significant change in numbers of microglia localized around different parts of V3, there is a significant increase in localization of BAMs near cluster 797, the most ventral cells (β2 tanycytes) located in the median eminence (Fig. 4j,k). Coupled with previous observations of increased microglia and BAM activation in CVOs compared to other brain regions, even in normal adult tissue[68], this suggests that CVOs such as the median eminence may be areas that drive increased inflammation in the brain with ageing.

Hypothalamic neurons in energy homeostasis and ageing

Next, we examined changes in neurons with age. As mentioned above, the greatest numbers of age-DE genes and Augur predictive scores were seen in hypothalamic neurons, as well as a handful of other neuron subclasses (Figs. 1f,g and 5a). There are five classes of hypothalamic neurons in our ageing scRNA-seq dataset, that is, CNU-HYa Glut, CNU-HYa GABA, HY GABA, HY Glut and HY MM Glut (MM standing for medial mammillary nucleus), which are confirmed by *Slc17a6* and *Slc32a1* expression (Fig. 5b and Extended Data Fig. 12a). Under these classes, there are 29 subclasses that show unique marker gene expression (Extended Data Fig. 4 and Supplementary Table 2), altogether capturing the vast cell-type complexity reported in the adult mouse hypothalamus[3]. The subclasses with the greatest numbers of age-DE genes are those in hypothalamic regions proximal to V3, including ARH, DMH and PVH (Fig. 5a,c). Many of these subclasses show specific expression of transcription factors *Tbx3* and *Otp* (Extended Data Fig. 12b).

We further investigated these neurons at the cluster level, specifically those in the six subclasses each with more than 50 age-DE genes (Fig. 5c,d and Extended Data Fig. 12b,c). Neurons in the ARH and DMH are known for, among many functions, their critical role in regulating energy homeostasis and satiety response. Many clusters within these subclasses have highly specific expression of neuropeptides, neuropeptide receptors and hormone genes that are involved in food intake, energy metabolism, satiety and endocrine signalling pathways. For example, cluster 325_DMH-LHA Gsx1 Gaba has high expression of *Lepr* (leptin receptor) and *Glp1r* (glucagon-like peptide 1 receptor), cluster 331_TU-ARH Otp Six6 Gaba has high expression of *Agrp* (agouti-related peptide) and *Npy* (neuropeptide Y), and cluster 374_ARH-PVp Tbx3 Glut has high expression of *Pomc* (proopiomelanocortin) (Fig. 5d and Extended Data Fig. 12b). The well-characterized AgRP-POMC signalling circuit is localized to the ARH. *Agrp/Npy* and *Pomc* neurons stimulate or inhibit food intake, respectively[69,70] and are among the neuronal types that show the greatest numbers of gene expression changes under diet perturbation, including fasting and high-fat diets[71].

We found that among the clusters with the greatest numbers of age-DE genes are the *Lepr*$^+$/*Glp1r*$^+$ cluster 325_DMH-LHA Gsx1 Gaba, the *Agrp*$^+$/*Npy*$^+$ cluster 331_TU-ARH Otp Six6 Gaba, cluster 350_ARH-PVp Tbx3 Gaba, which shows high expression of *Npy5r*, a receptor of neuropeptide Y, and cluster 387_PVH-SO-PVa Otp Glut, which shows specific expression of *Crh*, a gene that encodes corticotropin-releasing hormone (Fig. 5d and Extended Data Fig. 12b). The stress hormone Crh is a major player in the hypothalamic–pituitary–adrenal axis that can become dysregulated with age[72].

Among the GO terms enriched with age-DE genes from the *Agrp*$^+$/*Npy*$^+$ neuron cluster, 331_TU-ARH Otp Six6 Gaba, we saw enrichment of genes involved in various neuromodulatory pathways, including serotonin receptor (*Htr1b*), cannabinoid receptor 1 (*Cnr1*) and histamine H3 receptor (*Hrh3*) (Fig. 5e). We also observed upregulation of circadian rhythm genes (for example, *Bhlhe40*, *Bhlhe41*, *Nr1d2*, *Per3*) and downregulation of genes involved in neuronal structure and synaptic signalling (for example, *Grm8*, *Grik1*, *Gabra5*) with ageing. Whereas cell clusters of this subclass are found in both ARH and the tuberal nucleus (TU), cluster 331 is specifically localized to ARH (Fig. 5f). The increased expression of circadian regulator gene *Bhlhe41* and decreased expression of cell cycle gene *Ccnd2* and metabotropic glutamate receptor *Grm8* with ageing was confirmed in situ (Fig. 5g and Extended Data Fig. 12d).

In the *Lepr*$^+$/*Glp1r*$^+$ cluster, 325_DMH-LHA Gsx1 Gaba, we found increased expression of MHC-I genes (for example, *B2m*, *H2-K1*, *H2-D1*) in aged brains, as well as an increase in expression of genes related to steroid and cholesterol metabolism (for example, *Abca1*, *Idi1*, *Ldlr*, *Msmo1*, *Srebf2*) and neuropeptide hormone activity (for example, *Gal*, *Oxt*, *Vgf*) (Fig. 5h). Significant differential expression of these genes is limited to cluster 325 and not other DMH-LHA clusters, demonstrating the highly specialized nature of these age-associated changes to this small cluster of cells. Among the three DMH-LHA Gsx1 Gaba clusters, 325 is localized to the DMH and shows in situ confirmed increased expression of *H2-K1* and *B2m*, genes associated with MHC-I response (Fig. 5i,j). Whereas expression of MHC genes is most commonly associated with non-neuronal cells, particularly immune cells, there are some reports of MHC-I gene expression in neurons, mostly associated with viral infections and neurodegenerative disease[73]. To our knowledge it has not yet been reported in the context of normal ageing in neurons.

Curious whether other neuron clusters in the hypothalamus also demonstrate an increase in MHC activity, we examined GO terms from all clusters and found a strong increase in MHC-I gene expression in cluster 389_PVH-SO-PVa Otp Glut_4 (Extended Data Fig. 12e). Clusters 389 and 390 in PVH-SO-PVa Otp Glut 4 supertype are highly localized to the retrochiasmatic supraoptic nucleus (rSO) (Extended Data Fig. 12f), have strong expression of neuropeptide genes *Avp* (arginine vasopressin) and *Oxt* (oxytocin), respectively (Fig. 5d), and both show increased expression of *H2-K1* with ageing in situ (Extended Data Fig. 12g). Coincidentally, all the clusters that show an increase in MHC-I activity also show distinctive expression of *Glp1r* (Fig. 5d), an intriguing result considering recent studies reporting anti-inflammatory effects of Glp1 on various tissues including the brain[74].

Hindbrain neuron types sensitive to ageing

In addition to the above hypothalamic neuron types, the greatest numbers of age-DE genes and Augur predictive scores are also seen in a handful of other neuron subclasses, including L4 RSP-ACA Glut and PRP-NI-PRNc-GRN Otp Glut (Figs. 1f and 5a, Extended Data Fig. 13a).

The hindbrain neuron subclass PRP-NI-PRNc-GRN Otp Glut shows strong and specific expression of transcription factors *Otp* and *Evx2* (Extended Data Fig. 13b). Neurons in this subclass are located in specific nuclei in both pons and medulla, but because we did not profile medulla in this study, we only observed the supertypes localized to the nucleus incertus (NI) and caudal pontine reticular nucleus (PRNc) in pons, which include supertypes 2–4 (Extended Data Fig. 13b). Among the GO terms enriched in age-DE genes observed in this subclass, we saw a decrease in synaptic signalling and neuronal structure genes, similar to many other neuron types, as well as decreased expression of genes involved in ephrin receptor signalling (*Epha3*, *Epha5*, *Epha7*) and kainate selective glutamate receptor signalling (*Grik3*, *Grik4*), which are uniquely enriched in only this subclass (Extended Data Fig. 13c,d). Although we did not see a specific cluster within this subclass that drives these changes (probably due to small cell numbers), the largest age effect sizes were observed in clusters 692 and 694, which also express genes related to food intake and energy homeostasis including *Lepr* and *Npy* (Extended Data Fig. 13b,d).

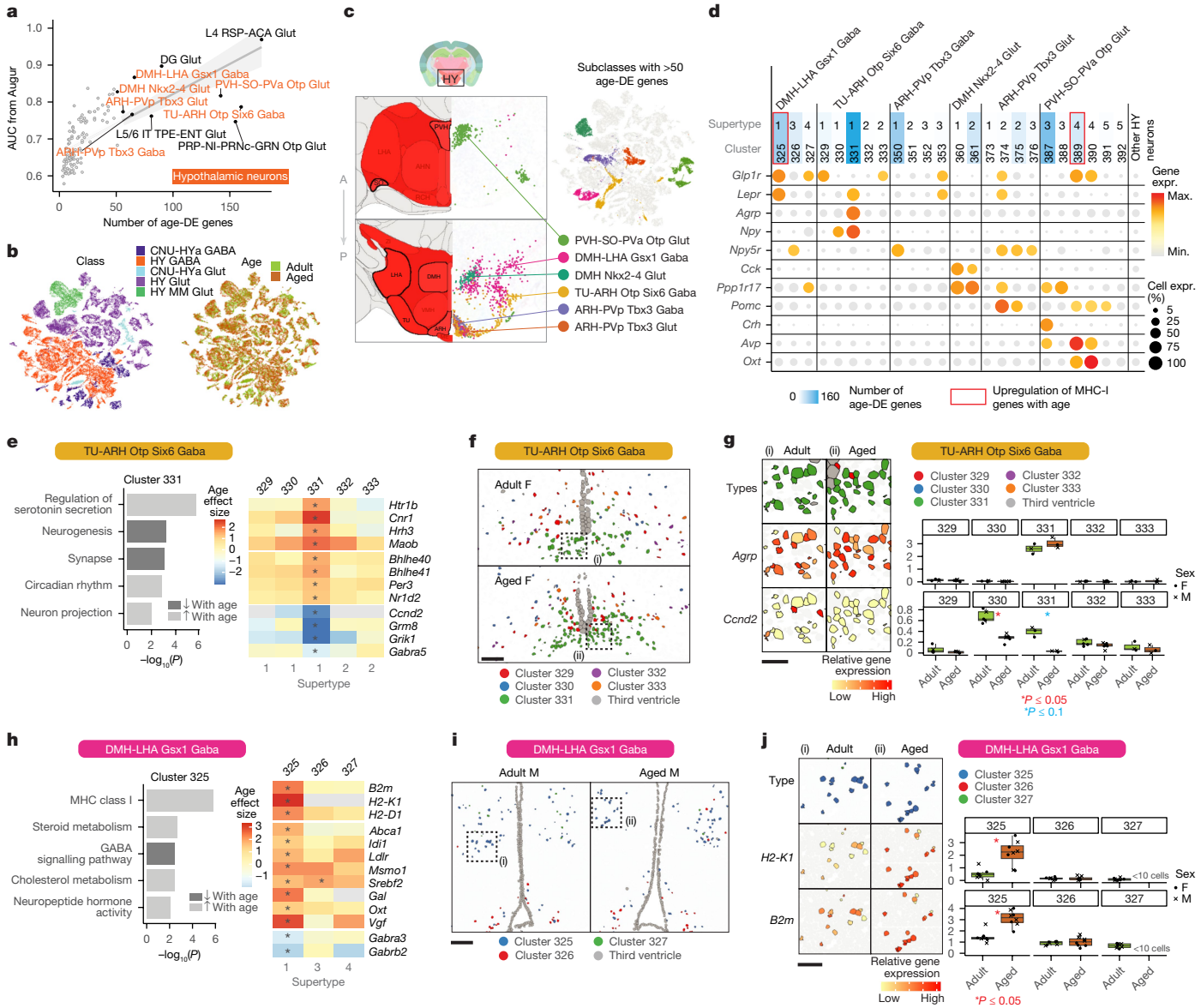

Fig. 5 | Hypothalamic neuron types showing the greatest age-associated changes are involved in energy homeostasis. a, Relationship between the number of age-DE genes and Augur AUC score for each neuronal subclass. Linear model with 95% confidence interval of fit is shown by the light grey shading. **b**, UMAP of all hypothalamic (HY) neurons coloured by class and age. **c**, Same UMAP from **b** with only the six subclasses having more than 50 age-DE genes highlighted, and the spatial locations of these subclasses taken from the ABC-WMB atlas in comparison with the HY subregion delineation in Allen Mouse Brain CCFv3. **d**, Dot plot of expression of the canonical genes involved in feeding behaviour and energy homeostasis for clusters from hypothalamic neuron subclasses with the greatest numbers of age-DE genes. **e**, Select GO terms enriched in age-DE genes from cluster 331_TU-ARH Otp Six6 Gaba (left) and heatmap of age effect sizes for select genes belonging to major enriched GO terms for all TU-ARH Otp Six6 Gaba clusters (right). Asterisks denote significant changes. **f**, Spatial localization of all TU-ARH Otp Six6 Gaba clusters in representative samples from RSTE4. **g**, Zoomed-in view of boxed areas in **f** coloured by cluster or expression of *Agrp* and *Ccnd2* (left), and quantification of expression of these two genes from RSTE4. **h**, Select GO terms enriched in age-DE genes from cluster 325_DMH-LHA Gsx1 Gaba (left) and heatmap of age effect sizes for select genes belonging to major enriched GO terms for all DMH-LHA Gsx1 Gaba clusters (right). **i**, Spatial localization of all DMH-LHA Gsx1 Gaba clusters in representative samples from RSTE3. **j**, Zoomed-in view of boxed areas in **i** coloured by cluster or expression of *H2-K1* and *B2m* (left), and quantification of expression of these two genes from RSTE3. Significance between ages for spatial gene expression was tested using a two-sided Mann–Whitney *U*-test. Results represent $n = 4$ biological replicates per sex and/or age from RSTE4 (**g**) and RSTE3 (**j**), respectively. Only samples with more than ten cells of that cluster were included in the analysis, resulting in certain clusters per sex/age that have fewer than four replicates shown. For all boxplots, the minimum, centre and maximum bound of the box represent the 25th, 50th and 75th percentile of the data shown, respectively. The upper and lower whiskers represent the largest and smallest value within 1.5 times above or below the interquartile range, respectively. Scale bars, 100 µm (**f**,**j**), 50 µm (**g**), 200 µm (**i**).

Reduced IEG response in L4 RSP neurons with ageing

One of the neuronal subclasses having the greatest numbers of age-DE genes and Augur predictive scores is L4 RSP-ACA Glut, a distinctive type of cortical area-specific excitatory neurons that reside in RSP and, to a lesser extent, ACA (Fig. 5a and Extended Data Fig. 13a,e). This subclass has been shown as a midline-projecting neuron type involved in the mouse default mode network (DMN) that mediates resting state cortical activity[75]. The GO terms with the greatest enrichment in L4 RSP-ACA Glut have a decrease in genes involved in visual system development, microRNA transcription and collagen network, and there is a decreased expression of *Pde7b* (Extended Data Fig. 13e). Notably, an

unusually large number (17) of immediate early genes (IEGs), a suite of genes activated rapidly in response to a wide variety of stimuli (see Supplementary Table 3 for a complete list), are mostly decreasing with age in L4 RSP-ACA Glut neurons (Extended Data Fig. 13f). Furthermore, among non-IEG age-DE genes in L4 RSP-ACA Glut, there is an enrichment of downregulated genes that are targets of an IEG, *Egr1* (Extended Data Fig. 13g). Although we cannot rule out the potential technical confounds for IEG activation during tissue preparation of scRNA-seq libraries, the fact that L4 RSP-ACA cells have more substantial IEG changes with age than other cell types, and that they were implicated in a highly connected part of the mouse DMN[75], suggest that these changes may reflect biological changes in DMN activity with ageing.

Common signatures of ageing across cell types

Finally, to reveal common biological processes that are changing (driven by either increased or decreased gene expression) across many cell types in all profiled brain regions, we clustered the most common GO terms that are enriched across all neuron subclasses and non-neuronal supertypes and visualized them in a matrix coloured by significance score of each term (Fig. 6a and Supplementary Table 5).

We observed many common biological processes that are enriched across several cell types. For example, there is a decrease in expression of genes related to collagen network and extracellular matrix, mostly driven by different collagen genes (for example, *Col4a2*, *Col1a2* and *Col3a1*) in pericytes, SMCs and VLMC supertype 2 (Extended Data Fig. 14a), consistent with decreased structural integrity and collagenous remodelling observed in brain vasculature with age[76]. There are also certain biological terms that change in opposite directions for different cell types. For example, GO terms related to cholesterol and lipid metabolism show decreased expression with ageing of associated genes in MOLs but increased expression in the hypothalamic neuron subclass DMH-LHA Gsx1 Gaba (Extended Data Fig. 14b). These terms are partially driven by overlapping sets of genes, including *Dhcr24*, *Hmgcs1* and *Idi1*, as well as genes that are uniquely changing in one type or the other. A decrease in lipid biosynthesis with ageing is consistent with a loss of lipid-rich myelin integrity and production in MOLs[77]. Although it is unclear what this may mean in DMH-LHA Gsx1 Gaba neurons, the fact that this subclass shows a strong age response (Fig. 5a), contains clusters with strong *Lepr* and *Glp1r* expression (Fig. 5d), and is one of the only few neuron types showing increased MHC-I activity with ageing (Fig. 5d,h–j) is intriguing.

Across most non-neuronal cell types, terms related to immune response and cell migration are highly enriched in genes with increased expression with ageing, particularly in immune cells including microglia and BAMs (Fig. 6a). Within these immune terms, we identified specific changes in MHC-I or MHC-II antigen-presentation response that overlap in many cell types: both non-neuronal and neuronal. Specifically, there is a significant upregulation of MHC-I response in microglia, tanycytes, ependymal cells, endothelial cells, and DMH-LHA Gsx1 Gaba neurons, whereas there is a strong upregulation of MHC-II in BAMs and ABCs (Fig. 6b). MHC-I and MHC-II upregulation is partially driven by an upregulation in histocompatibility (H2) genes (Fig. 6b). MHC-I responses appear to be driven by different H2 genes in different cell types. All but one of the cell types that have increased MHC-I responses show an increase in *H2-D1* and *H2-K1* expression with ageing, whereas only endothelial cell MHC-I response is driven by *H2-Q4*, *H2-Q6* and *H2-Q7*, and ependymal cells are the only type that shows a significant increase in *H2-T23*. By contrast, MHC-II activities in BAMs and ABCs are largely driven by the same H2 genes (for example, *H2-Aa*, *H2-Ab1*, *H2-DMb1*, *H2-Eb1* and *H2-DMa*).

Across neurons, the most common GO terms enriched in age-DE genes are related to neuron development, function and structure (for example, neurogenesis, neuron development, presynapse, postsynapse, axon guidance, and dendrite). These terms are primarily enriched in genes with decreased expression with ageing. As these terms are very broad and span many different gene sets that cover various functional pathways, we interpreted them as being indicative of general neuronal function. Specifically, we found 16 different neuron subclasses with enrichment of one or more 'neuronal function' terms, with the greatest numbers of neuron types coming from the cortex and hypothalamus (Extended Data Fig. 14c). We also observed a decrease in neuronal function terms in some non-neuronal types, that is, MOLs, VLMC supertype 1, ependymal cells, tanycytes and certain astrocyte supertypes (Extended Data Fig. 14c).

Last, at individual gene level, we found certain neuronal genes that are downregulated across a handful of neuron types, including *Robo1* and *Sema6d*, both of which code for axon guidance proteins (Fig. 6c). However, most genes are uniquely downregulated in individual neuron types (Fig. 6c), further demonstrating that most neurons possess unique ageing signatures.

Discussion

A gradual loss of homeostasis across many aspects of cellular and organismal function occurs with ageing. Many of these themes, or hallmarks, of ageing, including genomic instability, epigenetic alteration, chronic inflammation, cellular senescence, and deregulated nutrient signalling, have been observed in many invertebrate and vertebrate species[1,2]. However, the mechanisms that govern systemic ageing at the organismal level across complex tissue types and organ systems remain unclear. Furthermore, it is poorly understood if certain cell types are more vulnerable than others to specific aspects of ageing.

In this study, we present a large-scale, comprehensive single-cell transcriptomic atlas and comparative analysis of young adult and aged mouse brains. Large cell numbers, high quality of transcriptomes and detailed annotation of cell types using the ABC-WMB atlas enabled us to precisely pinpoint the regions and cell types in the brain vulnerable to ageing. Consequently, we identified a large set (2,449) of genes showing age-associated differential expression in specific cell types throughout the brain (Fig. 1f,h and Supplementary Table 3). Some of these gene expression changes are strong enough to drive the emergence of transcriptionally distinct cell clusters that are either enriched or depleted in the aged brain, including small populations of IMNs, astrocytes, tanycytes, ependymal cells, oligodendrocytes and microglia (Fig. 2b).

We find evidence supporting some of the established hallmarks of brain ageing, while pinpointing specific cell types in the aged mouse brain as main contributors to these hallmarks (summarized in Fig. 6d). These include (1) stem-cell exhaustion as seen through the depletion of IMNs and certain astrocyte populations in regions of adult neurogenesis (Fig. 2c–e), (2) increased immune response and inflammation as shown by the ageing-enriched pro-inflammatory microglia clusters (Extended Data Fig. 10) and increased expression of genes involved in immune response, inflammation and MHC antigen presentation across various non-neuronal and neuronal types (Fig. 6a,b), (3) deteriorated neuronal network structure and activity as indicated by an observed decrease in new myelination due to the depletion of immature oligodendrocyte cell types and altered gene expression in MOLs (Fig. 3), and decreased expression of genes involved in neuronal signalling and structural integrity in a large number of neuron and astrocyte types (Fig. 6a,c), and (4) dysregulated nutrient signalling and energy homeostasis through changes in gene expression related to both neuronal and immune functions observed in tanycytes, ependymal cells and neurons localized around the V3 of the hypothalamus (Figs. 4 and 5).

Dysregulated nutrient sensing and the gradual loss of energy homeostasis is a main area of ageing and longevity research. Moreover, caloric restriction and intermittent fasting have been shown to delay ageing-associated structural and functional decline and increase longevity across several animal species[78]. The cell types with the most

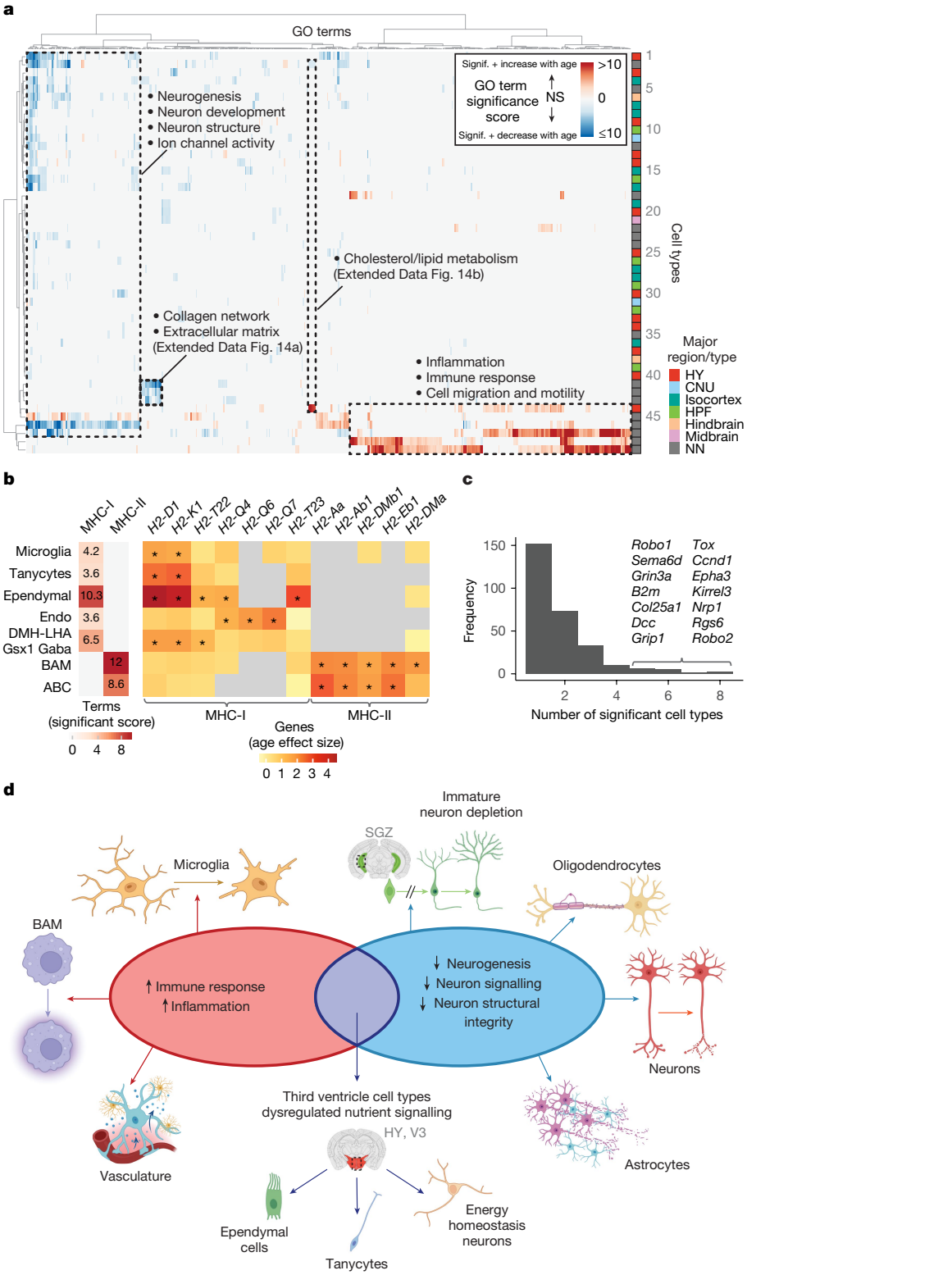

Fig. 6 | Decreased neuronal function and increased immune activity as common signatures of ageing across brain cell types. a, Heatmap of hierarchically clustered GO significance scores for cell types (rows) and common terms (columns). Significance scores were calculated by taking the $-\log_{10}(P)$ for each GO term, with positive or negative scores assigned to increased or decreased gene expression with ageing in each term. Boxed areas show groups of related terms that are significant across one or more cell types. The matrix used for this heatmap is included in Supplementary Table 5 in the same order as shown in the figure. NN, non-neuronal. **b**, Heatmaps of GO significance scores of MHC-I and MHC-II activity (left) and age effect sizes of select H2 genes (right) for select cell types. Asterisks denote significant age-DE genes as defined by adjusted $P < 0.01$ and abs(age effect size) greater than one. **c**, Distribution of the number of cell types for which a gene belonging to a neuronal signalling or structure term is significant. **d**, Summary of major trends in ageing-associated gene expression changes, including increased immune response and decreased neuronal function in different cell types. Schematic in **d** was created using BioRender (https://biorender.com).

prominent age-related gene expression changes around the V3, including tanycytes, *Agrp*$^+$ neurons, *Crh*$^+$ neurons, *Lepr*$^+$ neurons and *Glp1r*$^+$ neurons all play distinctive roles in the brain's ability to integrate nutrient and hormonal signals from the rest of the body. CVOs contain a more permissive blood vascular system than the rest of the brain, allowing nutrients and hormones from blood to interact more freely with neurons and glia locally[79].

Tanycytes are a key integrator of nutrient and sex hormone signalling within the brain[59] and have adult neurogenic and gliogenic potentials, possibly in response to changes in diet[80]. AgRP neurons are part of the melanocortin AgRP/POMC neuron signalling network that control feeding behaviour and satiety response[69,70]. CRH neurons and AgRP neurons are key neurons in the hypothalamic–pituitary–adrenal axis[81], a neuroendocrine signalling network in the brain that controls stress response and can become dysregulated with ageing[72] and contribute to age-associated frailty, loss of psychological resilience and decreased emotion regulation[82]. LepR neurons in DMH respond to circulating leptin, a key hormone synthesized mostly in adipose tissue that regulates satiety response. These neurons also regulate diurnal feeding behaviour in mice[83]. GLP1R neurons bind GLP1, another satiety-controlling peptide that is mimicked by semaglutide-based diabetes drugs that have shown effectiveness at treating obesity through appetite suppression[84]. In our dataset, *Lepr*$^+$/*Glp1r*$^+$ neurons around the V3, as well as the *Avp*$^+$/*Oxt*$^+$ neurons, are among the only neuron types with an increase in MHC antigen-presentation activity with ageing (Fig. 5h–j and Extended Data Fig. 12e–g), pathways that are predominantly associated with immune cells. There is also an increase in MHC activity in other non-immune non-neuronal cells including tanycytes and ependymal cells (Figs. 4 and 6b). Taken together with recent studies that highlight anti-inflammatory properties of GLP1 (ref. 74), our results indicate that there may be a meaningful and therapeutically actionable interaction between inflammation and satiety that contributes to ageing-associated maladaptive phenotypes in the brain.

The identification of a variety of robust and highly significant gene expression changes with ageing across many neuronal and non-neuronal cell types throughout the brain demonstrates the power and necessity of single-cell approaches in revealing the mechanisms that govern complex systemic phenotypes like ageing. Extensive experimental validations will be needed to link these gene expression changes with physiological and functional changes in the animal brain during ageing. The results and insights from this work will serve as a foundational resource for the neuroscience and ageing research communities to facilitate detailed investigation of age-associated phenotypes in the brain and the body and the interaction between ageing and various diseases.

Online content

Any methods, additional references, Nature Portfolio reporting summaries, source data, extended data, supplementary information, acknowledgements, peer review information; details of author contributions and competing interests; and statements of data and code availability are available at https://doi.org/10.1038/s41586-024-08350-8.

1. Mattson, M. P. & Arumugam, T. V. Hallmarks of brain aging: adaptive and pathological modification by metabolic states. *Cell Metab.* **27**, 1176–1199 (2018).
2. López-Otín, C., Blasco, M. A., Partridge, L., Serrano, M. & Kroemer, G. The hallmarks of aging. *Cell* **153**, 1194–1217 (2013).
3. Yao, Z. et al. A high-resolution transcriptomic and spatial atlas of cell types in the whole mouse brain. *Nature* **624**, 317–332 (2023).
4. Hammond, T. R. et al. Single-cell RNA sequencing of microglia throughout the mouse lifespan and in the injured brain reveals complex cell-state changes. *Immunity* **50**, 253–271.e6 (2019).
5. Pan, J., Ma, N., Yu, B., Zhang, W. & Wan, J. Transcriptomic profiling of microglia and astrocytes throughout aging. *J. Neuroinflammation* **17**, 97 (2020).
6. Ash, J. A. et al. Functional connectivity with the retrosplenial cortex predicts cognitive aging in rats. *Proc. Natl Acad. Sci. USA* **113**, 12286–12291 (2016).
7. Marstaller, L., Williams, M., Rich, A., Savage, G. & Burianová, H. Aging and large-scale functional networks: White matter integrity, gray matter volume, and functional connectivity in the resting state. *Neuroscience* **290**, 369–378 (2015).
8. Sikora, E. et al. Cellular senescence in brain aging. *Front. Aging Neurosci.* **13**, 646924 (2021).
9. Ximerakis, M. et al. Single-cell transcriptomic profiling of the aging mouse brain. *Nat. Neurosci.* **22**, 1696–1708 (2019).
10. Almanzar, N. et al. A single-cell transcriptomic atlas characterizes ageing tissues in the mouse. *Nature* **583**, 590–595 (2020).
11. Benayoun, B. A. et al. Remodeling of epigenome and transcriptome landscapes with aging in mice reveals widespread induction of inflammatory responses. *Genome Res.* **29**, 697–709 (2019).
12. Kiss, T. et al. Single-cell RNA sequencing identifies senescent cerebromicrovascular endothelial cells in the aged mouse brain. *Geroscience* **42**, 429–444 (2020).
13. Hajdarovic, K. H. et al. Single-cell analysis of the aging female mouse hypothalamus. *Nat. Aging* **2**, 662–678 (2022).
14. Allen, W. E., Blosser, T. R., Sullivan, Z. A., Dulac, C. & Zhuang, X. Molecular and spatial signatures of mouse brain aging at single-cell resolution. *Cell* **186**, 194–208.e18 (2023).
15. Kaya, T. et al. CD8$^+$ T cells induce interferon-responsive oligodendrocytes and microglia in white matter aging. *Nat. Neurosci.* **25**, 1446–1457 (2022).
16. Buckley, M. T. et al. Cell-type-specific aging clocks to quantify aging and rejuvenation in neurogenic regions of the brain. *Nat. Aging* **3**, 121–137 (2023).
17. Park, H. et al. Single-cell RNA-sequencing identifies disease-associated oligodendrocytes in male APP NL-G-F and 5XFAD mice. *Nat. Commun.* **14**, 802 (2023).
18. Langlieb, J. et al. The molecular cytoarchitecture of the adult mouse brain. *Nature* **624**, 333–342 (2023).
19. Zhang, M. et al. Molecularly defined and spatially resolved cell atlas of the whole mouse brain. *Nature* **624**, 343–354 (2023).
20. Yao, Z. et al. A taxonomy of transcriptomic cell types across the isocortex and hippocampal formation. *Cell* **184**, 3222–3241.e26 (2021).
21. DeTure, M. A. & Dickson, D. W. The neuropathological diagnosis of Alzheimer's disease. *Mol. Neurodegener.* **14**, 32 (2019).
22. Wang, Q. et al. The Allen Mouse Brain Common Coordinate Framework: a 3D reference atlas. *Cell* **181**, 936–953.e20 (2020).
23. Finak, G. et al. MAST: a flexible statistical framework for assessing transcriptional changes and characterizing heterogeneity in single-cell RNA sequencing data. *Genome Biol.* **16**, 278 (2015).
24. Robinson, M. D., McCarthy, D. J. & Smyth, G. K. edgeR: a Bioconductor package for differential expression analysis of digital gene expression data. *Bioinformatics* **26**, 139–140 (2010).
25. Skinnider, M. A. et al. Cell type prioritization in single-cell data. *Nat. Biotechnol.* **39**, 30–34 (2021).
26. Guttman, M. et al. Chromatin signature reveals over a thousand highly conserved large non-coding RNAs in mammals. *Nature* **458**, 223–227 (2009).
27. Schuiki, I. & Daum, G. Phosphatidylserine decarboxylases, key enzymes of lipid metabolism. *IUBMB Life* **61**, 151–162 (2009).
28. Zhao, T. et al. PISD is a mitochondrial disease gene causing skeletal dysplasia, cataracts, and white matter changes. *Life Sci. Alliance* **2**, e201900353 (2019).
29. Yoo, S. & Blackshaw, S. Regulation and function of neurogenesis in the adult mammalian hypothalamus. *Prog. Neurobiol.* **170**, 53–66 (2018).
30. Ruiz-Martínez, J., Azcona, L. J., Bergareche, A., Martí-Massó, J. F. & Paisán-Ruiz, C. Whole-exome sequencing associates novel CSMD1 gene mutations with familial Parkinson disease. *Neurol. Genet.* **3**, e177 (2017).
31. Baum, M. L. et al. CSMD1 regulates brain complement activity and circuit development. *Brain. Behav. Immun.* **119**, 317–332 (2024).
32. Denoth-Lippuner, A. & Jessberger, S. Formation and integration of new neurons in the adult hippocampus. *Nat. Rev. Neurosci.* **22**, 223–236 (2021).
33. Kuhn, H. G., Dickinson-Anson, H. & Gage, F. H. Neurogenesis in the dentate gyrus of the adult rat: age-related decrease of neuronal progenitor proliferation. *J. Neurosci.* **16**, 2027–2033 (1996).
34. Watanabe, C. et al. Aging of the vascular system and neural diseases. *Front. Aging Neurosci.* **12**, 557384 (2020).
35. Bennett, H. C. & Kim, Y. Pericytes across the lifetime in the central nervous system. *Front. Cell. Neurosci.* **15**, 627291 (2021).
36. Takino, J., Miyazaki, S., Nagamine, K. & Hori, T. The role of RASGRP2 in vascular endothelial cells—a mini review. *Int. J. Mol. Sci.* **22**, 11129 (2021).
37. Shi, W. et al. HDAC9 exacerbates endothelial injury in cerebral ischaemia/reperfusion injury. *J. Cell. Mol. Med.* **20**, 1139–1149 (2016).
38. Rossner, R., Kaeberlein, M. & Leiser, S. F. Flavin-containing monooxygenases in aging and disease: emerging roles for ancient enzymes. *J. Biol. Chem.* **292**, 11138–11146 (2017).
39. Stephenson, J., Nutma, E., van der Valk, P. & Amor, S. Inflammation in CNS neurodegenerative diseases. *Immunology* **154**, 204–219 (2018).
40. Hickman, S. E. et al. The microglial sensome revealed by direct RNA sequencing. *Nat. Neurosci.* **16**, 1896–1905 (2013).
41. Yosef, R. et al. Directed elimination of senescent cells by inhibition of BCL-W and BCL-XL. *Nat. Commun.* **7**, 11190 (2016).
42. Ogrodnik, M. et al. Whole-body senescent cell clearance alleviates age-related brain inflammation and cognitive impairment in mice. *Aging Cell* **20**, e13296 (2021).
43. Ritzel, R. M. et al. Old age increases microglial senescence, exacerbates secondary neuroinflammation, and worsens neurological outcomes following acute traumatic brain injury in mice. *Neurobiol. Aging* **77**, 194–206 (2019).
44. Zöller, T., Attaai, A., Potru, P. S., Ruß, T. & Spittau, B. Aged mouse cortical microglia display an activation profile suggesting immunotolerogenic functions. *Int. J. Mol. Sci.* **19**, 706 (2018).
45. Hefendehl, J. K. et al. Homeostatic and injury-induced microglia behavior in the aging brain. *Aging Cell* **13**, 60–69 (2014).
46. Vaughan, D. W. & Peters, A. Neuroglial cells in the cerebral cortex of rats from young adulthood to old age: an electron microscope study. *J. Neurocytol.* **3**, 405–429 (1974).

47. Long, J. M. et al. Stereological analysis of astrocyte and microglia in aging mouse hippocampus. *Neurobiol. Aging* **19**, 497–503 (1998).
48. Marques, S. et al. Oligodendrocyte heterogeneity in the mouse juvenile and adult central nervous system. *Science* **352**, 1326–1329 (2016).
49. Lintl, P. & Braak, H. Loss of intracortical myelinated fibers: a distinctive age-related alteration in the human striate area. *Acta Neuropathol.* **61**, 178–182 (1983).
50. Charlton, R. A., Schiavone, F., Barrick, T. R., Morris, R. G. & Markus, H. S. Diffusion tensor imaging detects age related white matter change over a 2 year follow-up which is associated with working memory decline. *J. Neurol. Neurosurg. Psychiatry* **81**, 13–19 (2010).
51. Chopra, S. et al. More highly myelinated white matter tracts are associated with faster processing speed in healthy adults. *NeuroImage* **171**, 332–340 (2018).
52. Bartzokis, G. et al. Heterogeneous age-related breakdown of white matter structural integrity: Implications for cortical 'disconnection' in aging and Alzheimer's disease. *Neurobiol. Aging* **25**, 843–851 (2004).
53. Kim, W. S. et al. ABCA8 stimulates sphingomyelin production in oligodendrocytes. *Biochem. J.* **452**, 401–410 (2013).
54. Schirmer, L. et al. Neuronal vulnerability and multilineage diversity in multiple sclerosis. *Nature* **573**, 75–82 (2019).
55. Yang, T. & Zhang, F. Targeting transcription factor Nrf2 (nuclear factor erythroid 2-related factor 2) for the intervention of vascular cognitive impairment and dementia. *Arterioscler. Thromb. Vasc. Biol.* **41**, 97–116 (2021).
56. Kujuro, Y., Suzuki, N. & Kondo, T. Esophageal cancer-related gene 4 is a secreted inducer of cell senescence expressed by aged CNS precursor cells. *Proc. Natl Acad. Sci. USA* **107**, 8259–8264 (2010).
57. Mathys, H. et al. Single-cell transcriptomic analysis of Alzheimer's disease. *Nature* **570**, 332–337 (2019).
58. Del Bigio, M. R. Ependymal cells: biology and pathology. *Acta Neuropathol.* **119**, 55–73 (2010).
59. Prevot, V. et al. The versatile tanycyte: a hypothalamic integrator of reproduction and energy metabolism. *Endocr. Rev.* **39**, 333–368 (2018).
60. Prevot, V., Nogueiras, R. & Schwaninger, M. in *Handbook of Clinical Neurology* Vol. 180 (eds Swaab, D. F. et al.) Ch. 16, 253–273 (Elsevier, 2021).
61. Recabal, A., Caprile, T. & García-Robles, M. L. A. Hypothalamic neurogenesis as an adaptive metabolic mechanism. *Front. Neurosci.* **11**, 190 (2017).
62. Sharif, A., Fitzsimons, C. P. & Lucassen, P. J. in *Handbook of Clinical Neurology* Vol. 179 (eds Swaab, D. F. et al.) Ch. 8, 125–140 (Elsevier, 2021).
63. Kowalczyk, A. et al. The critical role of cyclin D2 in adult neurogenesis. *J. Cell Biol.* **167**, 209–213 (2004).
64. Schaffer, A. E. et al. Biallelic loss of human CTNNA2, encoding αN-catenin, leads to ARP2/3 complex overactivity and disordered cortical neuronal migration. *Nat. Genet.* **50**, 1093–1101 (2018).
65. Chen, R., Wu, X., Jiang, L. & Zhang, Y. Single-cell RNA-seq reveals hypothalamic cell diversity. *Cell Rep.* **18**, 3227–3241 (2017).
66. Fong, H. & Kurrasch, D. M. Developmental and functional relationships between hypothalamic tanycytes and embryonic radial glia. *Front. Neurosci.* **16**, 1129414 (2023).
67. Robins, S. C. et al. α-Tanycytes of the adult hypothalamic third ventricle include distinct populations of FGF-responsive neural progenitors. *Nat. Commun.* **4**, 2049 (2013).
68. Takagi, S., Furube, E., Nakano, Y., Morita, M. & Miyata, S. Microglia are continuously activated in the circumventricular organs of mouse brain. *J. Neuroimmunol.* **331**, 74–86 (2019).
69. Cone, R. D. Anatomy and regulation of the central melanocortin system. *Nat. Neurosci.* **8**, 571–578 (2005).
70. De Solis, A. J. et al. Reciprocal activity of AgRP and POMC neurons governs coordinated control of feeding and metabolism. *Nat. Metab.* **6**, 473–493 (2024).
71. Campbell, J. N. et al. A molecular census of arcuate hypothalamus and median eminence cell types. *Nat. Neurosci.* **20**, 484–496 (2017).
72. Aguilera, G. HPA axis responsiveness to stress: Implications for healthy aging. *Exp. Gerontol.* **46**, 90–95 (2011).
73. Cebrián, C., Loike, J. D. & Sulzer, D. Neuronal MHC-I expression and its implications in synaptic function, axonal regeneration and Parkinson's and other brain diseases. *Front. Neuroanat.* **8**, 114 (2014).
74. Mehdi, S. F. et al. Glucagon-like peptide-1: a multi-faceted anti-inflammatory agent. *Front. Immunol.* **14**, 1148209 (2023).
75. Whitesell, J. D. et al. Regional, layer, and cell-type-specific connectivity of the mouse default mode network. *Neuron* **109**, 545–559.e8 (2021).
76. Xu, X. et al. Age-related impairment of vascular structure and functions. *Aging Dis.* **8**, 590–610 (2017).
77. Wang, F. et al. Myelin degeneration and diminished myelin renewal contribute to age-related deficits in memory. *Nat. Neurosci.* **23**, 481–486 (2020).
78. Mattson, M. P., Moehl, K., Ghena, N., Schmaedick, M. & Cheng, A. Intermittent metabolic switching, neuroplasticity and brain health. *Nat. Rev. Neurosci.* **19**, 63–80 (2018).
79. Kiecker, C. The origins of the circumventricular organs. *J. Anat.* **232**, 540–553 (2018).
80. Lee, D. A. et al. Tanycytes of the hypothalamic median eminence form a diet-responsive neurogenic niche. *Nat. Neurosci.* **15**, 700–702 (2012).
81. Chen, W. et al. Nutrient-sensing AgRP neurons relay control of liver autophagy during energy deprivation. *Cell Metab.* **35**, 786–806.e13 (2023).
82. Gaffey, A. E., Bergeman, C. S., Clark, L. A. & Wirth, M. M. Aging and the HPA axis: stress and resilience in older adults. *Neurosci. Biobehav. Rev.* **68**, 928–945 (2016).
83. Faber, C. L. et al. Leptin receptor neurons in the dorsomedial hypothalamus regulate diurnal patterns of feeding, locomotion, and metabolism. *eLife* **10**, e63671 (2021).
84. Wilding John, P. H. et al. Once-weekly semaglutide in adults with overweight or obesity. *N. Engl. J. Med.* **384**, 989–1002 (2021).

Methods

Mouse breeding and husbandry

All procedures were carried out in accordance with Institutional Animal Care and Use Committee protocols at the Allen Institute for Brain Science. Mice were provided food and water ad libitum and were maintained on a regular 14/10 h day/night cycle at no more than five adult animals of the same sex per cage. Ambient temperature of the vivarium was maintained between 21.1 and 22.78 °C (70–73 °F) and humidity was maintained between 40 and 45%. Mice were maintained on the C57BL/6J background. We excluded any mice with dermatitis, anophthalmia, microphthalmia, seizures or abdominal masses.

We used 44 aged mice (20 female, 24 male) and 64 young adult mice (31 female, 33 male) to collect cells for 10xv3 scRNA-seq. All young adult mice were also included in the ABC-WMB atlas[3]. Aged animals were euthanized at P540–553 (roughly 18 months) and young adult animals were euthanized at P53–69 (roughly 2 months). No statistical methods were used to predetermine sample size. All donor animals used in this study are listed in Supplementary Table 1. The Zeitgeber time of the light/dark cycle was similar (within a 3 h window) for all the tissue collections. We did not keep track of the oestrous cycle for female mice.

We isolated a total of 287 libraries from 108 animals: each animal contributed 1–6 libraries. All libraries are listed in Supplementary Table 1. Transgenic driver lines were used for fluorescence-positive cell isolation by FACS to enrich for neurons. Roughly half the libraries ($n = 145$) were sorted for neurons from the pan-neuronal *Snap25-IRES2-Cre* line (JAX strain no. 023525) crossed to the *Ai14*-tdTomato reporter (JAX strain no. 007914)[85,86] (Supplementary Table 1). For unbiased sampling (libraries that were not enriched for neurons), we used *Snap25-IRES2-Cre/wt;Ai14/wt* mice, *Ai14/wt* mice or in very few cases wild-type C57BL/6J mice. Unbiased sampling methods include libraries stained and sorted for Hoechst+, Calcein+/Hoechst+ or unstained libraries that were not sorted at all (no FACS). No FACS cells make up roughly 25% of the final high-quality dataset. The transgenic *Snap25-IRES2-Cre* line was backcrossed to C57BL/6J for at least ten generations before crossing and can be considered congenic. The transgenic *Ai14* line was backcrossed to C57BL/6J for at least five generations before crossing and can be considered incipient congenic. Example images of gating strategies used for FACS are shown in Extended Data Fig. 2.

10x scRNA-seq

Single-cell isolation. We used the CCFv3 (RRID: SCR_002978) ontology[22] (http://atlas.brain-map.org/) to define brain regions for profiling and boundaries for dissection. We covered all selected regions of the brain by sampling at top-ontology level with judicious joining of neighbouring regions. These choices were guided by the fact that microdissections of small regions are difficult. Therefore, joint dissection of neighbouring regions was sometimes necessary to obtain sufficient numbers of cells for profiling.

Single cells were isolated by adapting previously described procedures[20,87]. The brain was dissected, submerged in artificial cerebrospinal fluid (ACSF), embedded in 2% agarose and sliced into 350-µm coronal sections on a compresstome (Precisionary Instruments). Block-face images were captured during slicing. ROI were then microdissected from the slices and dissociated into single cells. Fluorescent images of each slice before and after ROI dissection were taken at the dissection microscope. These images were used to document the precise location of the ROI using annotated coronal plates of CCFv3 as reference.

Dissected tissue pieces were digested with 30 U ml^{-1} papain (Worthington, catalogue no. PAP2) in ACSF for 30 min at 30 °C. Owing to the short incubation period in a dry oven, we set the oven temperature to 35 °C to compensate for the indirect heat exchange, with a target solution temperature of 30 °C. Enzymatic digestion was quenched by exchanging the papain solution three times with quenching buffer (ACSF with 1% fetal bovine serum and 0.2% bovine serum albumin (BSA)). Samples were incubated on ice for 5 min before trituration. The tissue pieces in the quenching buffer were triturated through a fire-polished pipette with a 600 µm diameter opening roughly 20 times. The tissue pieces were allowed to settle and the supernatant, which now contained suspended single cells, was transferred to a new tube. Fresh quenching buffer was added to the settled tissue pieces, and trituration and supernatant transfer were repeated using 300 and 150 µm fire-polished pipettes. The single-cell suspension was passed through a 70 µm filter into a 15 ml conical tube with 500 µl of high BSA buffer (ACSF with 1% fetal bovine serum and 1% BSA) at the bottom to help cushion the cells during centrifugation at 100*g* in a swinging bucket centrifuge for 10 min. The supernatant was discarded, and the cell pellet was resuspended in the quenching buffer. We collected 1,508,284 cells without performing FACS. The concentration of the resuspended cells was quantified, and cells were immediately loaded onto the 10X Genomics Chromium controller.

To enrich for neurons or live cells, cells were collected by FACS (BD FACSAria II or FACSAria Fusion, with FACSDiva v.8 software) using a 130 µm nozzle. Cells were prepared for sorting by passing the suspension through a 70 µm filter and adding Hoechst or 4,6-diamidino-2-phenylindole (DAPI) (to a final concentration of 2 ng ml^{-1}). The sorting strategy was as previously described[3,20], with most cells collected using the tdTomato-positive label. Then, 30,000 cells were sorted within 10 min into a tube containing 500 µl of quenching buffer. We found that sorting more cells into one tube diluted the ACSF in the collection buffer, causing cell death. We also observed decreased cell viability for longer sorts. Each aliquot of sorted 30,000 cells was gently layered on top of 200 µl of high BSA buffer and immediately centrifuged at 230*g* for 10 min in a centrifuge with a swinging bucket rotor (the high BSA buffer at the bottom of the tube slows down the cells as they reach the bottom, minimizing cell death). No pellet could be seen with this small number of cells, so we removed the supernatant and left behind 35 µl of buffer in which we resuspended the cells. Immediate centrifugation and resuspension allowed the cells to be temporarily stored in a high BSA buffer with minimal ACSF dilution. The resuspended cells were stored at 4 °C until all samples were collected, usually within 30 min. Samples from the same ROI were pooled, cell concentration quantified and immediately loaded onto the 10x Genomics Chromium controller.

Complementary DNA amplification and library construction. For 10xv3 processing, we used the Chromium Single Cell 3′ Reagent Kit v.3 (1000075, 10x Genomics). We followed the manufacturer's instructions for cell capture, barcoding, reverse transcription, complementary DNA amplification and library construction. We targeted a sequencing depth of 120,000 reads per cell; the actual average achieved was 77,743 ± 36,025 (mean ± s.d.) reads per cell across 287 libraries (Supplementary Table 1).

Sequencing data preprocessing. All libraries were 10xv3 samples and processed as previously described[3,20]. All libraries were sequenced on Illumina NovaSeq6000 and sequencing reads were aligned to the mouse reference (mm10/gencode.vM23)[88] using the 10x Genomics CellRanger pipeline (v.6.0.0) with the –include introns argument to include intronically mapped reads. This resulted in an scRNA-seq dataset containing 2,777,165 cells.

To remove low-quality cells, we used a stringent QC process. Cells were first filtered by a broad set of quality cut-offs based on gene detection, QC score and doublet score. As we previously described[3], the QC score was calculated by summing the log-transformed expression of a set of genes, whose expression level is decreased significantly in poor-quality cells. Briefly, these are housekeeping genes that are strongly expressed in nearly all cells with a very tight coexpression pattern that is anticorrelated with the nucleus-enriched transcript *Malat1*. We use this QC score to quantify the integrity of cytoplasmic messenger

RNA (mRNA) content. Doublets were identified using a modified version of the DoubletFinder algorithm[89]. For this preliminary round of filtering, we included cells with gene detection greater than 1,000, a QC score greater than 50 and a doublet score less than 0.3. Using these thresholds, 1,999,976 cells remained in the dataset (Extended Data Fig. 3a). Mixing of cell types by library and other metadata categories is visualized in Extended Data Fig. 6f.

Clustering scRNA-seq data. Following the initial round of filtering described above, adult and aged single-cell transcriptomes were co-clustered over two rounds of clustering. The goal for the first round of clustering was to assign a cell class identity to every unlabelled (aged) cell and filter out low-quality (noise) clusters. The goal of the second round of clustering was to assign a subclass identity to every unlabelled (aged) cell and filter out extra low-quality clusters. All adult cells in the dataset already had labels because they are also part of the ABC-WMB cell-type taxonomy[3]. For both rounds, clustering was performed independently with the in-house developed R package scrattch.bigcat (v.0.0.1) as was previously described[3] (available through https://github.com/AllenInstitute/scrattch.bigcat), which is a version of R package scrattch.hicat[20] that can cluster large datasets. Detailed functionality of scrattch.bigcat was discussed in our previous paper[3]. We used the automatic iterative clustering method, iter_clust_big, to perform clustering in a top-down manner into cell types of increasingly finer resolution. This method performs clustering without human intervention, while ensuring that all pairs of clusters, even at the finest level, were separable by differential gene expression criteria (q1.th = 0.4, q.diff.th = 0.7, de.score.th = 300, min.cells = 50, min.genes = 5) for both rounds of clustering. Following each round of clustering using iter_clust_big, we used the function merge_cl to merge clusters based on total number and significance of shared differentially expressed genes. For round 1, the criteria used for merge_cl were identical to those previously described for clustering. For round 2, the criteria used for merge_cl were almost identical with the exception of increasing min.cells = 100.

Finer resolution analysis was performed on microglia, BAMs, tanycytes and ependymal cells and as such, further clustering was performed on only these cell types as follows:

Microglia and BAMs. Microglia and BAMs were separately clustered using the same parameters as used in round 2 of clustering for the larger dataset except with min.cell = 50 and min.genes = 3. Clusters were mapped to the Hammond et al. dataset.

Tanycytes and ependymal cells. Because tanycytes were one of the cell types with the greatest sensitivity to age, they are a relatively rare population of cells compared to other types and in our original dataset there were far fewer adult tanycytes sampled by 10xv3 than aged, we included extra tanycytes from the ABC-WMB atlas dataset to even out the cell numbers. These extra adult tanycytes mostly came from libraries that were prepped under the reversed light/dark cycle conditions compared to all other libraries in this study (Extended Data Fig. 11c). Tanycytes and ependymal cells were then clustered separately using the same conditions as described above for round 2 of clustering for the larger dataset.

Label transfer by means of mapping. Because the adult cells have been previously published and annotated, only the cells from the aged libraries did not have annotations. We mapped all aged cells to the ABC-WMB reference taxonomy as previously described[3]. Briefly, we assigned their cell-type identities by mapping them to the nearest cluster centroid in the reference taxonomy using the corresponding Annoy index using the same method as implemented at present in the R package scrattch.mapping. We also used this approach for assigning cell-type identities for cells segmented from Resolve spatial data to the ABC-WMB cell-type taxonomy or external datasets as reference, using different gene lists based on the contexts. For mapping to the microglia dataset from Hammond et al.[4], we used a list of 72 genes that was assembled on the basis of prominent marker genes from each reference cluster. When a mapping confidence score was needed, we sampled 80% genes from the marker list randomly and performed mapping 100 times. We define the fraction of times a cell is assigned to a given cell type as the mapping probability to that type.

Assigning labels to aged cells and removing low-quality clusters. We observed 2,467 clusters after the first round of clustering. At this point, all cells were assigned a cell category (Glut, GABA, Dopa, Sero, IMN or NN), which matched labels from an older version of the ABC-WMB reference taxonomy. As the adult cells have been previously published and annotated, cell annotations for aged cells were assigned on the basis of cluster membership with annotated adult cells. Specifically, clusters that contained more than 5% of annotated adult cells were assigned that cell category. Median gene detection (GC_{med}) and median QC score (QC_{med}) were calculated for each cluster. Clusters that belonged to non-neuronal and IMN categories with $GC_{med} < 2{,}000$ and $QC_{med} < 100$ were removed from the dataset. Clusters that belonged to neuronal categories with $GC_{med} < 3{,}000$ and $QC_{med} < 250$ were removed from the dataset. Clusters with more than 80% contribution from a single library were also filtered out to minimize donor bias in the final dataset. Clusters with less than 5% adult cells were retained in the dataset and carried over into the next round of clustering. Because adult cells that were previously deemed to be low quality were also included in clustering, clusters with the most low-quality cells were also filtered out. In total, 1,197 clusters were removed based on these criteria after the first round of clustering ($n = 796{,}126$ cells removed). This resulted in the dataset of 1,203,850 cells, which were carried over into the second round of clustering (Extended Data Fig. 3a).

After the second round of clustering, we observed 928 clusters. All clusters were then assigned supertype identities using majority membership from the final version of annotations from the ABC-WMB atlas. Annotated clusters were then filtered out using class-level quality metrics as following: clusters that belong to Immune, Vascular and Astro-Epen classes with $GC_{med} < 2{,}000$ or $QC_{med} < 150$; clusters that belong to OPC-Oligo, OB-CR Glut, DG-IMN Glut and OB-IMN GABA class with $GC_{med} < 3{,}000$ or $QC_{med} < 150$; clusters that belong to remaining neuron classes with $GC_{med} < 5{,}500$ or $QC_{med} < 300$ (Extended Data Fig. 2a). After this second round of cluster-level filtering, 85 clusters were removed ($n = 41{,}776$ cells removed) and 1,162,074 cells remained in the dataset. After including immune cell clusters and ependymal and/or tanycyte clusters that underwent separate rounds of clustering as described above, the final number of clusters in the dataset was 847. These remaining cells and resultant annotations were used for all downstream analysis (Extended Data Fig. 3a).

Off-target cell types were also collected because of dissection variability, and if included in the analysis, may result in bias of age analysis if certain libraries contained more off-target cells than others. To identify and remove these cell types from downstream analysis, we performed the following. First, using all the scRNA-seq data from the ABC-WMB atlas, we calculated the number and proportion of cells in that supertype that originated from the 16 regions included in this ageing study (Fig. 1a) versus other regions. Second, supertypes with less than 30% of cells originating from the 16 regions and have fewer than 500 cells from the 16 regions (based on the ABC-WMB atlas dataset) were not included in downstream analysis. A list of these supertypes found in the ABC-WMB atlas that were excluded due to off-target concerns are listed in Supplementary Table 2. Briefly, they consist of supertypes that are mostly found in the thalamus, medulla and olfactory regions, which were regions not intentionally targeted in this study.

Identifying age-associated differentially expressed genes. Age-associated differentially expressed genes were calculated using the R package MAST[23] (v.1.20.0), a widely used statistical framework designed for modelling biological effects from scRNA-seq data.

Differentially expressed genes were calculated at the subclass, supertype and cluster levels (Supplementary Table 3). For all tests, only genes that were expressed at a frequency of more than 10% were tested (that is, only genes expressed in at least 10% of query cells were included). Only subclasses with at least 50 aged and 50 adult cells were evaluated for differentially expressed genes. To decrease running time, for large subclasses, we subsampled them to a maximum of 2,000 cells per age.

At the subclass level, we used the following statistical model to model the effect of age on gene *y* including various covariates:

$$\text{Model}: y \sim \text{age} + \text{sex} + z(\log(\text{gc})) + z(\log(\text{qc})) + \text{intercept}$$

where age and sex are all categorical variable each with two levels, and gene detection (gc) and QC score (qc) are log transformed and then *z*-score normalized, and the tilde (~) means distributed as. We included both gene detection and QC score in each model to account for potential effects that various FACS population plans had on library quality (Extended Data Fig. 6e,f). A likelihood ratio test was computed between each model with and without the age term to generate *P* values. These *P* values were corrected for multiple hypothesis testing with the Bonferroni correction. The effect size estimate for the age term for each model can be interpreted as the $\log_2$(fold change) ($\log_2$FC) of each gene with covariate adjustment that we refer to as 'age effect size' throughout the main body of the text.

Augur cell-type ranking analysis. Cell types at the subclass (for neuronal) and supertype (for non-neuronal) levels were ranked by R package Augur[25] (v.1.0.3), an analysis framework that prioritizes cell types most responsive to biological perturbations or conditions in single-cell genomics data. Briefly, the method selects the most variable genes from a set of single-cell data, withholds a set of cells for testing, trains classifiers with remaining cells for each cell type, and predicts withheld labels using the trained model. This is repeated over several iterations and an AUC is reported for each iteration and cell type. An AUC of 1 represents a perfectly predictive model, and an AUC of 0.5 represents a model that predicts no better than random guessing. Mean AUC values generally correlated well with the number of age-DE genes per group and are reported in Figs. 1g, 2d and 5a and Supplementary Table 2.

For AUC analysis on both neurons and non-neuronal cells, we used the following Augur parameters: feature_perc = 0.8, var_quantile = 0.9, subsample_size = 100 for non-neuronals and subsample_size = 200 for neurons. We also modified Augur's select_variance() function (which selects the highest variance genes to include in the model) to calculate dispersion (variance/mean) per gene rather than the calculation that was implemented by Augur's original function (mean/s.d.).

Pseudo-bulk analysis. We also performed differentially expressed gene analysis at the pseudo-bulk level with R package EdgeR[24] (v.3.32.1). Mean gene expression was calculated for each cell type and library combination. We fit a simple model modelling gene expression as a function of age using EdgeR's likelihood ratio test implemented using default parameters using function glmFit() and glmLRT(). Examples of logFCs calculated from EdgeR are shown in Extended Data Fig. 6a,b and correlations with age effect sizes estimated from MAST are summarized in Extended Data Fig. 6c.

Cluster odds ratio analysis. To assess whether clusters were made up of more aged or adult cells than expected by chance, we calculated OR using the numbers of aged and adult cells per cluster (Supplementary Table 2):

$$\text{OR} = (a/c)/(b/d)$$

where *a* is the number of aged cells in the cluster, *b* is the number of adult cells in the cluster, *c* is the number of aged cells in the class minus *a* and *d* is the number of adult cells in the class minus *b*. For tanycytes, *b* and *d* were calculated at the subclass level rather than the class level due to inclusion of extra cells from the ABC-WMB atlas that were not included for other cell types.

The $\log_2$OR values for non-neuronal clusters are summarized in Fig. 2b. Positive $\log_2$OR indicate clusters that are more biased towards aged cells than expected by chance (that is, age-enriched), whereas negative $\log_2$OR indicated clusters that are more biased towards young adult cells than expected by chance (that is, age-depleted). We highlight clusters with abs($\log_2$OR) > 2.5.

UMAP projection. We used principal components calculated from principal component analysis (PCA) to calculate UMAPs for different groups of cells[90]. For UMAPs with more than 100,000 cells, we performed PCA based on the imputed gene expression matrix of genes based on top marker genes from each cluster within each grouping of cells. For UMAPs with fewer than 100,000 cells, no imputation was used. Three parameters that can be adjusted when generating UMAPs include (1) the number of principal components that are used to calculated projections; (2) nn.neighbours, the size of the local neighbourhood of cells the UMAP will look at when trying to learn the structure of the data and (3) md, the minimum distance apart that cells are allowed in low-dimensional resolution. For all UMAPs, the top 150 principal components were then selected, and principal components with more than 0.7 correlation with the technical bias vector (defined as $\log_2$(gene count) for each cell) were removed. Each PCA was run with a unique gene list and each UMAP was run with a different set of nn.neighbours and md parameters. The parameters used for each PCA/UMAP were as follows: 6,446 genes, nn.neighbours = 20, md = 0.5 for the global UMAP (Fig. 1); 984 genes, nn.neighbours = 20, md = 0.5 for the OPC-Oligo UMAP (Fig. 3); 1,884 genes, nn.neighbours = 5, md = 0.5 for the Immune UMAP (Extended Data Fig. 10); 1,806 genes, nn.neighbours = 20, md = 0.5 for the Astro-Epen UMAP (Fig. 4); 401 genes, nn.neighbours = 5, md = 0.5 for the tanycyte and ependymal cell UMAP (Fig. 4); 1,169 genes, nn.neighbours = 5 and md = 0.5 for the HY (hypothalamus) neuron UMAP (Fig. 5).

Constellation plots. The global relatedness between cell types was visualized with constellation plots, which we had implemented previously[3,20]. To generate the constellation plot, each transcriptomic cluster was represented by a node (circle), whose surface area reflected the number of cells within the subclass in $\log_{10}$ scale. The position of each node was based on the centroid position of the corresponding cluster in UMAP coordinates. The relationships between nodes were indicated by edges that were calculated as follows. For each cell, 15 nearest neighbours in reduced dimension space were determined and summarized by cluster. For each cluster, we then calculated the fraction of nearest neighbours that were assigned to other clusters. The edges connected two nodes in which at least one of the nodes had more than 5% of nearest neighbours in the connecting node. The width of the edge at the node reflected the fraction of nearest neighbours that were assigned to the connecting node and was scaled to node size. For all nodes in the plot, we then determined the maximum fraction of 'outside' neighbours and set this as edge width that was 100% of node width. The function for creating these plots, plot_constellation included in the R package scrattch.bigcat.

GO enrichment analysis. GO term enrichment was performed using the R package gprofiler2 (ref. 91) (v.0.2.2). The function gost was implemented using parameter 'ordered = T' to perform enrichment analysis using a hypergeometric test followed by correction for multiple testing on positive and negative age-DE genes separately. We queried all databases included in gprofiler's default implementation (GO:molecular function, GO:biological process, GO:cellular component, KEGG, Reactome, TRANSFAC, miRTarBase, Human Protein Atlas, Human Phenotype Ontology). Only GO terms were shown in

main figures here, but all significant terms from all databases are included in Supplementary Table 4. An adjusted *P* value cutoff of 0.01 was used to determine significant terms. Multiple testing correction was performed using gprofiler2's default algorithm g:SCS (set counts and sizes), which accounts for the dependency of multiple tests in the context of enrichment analysis by taking into account the overlap of functional terms. It is more conservative than false discovery rate, but less strict than the Bonferroni correction[91]. All enrichment analysis *P* values reported in the figures have been adjusted using this method. GO significance scores shown in Fig. 6 represent the $-\log_{10}$(*P* value) for each term. Positive scores were enriched in genes observed to be increasing with age and negative scores were enriched in genes observed to be decreasing with age.

Resolve spatial transcriptomics

Resolve Molecular Cartography overview. All in situ spatial RNA data shown here were generated by Resolve Biosciences with their commercially available Molecular Cartography platform. Four total Molecular Cartography experiments were performed (RSTE1–4), each with a different panel of 100 genes and targeting different region(s) of the brain (Extended Data Fig. 5). For RSTE1, four different regions of the brain (cortex, striatum, midbrain and hindbrain) were imaged in both sexes and both ages (2 and 18 months), with two replicate brains per condition and two technical replicates per brain. The technical replicates were plotted and analysed as independent replicates in all figures. For RSTE2, the RSP and hippocampus were imaged in both sexes and ages, with four replicate brains per condition. For RSTE3 and RSTE4, the hypothalamus was imaged in both sexes and both ages, with four replicate brains per condition. Brain dissection and cryosectioning for Molecular Cartography experiments were performed at the Allen Institute for Brain Science in Seattle, WA, samples were stored at −80 °C for 1–3 days, and then shipped overnight to Resolve Biosciences in San Jose, CA, USA where the Molecular Cartography protocol was performed. Spot data were then made available 1–2 weeks after receipt of tissue. Data analysis was performed at the Allen Institute using methods detailed below. Briefly, transcript data were segmented into cells, cells were filtered based on quality metrics generated from segmentation and mapping, and downstream analysis and visualization was performed.

Brain dissection and freezing. Mice used for spatial experiments were housed and kept in same conditions as those used for scRNA-seq described above. Mice were transferred from the vivarium to the procedure room with efforts to minimize stress during transfer. Mice were anaesthetized with 5% isoflurane. A grid-lined freezing chamber was designed to allow for standardized placement of the brain within the block to minimize variation in sectioning plane. Chilled optimal cutting temperature compound (OCT) was placed in the chamber, and a thin layer of OCT was frozen along the bottom by brief placement of the chamber in a dry ice and ethanol bath. The brain was rapidly dissected and placed into the prechilled OCT for roughly 2 min to acclimate to the cold before freezing. The orientation of the brain was adjusted under a dissecting scope, and the freezing chamber containing OCT and brains was placed into a dry ice and ethanol bath for freezing. After freezing, the brains were vacuum sealed and stored at −80 °C.

Cryosectioning. The fresh-frozen adult and aged brains were sectioned at 10 µm on Leica 3050 S cryostats. The OCT block containing a fresh-frozen brain was trimmed in the cryostat until reaching the desired region of interest. Sections were placed onto coverslips provided by Resolve Biosciences. Two replicate sections were collected sequentially: one as the primary sample and the other as a backup.

Gene panel design. The Molecular Cartography platform allows 100 genes per experiment for spatial RNA profiling. Each of the four Molecular Cartography experiments we ran was designed to target different regions and cell types in the adult and aged brains. Therefore, for each experiment we used different gene panels, which were compiled through a combination of automated and manual processes. Glutamatergic and GABAergic neuronal class markers *Slc17a7*, *Slc17a6*, *Gad1* and *Gad2* and major non-neuronal subclass markers *Aqp4*, *Apod*, *Sox10*, *Pdgfra*, *Enpp6*, *Opalin*, *Dcn*, *Pecam1*, *Ctss*, *Mrc1*, *Kcnj8*, *Pdgfrb* and *Acta2* were included for all four Resolve experiments. The remaining genes in each panel were then customized for each of the four experiments. RSTE1 targeted non-neuronal types in different major brain structures. RSTE2 primarily targeted neurons in the isocortex and hippocampus, as well as certain non-neuronal types. RSTE3 primarily targeted tanycytes and ependymal cells around the V3 of the hypothalamus. RSTE4 primarily targeted the neurons around the V3. The function select_N_markers included in the R package scrattch.hicat was used to select markers for all relevant subclasses and clusters in each experiment. The top age-DE genes were also included for relevant subclasses within each panel, as well as more genes of interest selected from previous literature.

Cell segmentation. Cells were segmented using a combination of open-source software Cellpose[92] (v.2.1.0) and Baysor[93] (v.0.6.2). Cellpose uses a generalist algorithm for segmenting cells from images of cellular stains as input. Baysor uses a transcript-driven algorithm to draw cell boundaries based on transcript data alone while also having the option of integrating previous knowledge from stained images into the process. First, images of DAPI stains from each of the tissue samples were used as input for Cellpose using the following parameters: --pretrained_model = nuclei, --diameter = 0. The output of Cellpose was saved as a TIF file and used as a prior for the Baysor segmentation algorithm. Baysor was run with the following input parameters: -m 30, -s 50.

In situ data preprocessing. All segmented cells were mapped to the ABC-WMB cell-type taxonomy with the same method used for scRNA-seq data as described above. The four RSTE datasets were filtered for high-quality cells using a combination of thresholds for mapping confidence score, segmentation confidence score (from Baysor), number of transcripts and gene detection. Owing to the variable gene panels and brain regions across the four RSTE datasets, we used a different set of filter criteria for each experiment. For RSTE1, neurons with between more than 50 and fewer than 3,000 transcripts, more than 0.9 average segmentation confidence and three or more unique genes were retained; non-neuronal cells and IMNs between more than 10 and fewer than 1,000 transcripts, more than 0.9 average segmentation confidence and three or more unique genes were retained. For RSTE2, neurons with between more than 50 and fewer than 3,000 transcripts, more than 0.9 average segmentation confidence, three or more unique genes and more than 0.4 mapping correlation score were retained; non-neuronal cells between more than 10 and fewer than 1,000 transcripts, more than 0.9 average segmentation confidence, three or more unique genes and more than 0.4 mapping correlation score were retained; IMNs between more than 100 and less than 1,000 transcripts, more than 0.9 average segmentation confidence, three or more unique genes and more than 0.4 mapping correlation score were retained. For RSTE3, neurons with more than 100 transcripts, more than 0.95 average segmentation confidence and three or more unique genes were retained; tanycytes with more than 300 transcripts, more than 0.95 average segmentation confidence and ten or more unique genes were retained; astrocytes with more than 50 transcripts, more than 0.95 average segmentation confidence and ten or more unique genes were retained; remaining non-neuronal cells with more than 30 transcripts, more than 0.95 average segmentation confidence and three or more unique genes were retained. For RSTE4, neurons with more than 50 transcripts, more than 0.95 average segmentation confidence and three or more unique genes were retained; non-neuronal cells with more than 20 transcripts, more than 0.95 average segmentation confidence and three or more unique

genes were retained. Cell counts for each experiment before and after quality filtering are shown in Extended Data Fig. 5. Quantification of select cell-type densities (Extended Data Fig. 8) was performed across Resolve image tiles. A single imaging tile is equivalent to 296 × 296 µm. The ranges of number of tiles imaged per region per RSTE dataset are listed in Extended Data Fig. 5.

Reporting summary

Further information on research design is available in the Nature Portfolio Reporting Summary linked to this article.

Data availability

Primary and processed scRNA-seq data have been deposited to the Neuroscience Multi-omic Data Archive (NeMO), https://nemoarchive.org/, and can be accessed at https://assets.nemoarchive.org/dat-61kfys3. Primary spatial transcriptomics data have been deposited to Brain Image Library (BIL), https://www.brainimagelibrary.org/, and can be accessed at https://doi.org/10.35077/g.1157. Source data are provided with this paper.

Code availability

Analysis methods used in the paper from R packages scrattch.hicat and scrattch.bigcat are available at https://github.com/AllenInstitute/scrattch.hicat and https://github.com/AllenInstitute/scrattch.bigcat. All the analysis scripts used in this study are available at https://github.com/AllenInstitute/mouse_aging_scRNAseq.

85. Daigle, T. L. et al. A suite of transgenic driver and reporter mouse lines with enhanced brain-cell-type targeting and functionality. *Cell* **174**, 465–480.e22 (2018).
86. Madisen, L. et al. A robust and high-throughput Cre reporting and characterization system for the whole mouse brain. *Nat. Neurosci.* **13**, 133–140 (2010).
87. Tasic, B. et al. Shared and distinct transcriptomic cell types across neocortical areas. *Nature* **563**, 72–78 (2018).
88. Frankish, A. et al. GENCODE reference annotation for the human and mouse genomes. *Nucleic Acids Res.* **47**, D766–D773 (2019).
89. McGinnis, C. S., Murrow, L. M. & Gartner, Z. J. DoubletFinder: doublet detection in single-cell RNA sequencing data using artificial nearest neighbors. *Cell Syst.* **8**, 329–337.e4 (2019).
90. McInnes, L., Healy, J., Saul, N. & Großberger, L. UMAP: uniform manifold approximation and projection. *J. Open Source Softw.* **3**, 861 (2018).
91. Raudvere, U. et al. g:Profiler: a web server for functional enrichment analysis and conversions of gene lists (2019 update). *Nucleic Acids Res.* **47**, W191–W198 (2019).
92. Stringer, C., Wang, T., Michaelos, M. & Pachitariu, M. Cellpose: a generalist algorithm for cellular segmentation. *Nat. Methods* **18**, 100–106 (2021).
93. Petukhov, V. et al. Cell segmentation in imaging-based spatial transcriptomics. *Nat. Biotechnol.* **40**, 345–354 (2022).

Acknowledgements We are grateful to the Transgenic Colony Management, Lab Animal Services, Molecular Biology, Tissue Processing and Histology teams at the Allen Institute for technical support. We thank D.-W. Kim, J. Mich and J. Buchanan for their feedback on the paper. The research was funded by grants from the National Institutes of Health (NIH), specifically, grant no. R01AG066027 from National Institute on Aging to H.Z. and B.T., and BRAIN Initiative grant no. U19MH114830 from National Institute of Mental Health to H.Z. The content is solely the responsibility of the authors and does not necessarily represent the official views of NIH and its subsidiary institutes. This work was also supported by the Allen Institute for Brain Science. We thank the Allen Institute founder, P. G. Allen, for his vision, encouragement and support.

Author contributions H.Z. and B.T. conceptualized the project. K.J. led data generation and analyses. K.J., Z.Y., C.T.J.v.V., S.T.B., G.B., D.C., T.C., M.C., M. Departee, M. Desierto, J. Gloe, N.G., J. Guzman, D.H., E.L., T.P., M.R., K.R., J. Sevigny, N.S., L.S., J. Sulc, A.T., H.T., B.L., N.D., K.A.S., B.T. and H.Z. generated scRNA-seq data. K.J., Z.Y., C.T.J.v.V., A.B.C., R.C., J. Goldy, C.L., K.A.S., B.T. and H.Z. processed and analysed scRNA-seq data. K.J., A.G., A.R., B.T. and H.Z. generated Resolve data. K.J., Z.Y., B.T. and H.Z. processed and analysed Resolve data. E.S.K., K.G., S.M.S., K.A.S. and L.E. carried out project management. Z.Y., C.T.J.v.V., K.R., B.L., S.M.S., N.D., L.E., K.A.S., B.T. and H.Z. were repsonsible for management and supervision. K.J., Z.Y., C.T.J.v.V., B.T. and H.Z. wrote the manuscript and generated the figures. K.J., Z.Y., C.T.J.v.V., E.S.K., B.T. and H.Z. reviewed and edited the manuscript.

Competing interests H.Z. is on the scientific advisory board of MapLight Therapeutics, Inc. The other authors declare no competing interests.

Additional information

Supplementary information The online version contains supplementary material available at https://doi.org/10.1038/s41586-024-08350-8.

Correspondence and requests for materials should be addressed to Bosiljka Tasic or Hongkui Zeng.

Peer review information *Nature* thanks John Campbell, Vincent Prevot and the other, anonymous, reviewer(s) for their contribution to the peer review of this work. Peer reviewer reports are available.

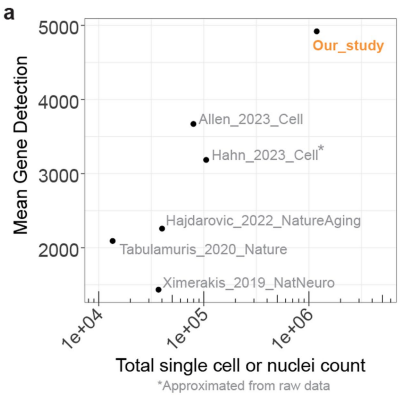

b

Broad region	This study	Hahn; Cell 2023 (bulk)	Tabula Muris Consortium; Nature 2020	Allen; Cell 2023
Isocortex	**Yes**	Yes*	Yes	Yes
Olfactory		Yes*		
Hippocampal formation	**Yes**	Yes	Yes	
Striatum	**Yes**	Yes	Yes	Yes
Palidum	**Yes**			
Thalamus		Yes*		
Hypothalamus	**Yes**	Yes*		
Midbrain	**Yes**			
Hindbrain	**Yes**	Yes*		
Cerebellum		Yes*	Yes	
White matter	**Yes**	Yes*		Yes

* bulk only

Extended Data Fig. 1 | Comparison of this study to other published mouse aging scRNA-seq datasets. (a) Scatter plot of mean gene detection plotted against total cell or nucleus count from major scRNA-seq datasets published within the last 5 years. **(b)** Table documenting major brain structures profiled within each study. Grey cells denote regions that were profiled with bulk-seq rather than single-cell methods.

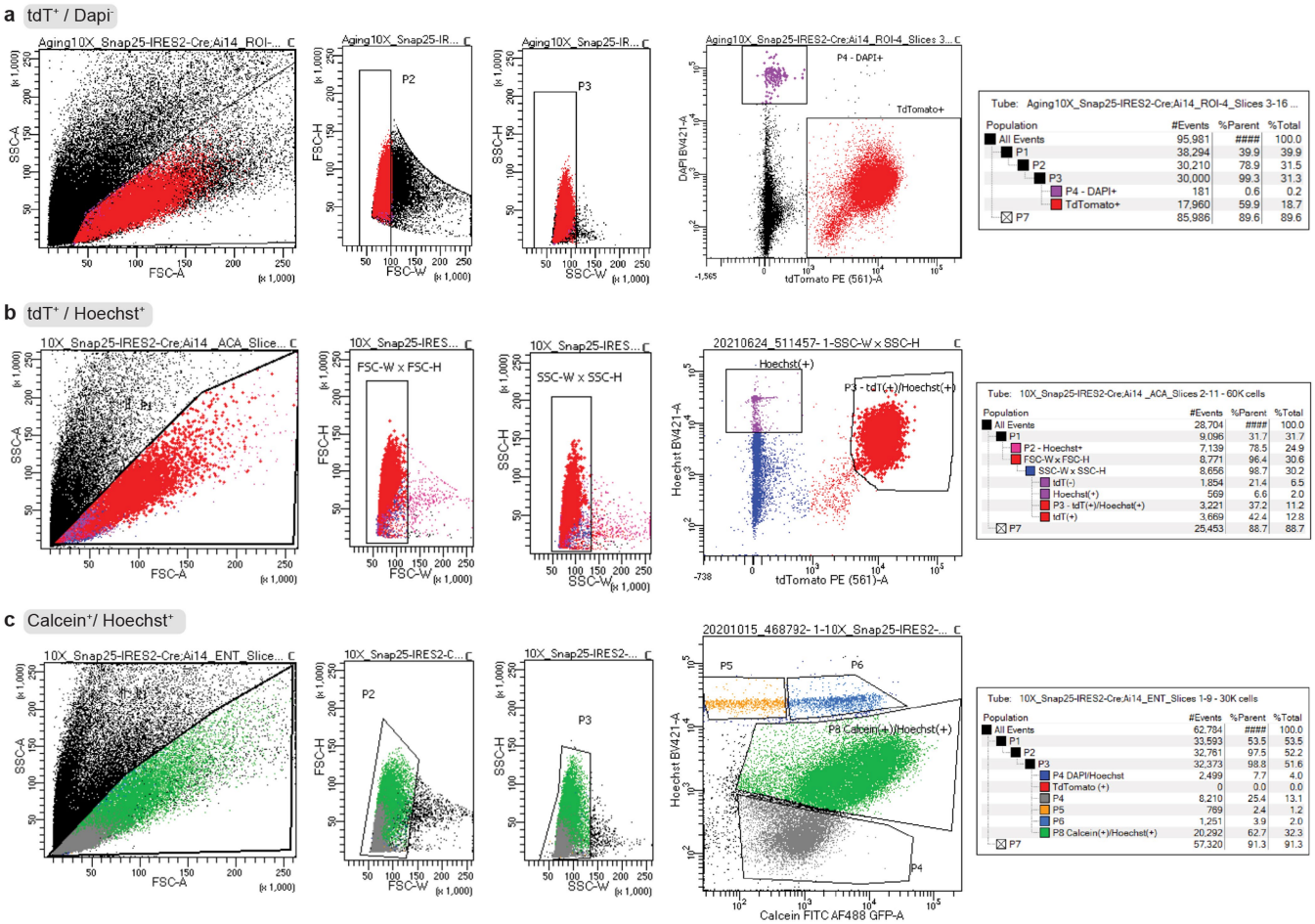

Extended Data Fig. 2 | FACS gating strategies. (a-c) Representative flow cytometry data illustrating the gating strategy for FACS purification of cells. Neurons were enriched using tdTomato signal combined with DAPI (a) or Hoechst (b) signal. Live cells were enriched using Calcein and Hoechst (c).

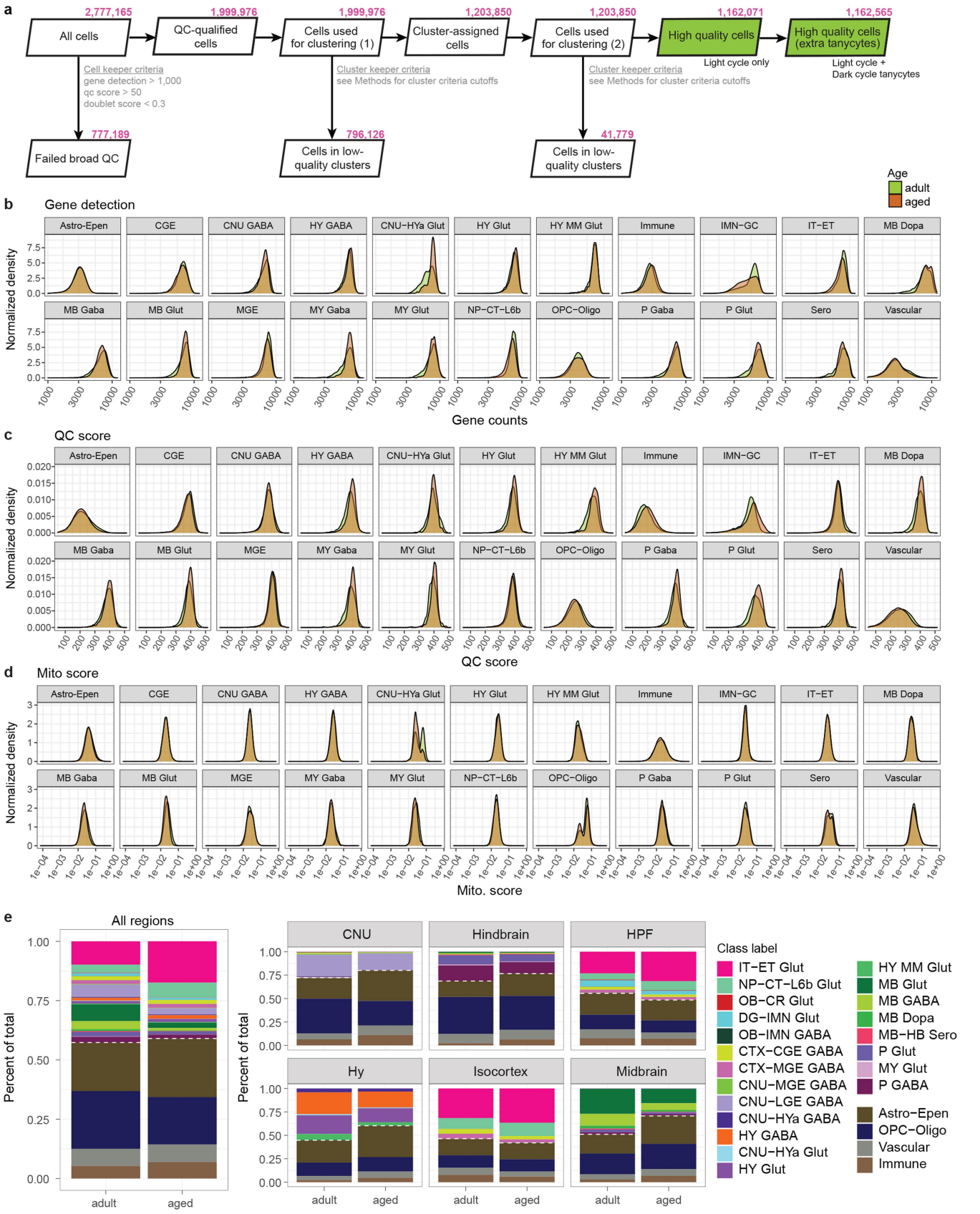

Extended Data Fig. 3 | Data pre-processing workflow and quality control. **(a)** Workflow for pre-processing of scRNA-seq data. Cells retained at each step are indicated in pink. **(b-d)** Normalized density distribution of gene detection (b), QC score (c), and mito. score (d) per cell across different cell classes and ages. These quality scores show little variation between aged and adult cells, except for a small number of cell classes such as higher gene detection in adult IMN-GC (immature neurons and granule cells) compared to aged IMN-GC in panel b. **(e)** Proportion of cells in each class across all regions and within each major brain structure. Dashed white lines denote the separation between neurons and non-neuronal cell classes.

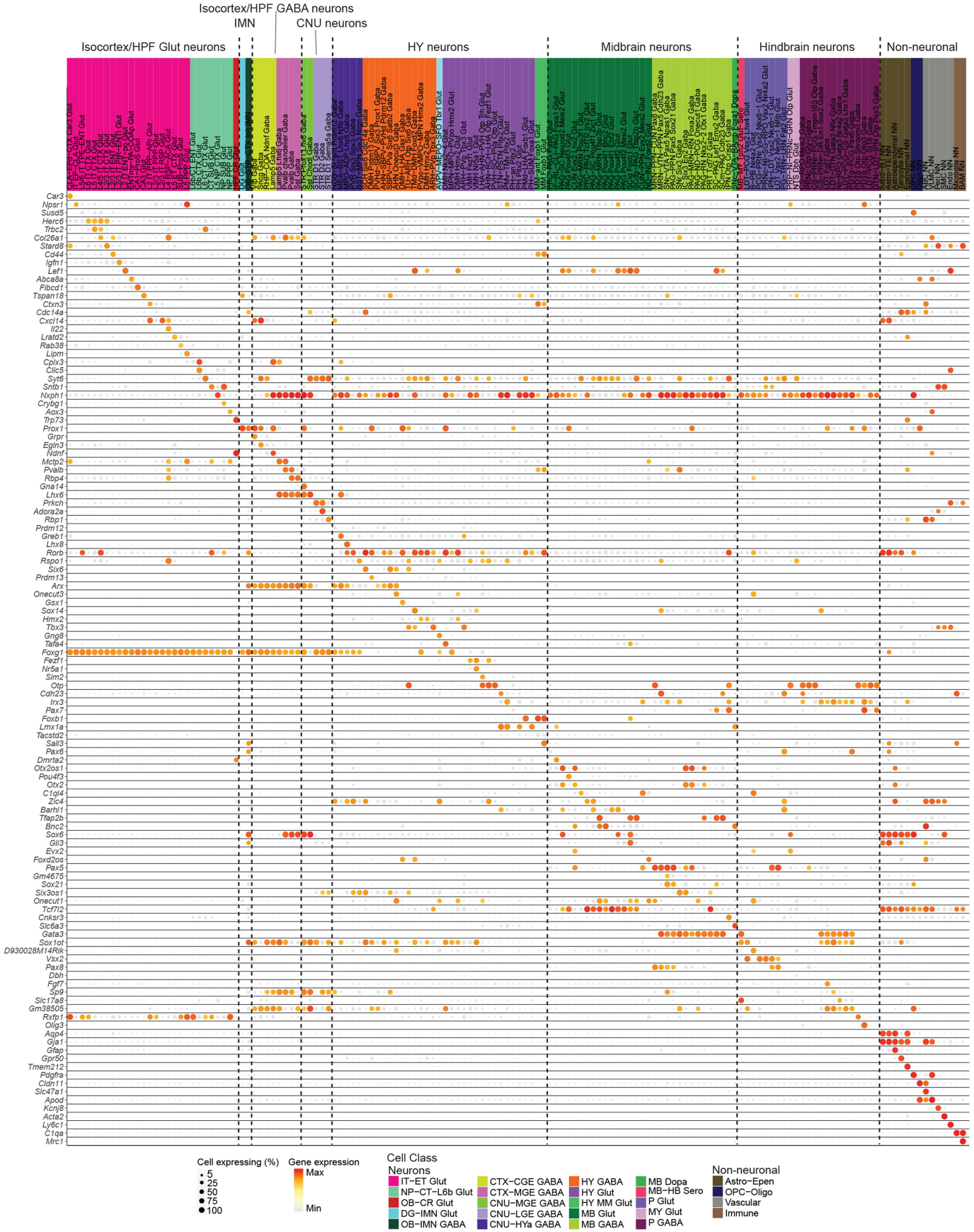

Extended Data Fig. 4 | Cell subclass marker genes. Dot plot of marker gene expression for cell subclasses analyzed in this study. Dot size and color indicate proportion of expressing cells and average expression level in each subclass, respectively. Subclass labels are colored by cell class.

a RSTE #1: 4 regions - CTX, STR, HB, MB

Target cell type: Oligodendrocytes, other major non-neuronal types

1 Resolve tile = 296 µm X 296 µm

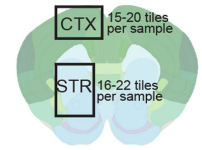

Atlas plate 40

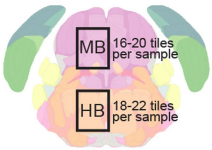

Atlas plate 102

Abca8a	Art3	Cnih2	Efna5	Grin2a	Ildr2	Mlc1	Pcolce2	Sgcd	Spock3
Acss1	Auts2	Crym	Enpp6	Grin3a	Inpp4b	Mrc1	Pdgfra	Shisa9	St6galnac5
Adam11	Brinp3	Ctss	Ephb1	Gstm1	Itga6	Nav3	Pdgfrb	Slc17a6	Sulf2
Adamts18	Ccl3	Cyp26b1	Fmo2	Hdac9	Itgb5	Neu4	Pdlim2	Slc17a7	Susd5
Adcy8	Ccl4	Dcn	Gad1	Hmgcs2	Jph4	Nkx2-9	Pecam1	Slc25a18	Svop
Adgrl3	Ccnd2	Des	Gad2	Hopx	Kcnab1	Nkx6-2	Prom1	Slc6a6	Ttll3
Aif1l	Cd24a	Dgat2	Gadd45b	Hsd11b1	Kcnj8	Nr6a1	Rasgrf2	Slc6a9	Unc13c
Apod	Cd38	Dock5	Gfap	Igfbp2	Klhl29	Nrg3	Rgs9	Snca	Ust
Aqp4	Cdh8	Dpyd	Gria1	Il23a	Maf	Nrgn	Robo1	Snhg11	Vit
Arhgap29	Cdkn1a	Dpysl3	Grik1	Il33	Mdga2	Opalin	Sema3g	Sox10	Wnk2

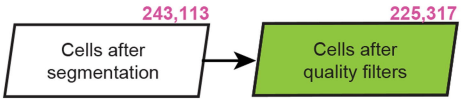

Age 2 month, 18 month X **Sex** M, F X **Regions** Ctx, Str, MB, HB X **Replicates** 2 biological, 2 technical

= 64 samples

b RSTE #2: 2 regions - RSP, HIP

Target cell type: RSP/HIP neurons

1 Resolve tile = 296 µm X 296 µm

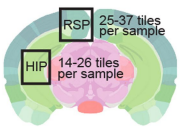

Atlas plate 83

Abcc9	Calb1	Cplx2	Fkbp3	Ildr2	Meg3	Nr1d2	Rai14	Rspo1	Sulf2
Acta2	Ccbe1	Ctnna3	Fmo2	Irf2bp2	Mgp	Nrxn1	Rasgrf2	S100b	Thsd7b
Adgrg1	Cd209a	Ctss	Fos	Itga4	Mrc1	Opalin	Rgma	Satb2	Tmem196
Alcam	Cd209b	Dbp	Frmd4b	Kcnj8	Msmo1	Pdgfra	Rgs6	Sema5b	Tpr
Aqp4	Cd74	Dcn	Gad1	Klf10	Ndufb7	Pecam1	Rims3	Slc17a6	Upk1b
Arc	Cisd1	Ddit4l	Gpc5	Lhx2	Ndufc1	Pisd	Rorb	Slc17a7	Ust
Arhgap25	Clmp	Egfl6	Hdac9	Lingo2	Nkain3	Plcl1	Rpgrip1	Slc1a3	Vstm2b
Auts2	Cntnap5a	Eif3c	Hist1h2bc	Lpar1	Npas2	Prdm8	Rpl39	Slc32a1	Wwtr1
Bcl11b	Col4a2	Enpp6	Hmcn1	Luzp2	Nptx1	Ptprk	Rprml	Sox10	Xist
C1ql3	Cox7b	F13a1	Htr4	Mbp	Nr1d1	Ptprm	Rras2	St18	Zfp536

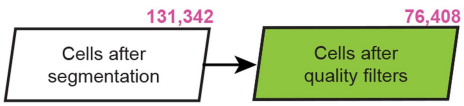

Age 2 month, 18 month X **Sex** M, F X **Regions** RSP, HIP X **Replicates** 4 biological = 32 samples

c RSTE #3: 1 region - HY

Target cell type: HY third ventricle tanycytes, ependymal cells, neurons

1 Resolve tile = 296 µm X 296 µm

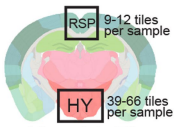

Atlas plate 72

Acta2	Bmi1	Ctss	Frzb	Id1	Meg3	Pcdh11x	Ptn	Slc1a2	Sulf1
Actn2	Bst2	Dcn	Fstl4	Id4	Mrc1	Pcp4l1	Rasgrf2	Slc22a8	Sulf2
Adap2	Capn6	Dio2	Gad1	Ifi27	Nav3	Pde7b	Rax	Slc7a10	Synpo2
Agt	Car4	Dlg2	Gad2	Ifit1	Npas3	Pdgfra	Rspo3	Slc9a9	Tenm4
Aldh1a1	Ccnd2	Dnah11	Gpr50	Igfbp7	Nsg2	Pdgfrb	Scn7a	Slco1c1	Tm4sf1
Apod	Col23a1	Efna5	Grip1	Inpp4b	Ntn4	Pdzph1	Shank2	Sox10	Tmem59l
Apoe	Col25a1	Elmo1	H2-K1	Itih5	Oasl2	Pecam1	Slc16a2	Sox2	Tmsb4x
Aqp4	Csmd1	Enpp6	Hdac9	Kcnj8	Olfml2a	Plvap	Slc17a6	Sparc	Tmtc2
B2m	Ctla2a	Fmo2	Hdc	Lmo3	Opalin	Plxdc2	Slc17a7	St6galnac5	Vcan
Bgn	Ctnna2	Frmd4b	Hkdc1	Mafb	P3h2	Prex2	Slc17a8	Stxbp6	Wdr63

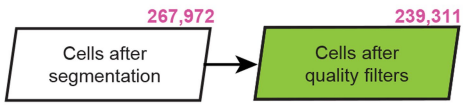

Age 2 month, 18 month X **Sex** M, F X **Regions** HY X **Replicates** 4 biological = 16 samples

2 month, 18 month X M, F X RSP X 2 biological = 8 samples

d RSTE #4: 1 region - HY

Target cell type: HY third ventricle neurons

1 Resolve tile = 296 µm X 296 µm

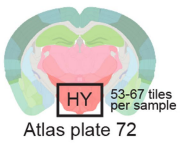

Atlas plate 72

Acta2	Bsx	Ctss	Gad2	Kcnj8	Nfix	Pde7b	Ptpn5	Six6	Sulf1
Agrp	Caln1	Dcn	Glra2	Kcnt2	Nhlh2	Pdgfra	Rasgrp2	Slc17a6	Tacr1
Agtr1a	Ccnd2	Dlx1	Glra3	Lhfp	Npy	Pdgfrb	Robo1	Slc17a7	Tbx3
Alk	Cdh12	Dnajb9	Grik1	Lncenc1	Nr1d2	Pecam1	Ror2	Slc32a1	Tcf7l2
Apod	Chchd10	Ebf3	Grm8	Lrrc9	Nr2f2	Per3	Rxfp1	Slc35f4	Tent5a
Aqp4	Cntn5	Enpp6	Hcn1	Lrrtm4	Nr5a2	Pitx2	Sall3	Sorcs1	Tmem176a
Atp6v1f	Cntnap5b	Fezf1	Hspa5	March1	Ntn1	Pomc	Satb2	Sox10	Tmem176b
Bace2	Cntnap5c	Foxd2	Isl1	Mbnl3	Opalin	Pou3f1	Selenom	Sox14	Unc13c
Bcl11b	Col25a1	Foxp2	Kazald1	Mrc1	Otp	Prlr	Sfta3-ps	Sox1ot	Xist
Bhlhe41	Cox6b1	Gad1	Kcnh8	Ndufa5	Pde3a	Prox1	Six3	Sox2	Zbtb7c

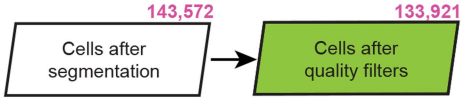

Age 2 month, 18 month X **Sex** M, F X **Regions** HY X **Replicates** 4 biological = 16 samples

Extended Data Fig. 5 | Summary of spatial transcriptomics datasets. **(a-d)** Diagram of brain regions profiled, gene panels, and pre- and post-filtered cell counts, and experimental design of Resolve spatial transcriptomic datasets 1 (RSTE1; a), 2 (RSTE2; b), 3 (RSTE3; c), and 4 (RSTE4; d). CTX, isocortex; STR, striatum; HB, hindbrain; MB, midbrain; RSP, retrosplenial area; HIP, hippocampus; HY, hypothalamus.

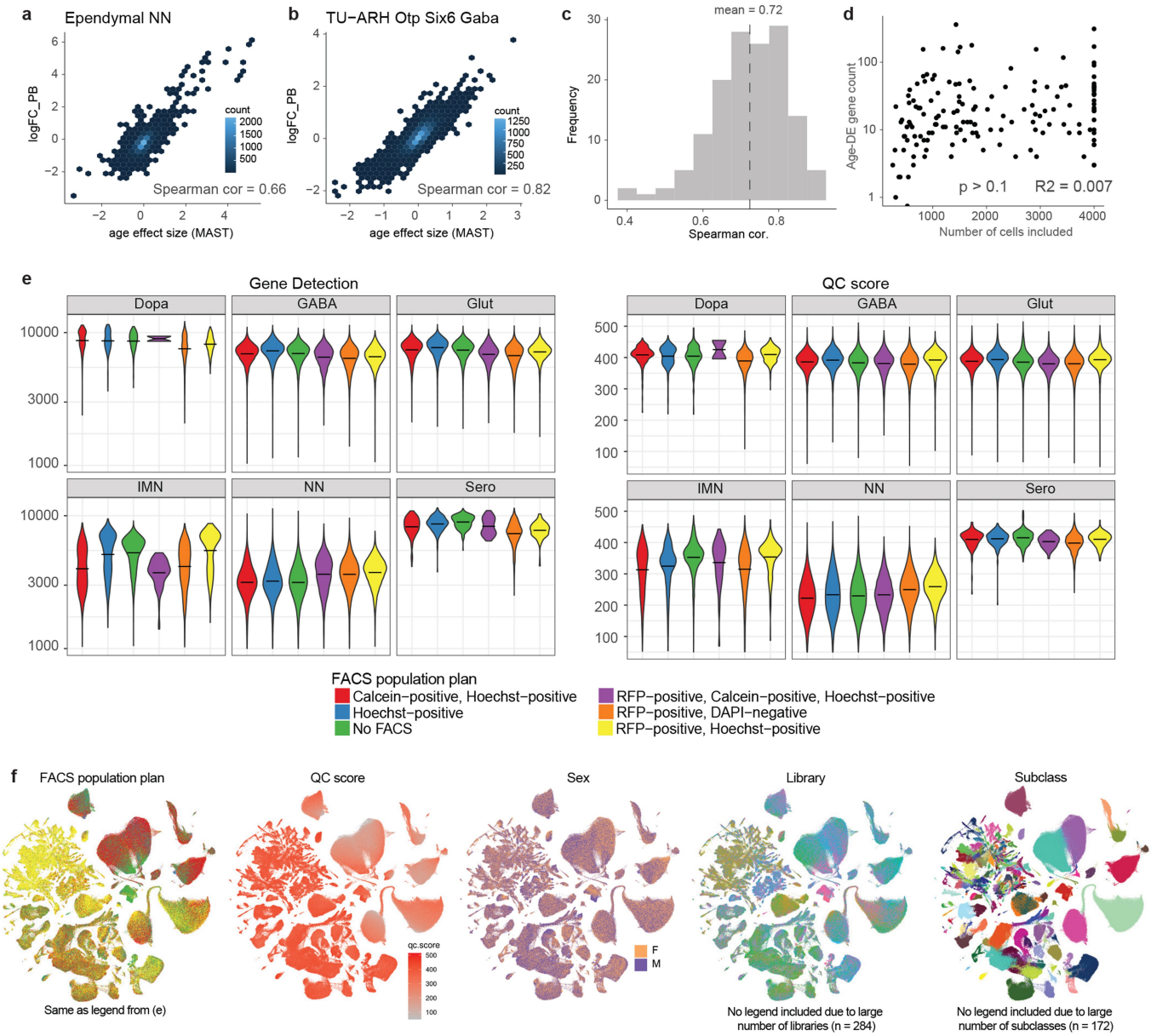

Extended Data Fig. 6 | Correlation between different DE-gene analysis methods. (a-b) Select two-dimensional density plots comparing the $\log_2$(fold change) per gene calculated from a pseudo-bulk (PB) method (y axis) versus the age effect size (comparable to $\log_2$FC; see Methods) estimated by MAST (x axis) for two subclasses: ependymal cells (a) and hypothalamic neuron subclass TU-ARH Otp Six6 Gaba (b). **(c)** Distribution of spearman correlation coefficients from all pseudo-bulk to MAST comparisons (such as those visualized in a and b) for all subclasses tested (n = 146). **(d)** Scatterplot comparing the total number of age-DE genes per subclass as identified by MAST versus the number of cells per subclass included in each test. P-value and R^2 value from linear model are shown. **(e)** Violin plots showing gene detection (left; log scale on y axis) and QC score (right; y axis) for major cell type categories and FACS population plans (x axis). **(f)** UMAP from Fig. 1 colored by additional meta data metrics, including FACS population plan, QC score, sex, library, and subclass.

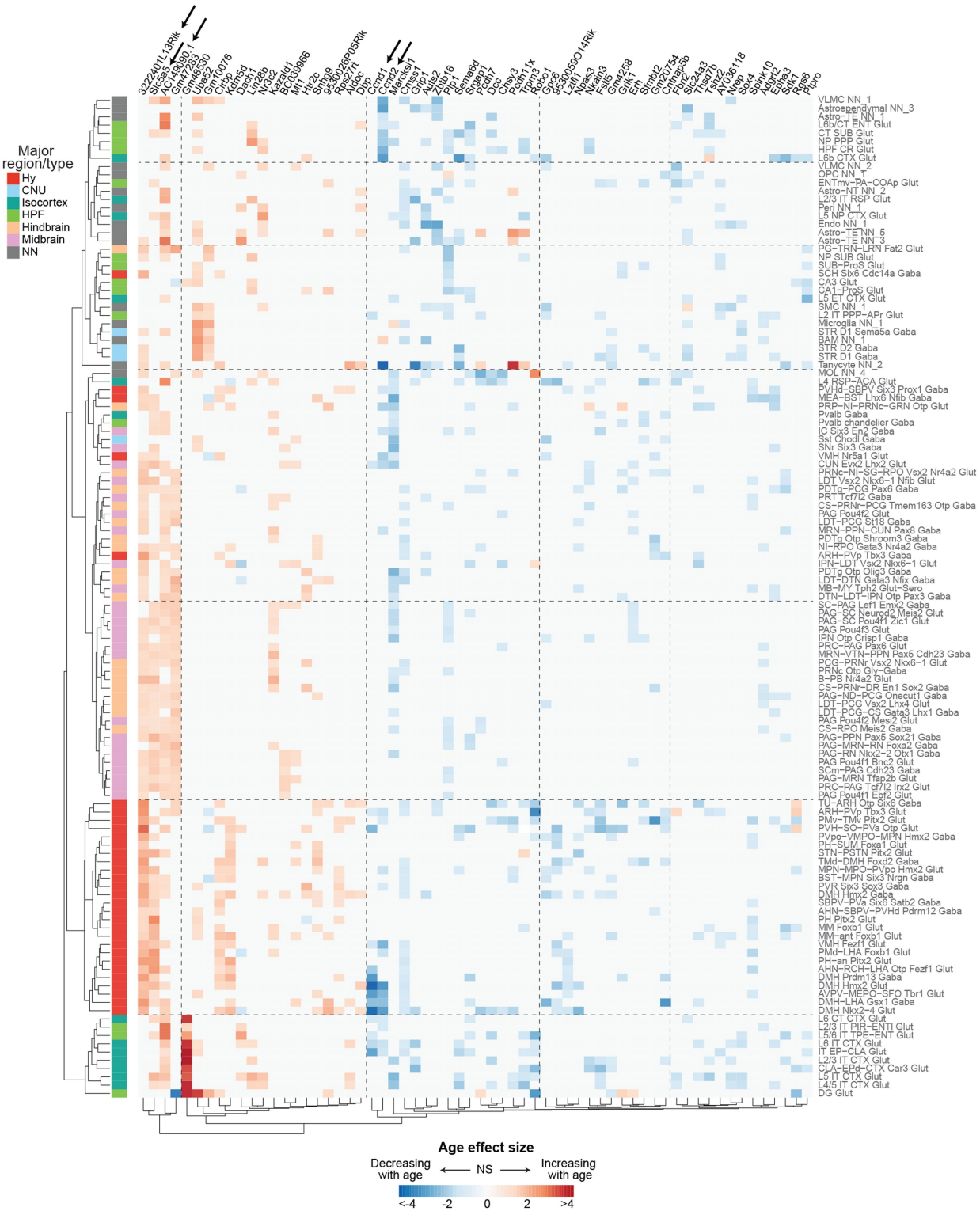

Extended Data Fig. 7 | Common age-DE genes across cell types. Heatmap of age effect sizes of the most common significant age-DE genes. DE genes that are significant in ≥ 10 cell types (corresponding to Fig. 1h) are shown. Genes and cell types are hierarchically clustered based on age effect sizes and their relatedness represented by the dendrogram.

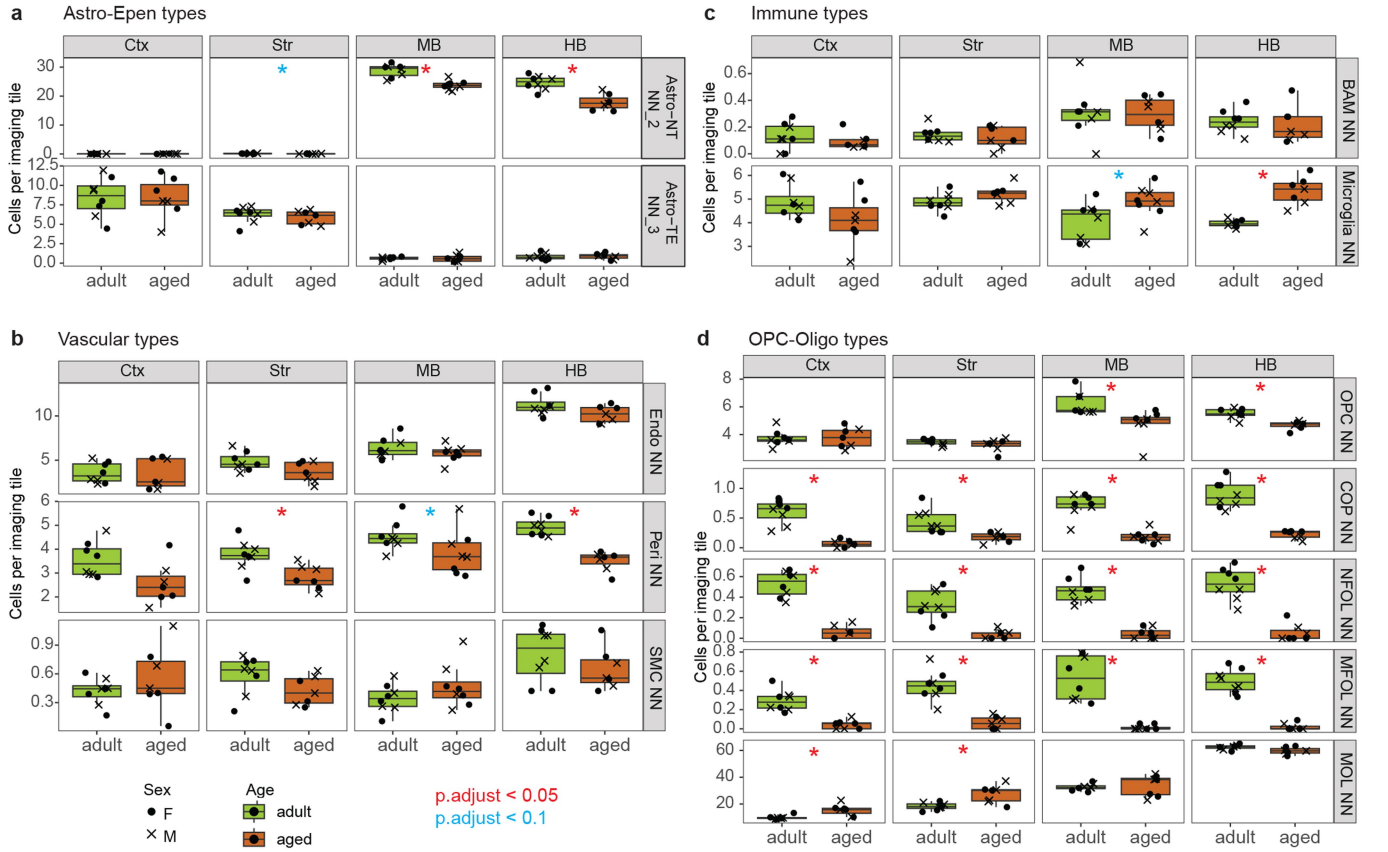

Extended Data Fig. 8 | Changes in density of major non-neuronal cell types as estimated in situ in spatial transcriptomics datasets. (a-d) Density changes of major Astro-Epen (a), Vascular (b), Immune (c), and OPC-Oligo (d) supertypes with age in isocortex (CTX), striatum (STR), midbrain (MB) and hindbrain (HB), calculated from RSTE1. Each point represents one replicate image. Significance between ages was tested with a two-sided Mann-Whitney U test. Results in all panels mostly represent n = 4 replicates from RSTE1 per sex/age/region (2 biological replicates and 2 technical replicates per brain) examined over one experiment. Male aged CTX and male aged MB have n = 3 replicates due to technical errors during imaging process. For all boxplots, the minimum, center, and maximum bound of the box represent the 25th, 50th, and 75th percentile of the data shown, respectively. The upper and lower whiskers represent the largest and smallest value within 1.5 times above or below the interquartile range, respectively.

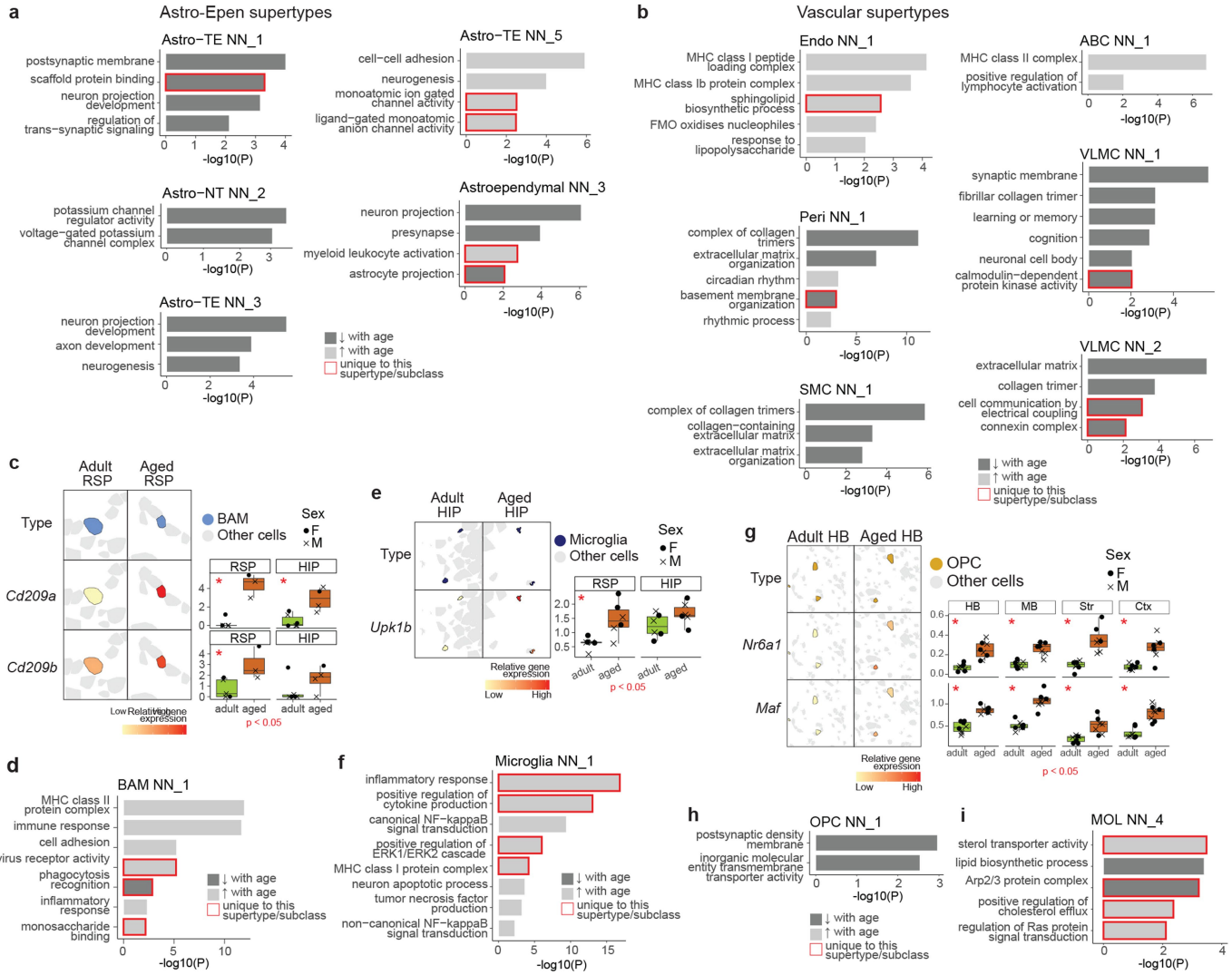

Extended Data Fig. 9 | Non-neuronal GO terms. (a-b) Select GO terms enriched in age-DE genes from Astro-Epen (a) and Vascular (b) supertypes, split by genes that increase (light grey) or decrease (dark grey) with age. **(c)** Visualization and quantification of expression of *Cd209a* and *Cd209b* in BAMs from in situ RSTE2. **(d)** Select GO terms enriched in age-DE genes from BAMs. **(e)** Visualization and quantification of expression of *Upk1b* in microglia from RSTE2. **(f)** Select GO terms enriched in age-DE genes from microglia. **(g)** Visualization and quantification of expression of *Nr6a1* and *Maf* in OPCs from RSTE1. **(h)** Select GO terms enriched in age-DE genes from OPCs. **(i)** Select GO terms enriched in age-DE genes from MOLs. Enriched GO terms were identified using hypergeometric test and corrected for multiple testing as described in the Methods. All enrichment analysis was performed across all non-neuronal supertypes and neuronal subclasses. Terms that are unique to one cell type only are highlighted with a red border. Significance between ages for spatial gene expression was tested using a two-sided Mann-Whitney U test. Results in panels c and e represent n = 4 biological replicates per sex/age from RSTE2 collected over one experiment. Only samples with > 2 BAM cells (c) or > 20 microglia (e) were included in the analysis, resulting in certain clusters per sex/age that have < 4 replicates shown. Results in panel g represent n = 4 replicates from RSTE1 per sex/age/region (2 biological replicates and 2 technical replicates per brain) examined over one experiment. Only samples with > 20 cells of that cluster were included in the analysis, resulting in certain cell types per sex/age that have < 4 replicates shown. For all boxplots, the minimum, center, and maximum bound of the box represent the 25th, 50th, and 75th percentile of the data shown, respectively. The upper and lower whiskers represent the largest and smallest value within 1.5 times above or below the interquartile range, respectively.

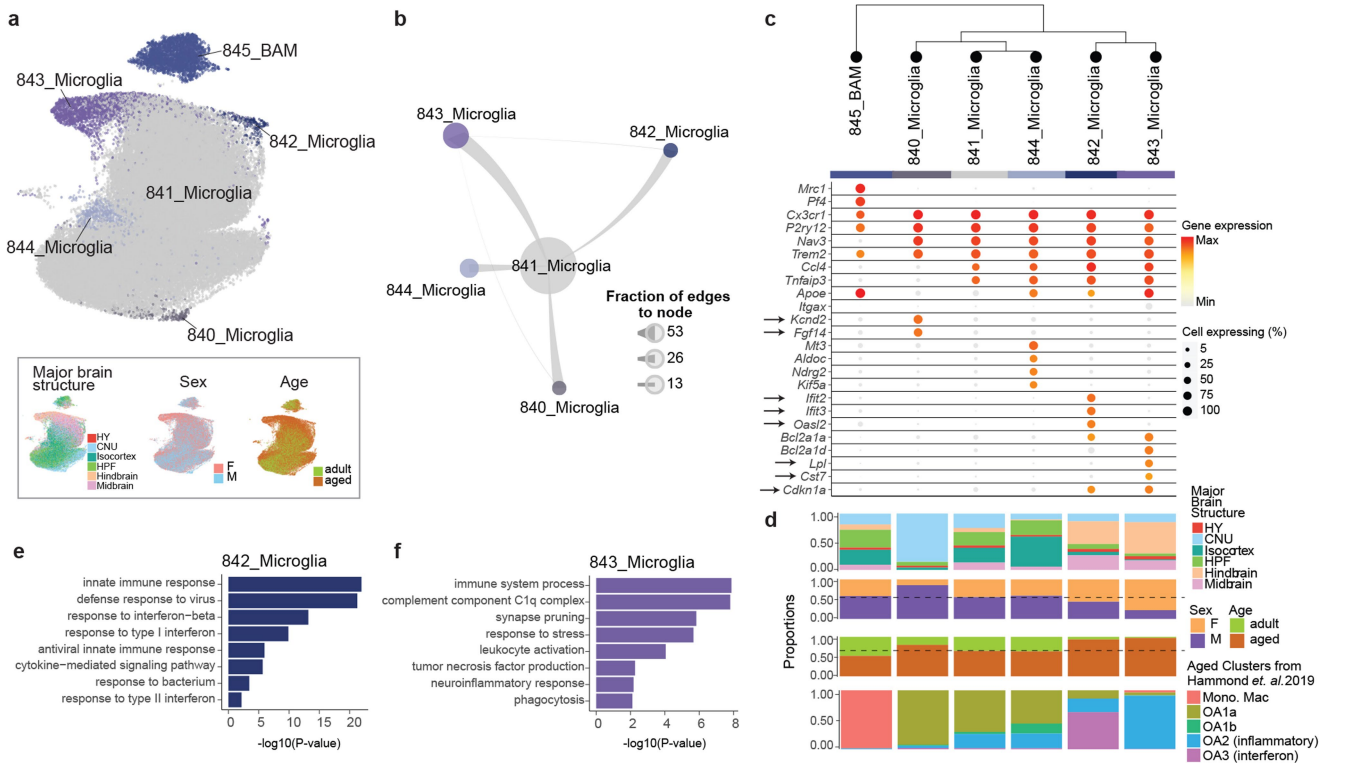

Extended Data Fig. 10 | Microglia clusters. (a) UMAP of all microglia and BAM cells colored by cluster, major brain structure, sex, and age. **(b)** Constellation plot of microglia clusters colored by cluster. **(c)** Marker gene expression in microglia and BAM clusters organized in a dendrogram calculated from cluster DE genes. **(d)** Bar plot summaries for each cluster colored by brain structure, sex, age, and mapping label from Hammond *et al.* 2019 dataset. **(e-f)** Select GO terms enriched in marker genes computed from age-enriched clusters 842_Microglia and 843_Microglia. Enriched GO terms were identified using hypergeometric test and corrected for multiple testing as described in the Methods.

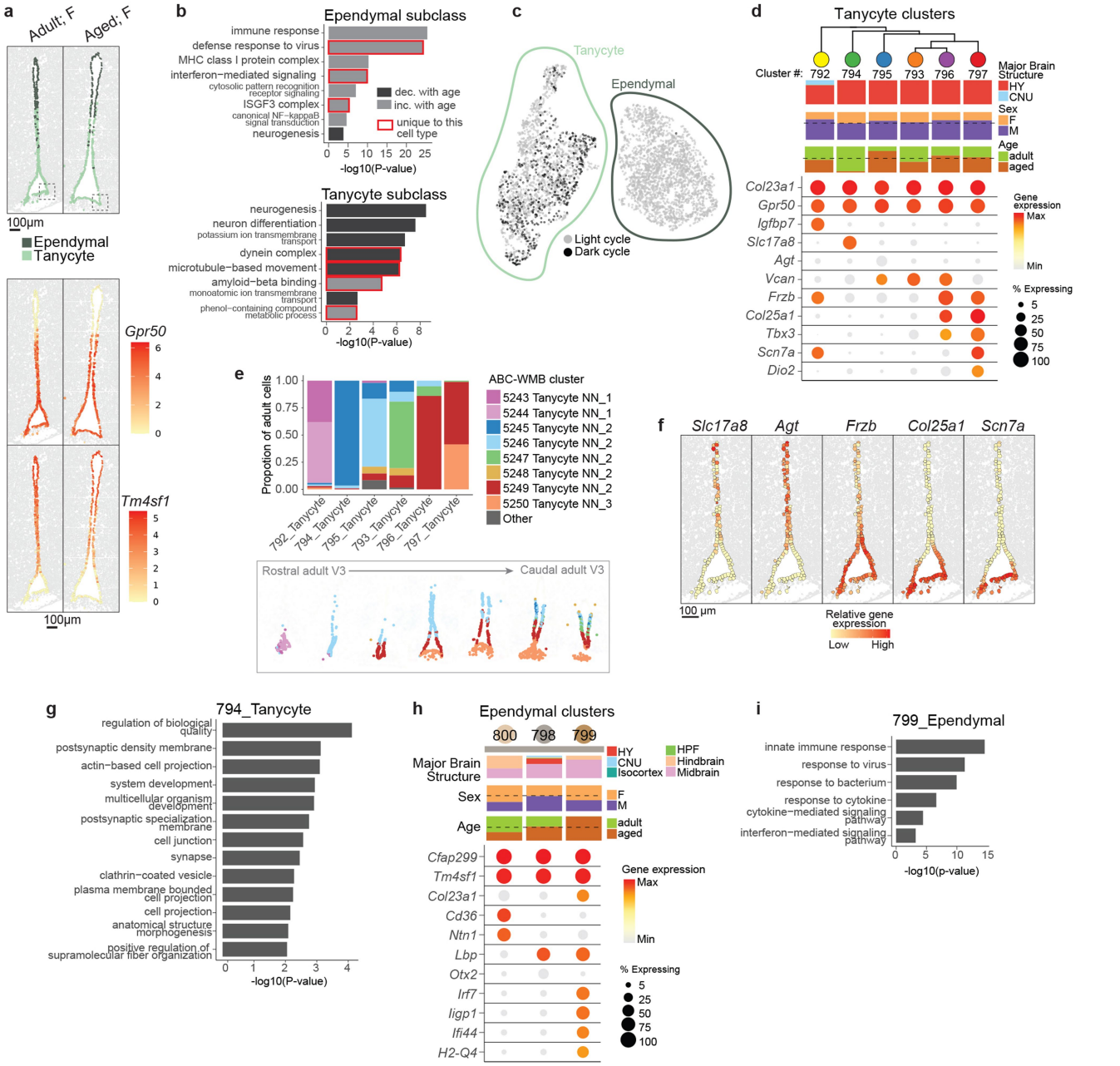

Extended Data Fig. 11 | Tanycyte and ependymal cell clusters. (a) Tanycyte and ependymal cell body locations in select samples from in situ spatial dataset RSTE3, colored by subclass label and relative expression of marker genes *Gpr50* and *Tm4sf1*. **(b)** Select GO terms enriched in age-DE genes from tancyytes and ependymal cells split by genes with increased (light grey) or decreased (dark grey) expression with age. Terms that are unique to one cell type only are highlighted with a red border. Enriched GO terms were identified using hypergeometric test and corrected for multiple testing as described in the Methods. **(c)** UMAP of tanycytes and ependymal cells with additional tanycytes included from the ABC-WMB atlas that were collected in a reversed light/dark cycle. **(d)** Marker gene expression in tanycyte clusters organized in a dendrogram calculated from cluster DE genes. Bar plots show breakdown of each cluster by brain structure, sex, and age. **(e)** Bar plot summaries for each cluster colored by brain structure, sex, age, and adult cell label from the ABC-WMB atlas and corresponding location of tanycyte clusters in the ABC-WMB atlas MERFISH data. **(f)** Representative marker gene expression for adult tanycyte subtypes from RSTE3. **(g)** GO term enrichment in marker genes from age-depleted cluster 794_Tanycyte. **(h)** Ependymal cell clusters broken down by major brain structure, sex, and age with marker gene expression for each cluster. **(i)** GO term enrichment in marker genes from age-enriched cluster 799_Ependymal. Enriched GO terms were identified using hypergeometric test and corrected for multiple testing as described in the Methods.

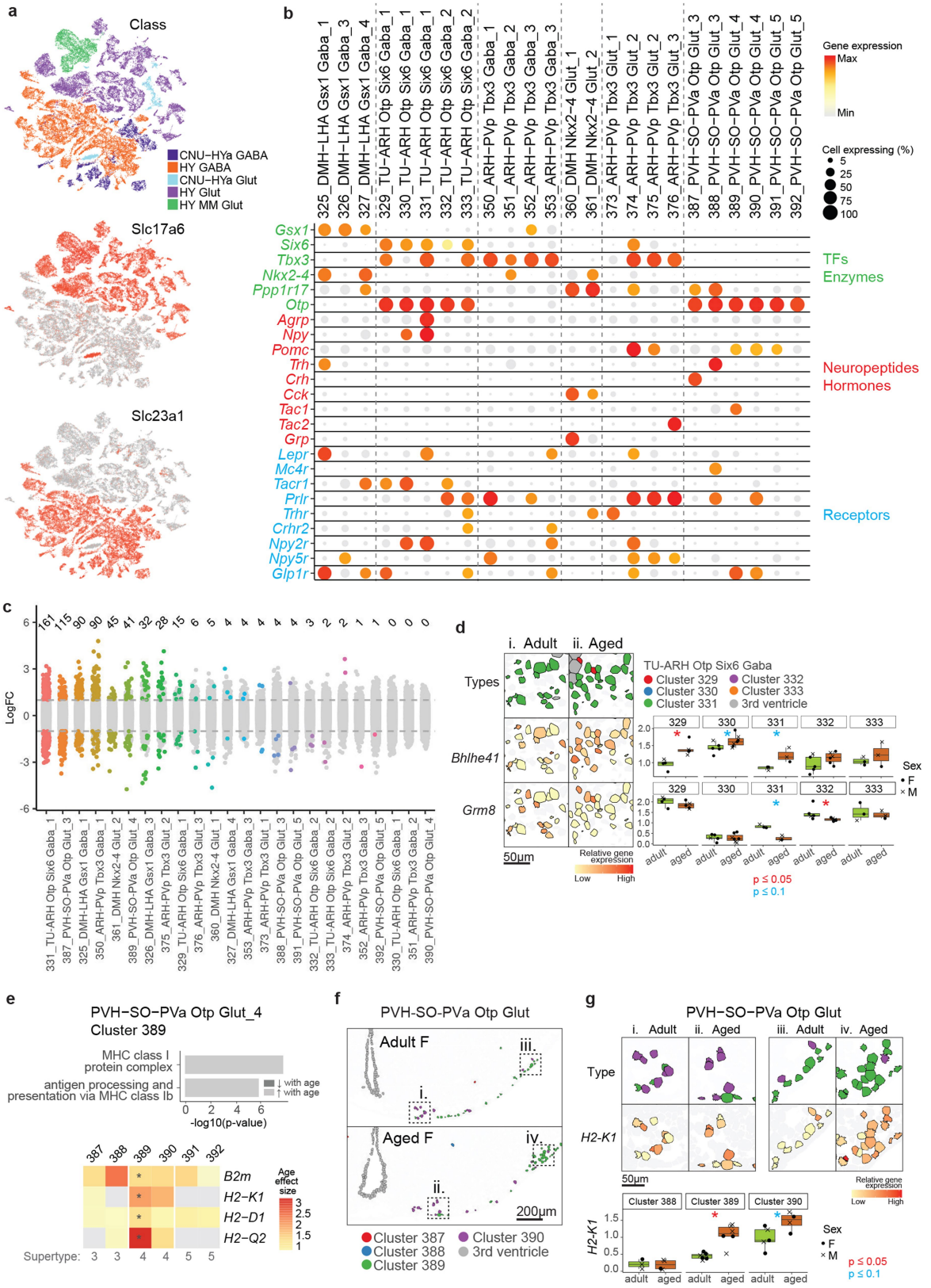

Extended Data Fig. 12 | See next page for caption.

Extended Data Fig. 12 | Hypothalamic neuronal clusters. (a) UMAP of all hypothalamic neurons in the dataset colored by class, *Slc17a6* expression (labelling glutamatergic neurons), and *Slc23a1* expression (labelling GABAergic neurons). **(b)** Expression of select transcription factors, enzymes, neuropeptides, hormones, and receptors (mostly related to energy homeostasis signaling) across hypothalamic neuron clusters from select hypothalamic neuron subclasses that show the greatest numbers of age-DE genes. **(c)** Dot plot of age effect sizes of all genes from select hypothalamic neuron clusters (same ones as shown in b). Significant age-DE genes are colored. Clusters are ordered from the most to the least number of significant age-DE genes. **(d)** Zoomed-in view of areas similar to the boxed areas shown in panel f colored by cluster or gene expression of *Bhlhe41* and *Grm8* (left), and quantification of expression of these two genes from all samples from in situ dataset RSTE4. **(e)** Select GO terms enriched in age-DE genes from cluster 389_PVH-SO-PVa Otp Glut_4 (top) and heatmap of age effect sizes for select genes belonging to major enriched GO terms for all PVH-SO-PVa Otp Glut clusters. Asterisks denote significant changes. **(f)** Spatial localization of all PVH-SO-PVa Otp Glut clusters in representative adult and aged samples from RSTE3. **(g)** Zoomed-in view of boxed areas in f colored by cluster or gene expression of (top), and quantification of expression of *H2-K1* from all samples from in situ dataset RSTE3. Enriched GO terms in e were identified using hypergeometric test and corrected for multiple testing as described in Methods. Significance between ages for spatial gene expression was tested using a two-sided Mann-Whitney U test. Results in panels d and g represent n = 4 biological replicates from per sex/age from RSTE3 and RSTE4, respectively. Only samples with > 10 cells of that cluster were included in the analysis, resulting in certain clusters per sex/age that have < 4 replicates shown. For all boxplots, the minimum, center, and maximum bound of the box represent the 25^{th}, 50^{th}, and 75^{th} percentile of the data shown, respectively. The upper and lower whiskers represent the largest and smallest value within 1.5 times above or below the interquartile range, respectively.

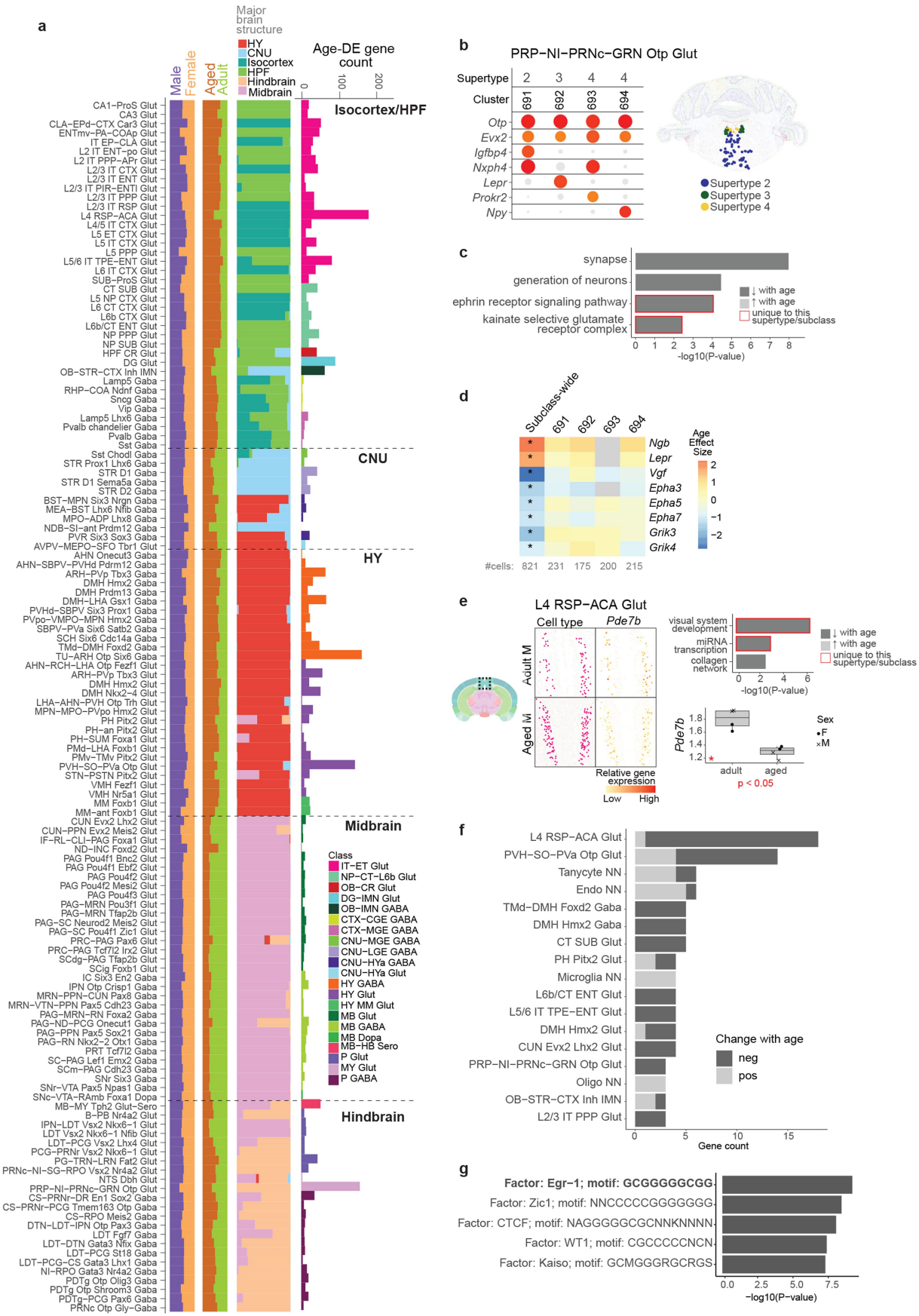

Extended Data Fig. 13 | See next page for caption.

Extended Data Fig. 13 | Age-DE genes across neuronal subclasses. **(a)** Summary of the number of age-DE genes for each neuronal subclass. Far right: The total number of age-DE genes within each subclass, colored by cell class and ordered based on broad categories. Left and center: Bar graphs summarizing the breakdown of each subclass by major brain structure, age, and sex. (**b**) Cluster marker gene expression and supertype localization from the ABC-WMB atlas for PRP-NI-PRNc-GRN Otp Glut hindbrain neuron subclass. **(c)** Select GO term enrichment in age-DE genes from PRP-NI-PRNc-GRN Otp Glut subclass. All terms are enriched in genes that have decreased expression with age. Terms that are unique to only PRP-NI-PRNc-GRN Otp Glut are highlighted with red border. **(d)** Heatmap of age effect sizes of certain genes belonging to certain terms shown in c at the subclass and cluster levels. Asterisks represent significant age-DE genes as defined by adjusted $p < 0.01$ & abs(age effect size) > 1. **(e)** Summary of age-DE gene changes in L4 RSP-ACA Glut neurons, including in situ localization of cells and expression of *Pde7b* visualized from select samples from RSTE3. Also shown are select top GO enrichment terms in age-DE genes from L4 RSP-ACA Glut. **(f)** The subclasses with greatest numbers of primary response immediate early genes (PRGs) within original age-DE gene list (the summary in a has removed PRGs). **(g)** Top transcription factor motifs from the TRANSFAC database enriched within age-DE genes from L4 RSP-ACA Glut neurons. Results in panel e represent n = 2 biological replicates from RSTE3 per sex/age from the RSP region. For all boxplots, the minimum, center, and maximum bound of the box represent the 25^{th}, 50^{th}, and 75^{th} percentile of the data shown, respectively. The upper and lower whiskers represent the largest and smallest value within 1.5 times above or below the interquartile range, respectively. Enriched GO terms from c and e and transcription factor motifs in g were identified using hypergeometric test and corrected for multiple testing as described in Methods.

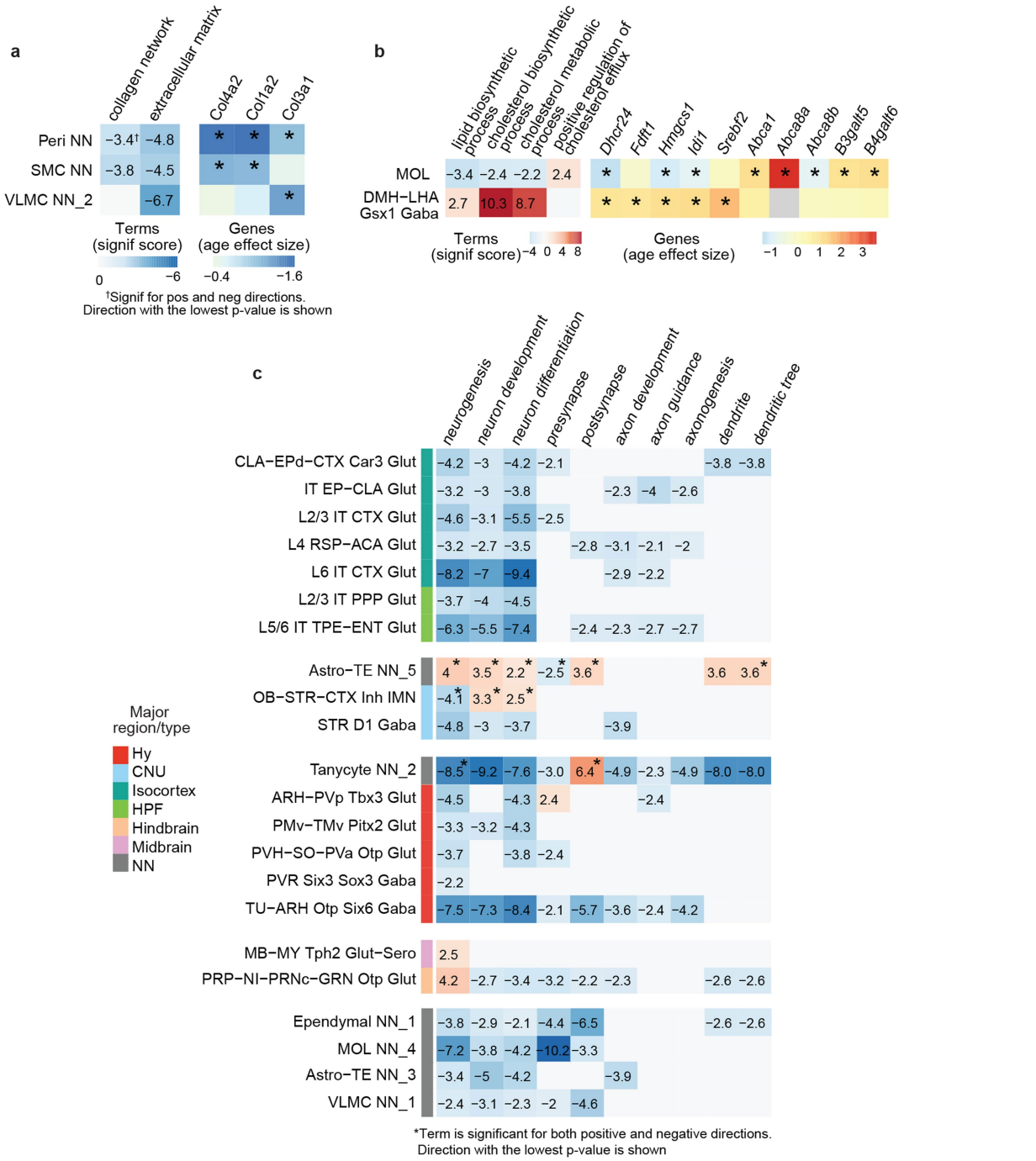

Extended Data Fig. 14 | Term enrichment scores for GO terms related to neuronal function and structure. **(a)** Heatmaps of GO significance scores of terms related to collagen network (left) and age effect sizes of select collagen genes (right) for pericytes, SMCs, and VLMC supertype 2. **(b)** Heatmaps of GO significance scores of terms related to lipid metabolism (left) and age effect sizes of select lipid metabolism genes (right) for MOLs and DMH-LHA Gsx1 Gaba neurons. **(c)** GO term enrichment was performed across all non-neuronal supertypes and neuronal subclasses, using hypergeometric test and corrected for multiple testing as described in Methods. Cell subclasses or supertypes that have significant enrichment of terms (i.e., neurogenesis, neuron development, neuron differentiation, presynapse, postsynapse, axon development, axon guidance, axonogenesis, dendrite, and dendritic tree) are included in this figure, and GO enrichment scores are plotted in the heatmap here. Negative (blue) values represent terms enriched from genes with decreased expression with age; positive (red) values represent terms enriched from genes with increased expression with age. A term enriched in both negatively and positively changing genes from a cell subclass or supertype is denoted with an asterisk, and the direction with the lowest p-value is shown.

nature portfolio

Corresponding author(s): Hongkui Zeng & Bosiljka Tasic

Last updated by author(s): Oct 19, 2024

Reporting Summary

Nature Portfolio wishes to improve the reproducibility of the work that we publish. This form provides structure for consistency and transparency in reporting. For further information on Nature Portfolio policies, see our Editorial Policies and the Editorial Policy Checklist.

Statistics

For all statistical analyses, confirm that the following items are present in the figure legend, table legend, main text, or Methods section.

n/a	Confirmed
☐	☒ The exact sample size (*n*) for each experimental group/condition, given as a discrete number and unit of measurement
☐	☒ A statement on whether measurements were taken from distinct samples or whether the same sample was measured repeatedly
☐	☒ The statistical test(s) used AND whether they are one- or two-sided *Only common tests should be described solely by name; describe more complex techniques in the Methods section.*
☐	☒ A description of all covariates tested
☐	☒ A description of any assumptions or corrections, such as tests of normality and adjustment for multiple comparisons
☐	☒ A full description of the statistical parameters including central tendency (e.g. means) or other basic estimates (e.g. regression coefficient) AND variation (e.g. standard deviation) or associated estimates of uncertainty (e.g. confidence intervals)
☒	☐ For null hypothesis testing, the test statistic (e.g. *F*, *t*, *r*) with confidence intervals, effect sizes, degrees of freedom and *P* value noted *Give P values as exact values whenever suitable.*
☒	☐ For Bayesian analysis, information on the choice of priors and Markov chain Monte Carlo settings
☒	☐ For hierarchical and complex designs, identification of the appropriate level for tests and full reporting of outcomes
☐	☒ Estimates of effect sizes (e.g. Cohen's *d*, Pearson's *r*), indicating how they were calculated

Our web collection on statistics for biologists contains articles on many of the points above.

Software and code

Policy information about availability of computer code

Data collection	scRNA-seq data was collected using the 10x Genomics Chromium Single Cell 3' v3 kit. Sequencing was performed on the Illumina NovaSeq6000. Flow cytometry data were acquired on a BD FACSAria II or FACSAria Fusion running FACSDiva v8 software. Resolve spatial transcriptomics data were acquired using the Molecular Cartography platform.
Data analysis	Raw scRNA-seq fastq files were aligned to the mouse reference (mm10/gencode.vM23) using the 10x Genomics CellRanger v6.0.0 pipeline. scRNA-seq iterative clustering and differential gene expression analysis was performed in R using the scrattch.bigcat package (https://github.com/AllenInstitute/scrattch.bigcat), v0.0.1, which also contains many functions to visualize the data together with the scrattch.vis package (https://github.com/AllenInstitute/scrattch.vis). Age-associated DE genes were calculated using the R package MAST v1.20.0 (https://github.com/RGLab/MAST), and compared with the DE genes computed at the pseudo-bulk level using edgeR v3.32.1 (https://bioconductor.org/packages/release/bioc/html/edgeR.html). Augur v1.0.3 (https://github.com/neurorestore/Augur) was used to prioritize cell types at subclass and supertype levels that are most responsive to age-associated effects. Gene ontology (GO) term enrichment was performed using the R package gprofiler2, v0.2.2. Raw Resolve data were segmented using a combination of open-source software Cellpose v2.1.0 (https://www.cellpose.org/) and Baysor v0.6.2 (https://github.com/kharchenkolab/Baysor). Filtering of low quality cells and mapping to scRNASeq taxonomy was performed using custom made scripts in R. Additional downstream analysis was conducted using custom scripts in R. All the analysis scripts used in this study, including examples using the tools mentioned above, are available at https://github.com/AllenInstitute/mouse_aging_scRNAseq.

For manuscripts utilizing custom algorithms or software that are central to the research but not yet described in published literature, software must be made available to editors and reviewers. We strongly encourage code deposition in a community repository (e.g. GitHub). See the Nature Portfolio guidelines for submitting code & software for further information.

Data

Policy information about availability of data

All manuscripts must include a data availability statement. This statement should provide the following information, where applicable:

- Accession codes, unique identifiers, or web links for publicly available datasets
- A description of any restrictions on data availability
- For clinical datasets or third party data, please ensure that the statement adheres to our policy

Primary and processed single cell RNA seq data have been deposited to the Neuroscience Multi-omic Data Archive (NeMO), https://nemoarchive.org/, and can be accessed at https://assets.nemoarchive.org/dat-61kfys3.
Primary spatial transcriptomics data have been deposited to Brain Image Library (BIL), https://www.brainimagelibrary.org/, and can be accessed at https://doi.org/10.35077/g.1157.

Research involving human participants, their data, or biological material

Policy information about studies with human participants or human data. See also policy information about sex, gender (identity/presentation), and sexual orientation and race, ethnicity and racism.

Reporting on sex and gender	This study does not involve human research participants.
Reporting on race, ethnicity, or other socially relevant groupings	N/A
Population characteristics	N/A
Recruitment	N/A
Ethics oversight	N/A

Note that full information on the approval of the study protocol must also be provided in the manuscript.

Field-specific reporting

Please select the one below that is the best fit for your research. If you are not sure, read the appropriate sections before making your selection.

☒ Life sciences ☐ Behavioural & social sciences ☐ Ecological, evolutionary & environmental sciences

For a reference copy of the document with all sections, see nature.com/documents/nr-reporting-summary-flat.pdf

Life sciences study design

All studies must disclose on these points even when the disclosure is negative.

Sample size	Sample size calculations were not performed. For scRNA-seq data and spatial transcriptomics data, sample size was determined based on extensive prior experience using these technologies in brain and resource availability, with balance in sex and age groups. The scRNA-seq data for each ROI were generated from 10-30 independent samples.
Data exclusions	Cells from scRNA-seq data and segmented cells from Resolve data that did not pass the QC processes described in Methods and supplementary tables were excluded.
Replication	The scRNA-seq data were generated from a total of 284 libraries from 96 animals, with multiple animals used for each of the 16 ROIs at each of the aged and adult age groups. The scRNA-seq data were obtained from at least two males and two females per ROI per age group, except for ROIs ACA (3M 1F in the adult group), PL-ILA-ORB (2M 1F in the adult group), and STRv (5M 1F in the adult group). The Resolve data were generated from at least 2 biological replicates per ROI per sex per age group.
Randomization	Randomization of animals to different groups was not relevant to our study design. There were no experimental vs. control groups.
Blinding	Experiments were not blinded in this study as all results presented are based on quantitative analysis and not subject to human biases.

Reporting for specific materials, systems and methods

We require information from authors about some types of materials, experimental systems and methods used in many studies. Here, indicate whether each material, system or method listed is relevant to your study. If you are not sure if a list item applies to your research, read the appropriate section before selecting a response.

Materials & experimental systems

n/a	Involved in the study
☒	☐ Antibodies
☒	☐ Eukaryotic cell lines
☒	☐ Palaeontology and archaeology
☐	☒ Animals and other organisms
☒	☐ Clinical data
☒	☐ Dual use research of concern
☒	☐ Plants

Methods

n/a	Involved in the study
☒	☐ ChIP-seq
☐	☒ Flow cytometry
☒	☐ MRI-based neuroimaging

Animals and other research organisms

Policy information about studies involving animals; ARRIVE guidelines recommended for reporting animal research, and Sex and Gender in Research

Laboratory animals	Laboratory animals Mus musculus, males and females, wild-type or Cre transgenic, in the C57BL/6J strain, in two age groups - adult (P53-P69) and aged (P540-P553).
Wild animals	This study did not involve wild animals.
Reporting on sex	For each brain ROI and each age, both male and female mice were used to collect scRNA-seq data.
Field-collected samples	This study did not involve field-collected samples.
Ethics oversight	All experimental procedures related to the use of mice were approved by the Institutional Animal Care and Use Committee of the Allen Institute for Brain Science, in accordance with NIH guidelines.

Note that full information on the approval of the study protocol must also be provided in the manuscript.

Plants

Seed stocks	This study does not involve plants.
Novel plant genotypes	N/A
Authentication	N/A

Flow Cytometry

Plots

Confirm that:

☒ The axis labels state the marker and fluorochrome used (e.g. CD4-FITC).

☒ The axis scales are clearly visible. Include numbers along axes only for bottom left plot of group (a 'group' is an analysis of identical markers).

☒ All plots are contour plots with outliers or pseudocolor plots.

☒ A numerical value for number of cells or percentage (with statistics) is provided.

Methodology

Sample preparation	Sample preparation was done according to protocols: Allen Institute for Brain Science 2021, Slice Preparation with Tissue Dissociation - Mouse Protocol. protocols.io https://dx.doi.org/10.17504/protocols.io.bq6wmzfe; and Allen Institute for Brain Science 2020, FACS Single Cell Sorting. protocols.io https://dx.doi.org/10.17504/protocols.io.be4cjgsw. Single cells were isolated by adapting previously described procedures. The brain was dissected, submerged in ACSF, embedded in 2% agarose, and sliced into 350-µm coronal sections on a compresstome (Precisionary Instruments). Block-face images were captured during slicing. Regions of interest (ROIs) were then microdissected from the slices and dissociated into single cells as previously described. Fluorescent images of each slice before and after ROI dissection were taken at the

dissection microscope. These images were used to document the precise location of the ROIs using annotated coronal plates of CCFv3 as reference.

Dissected tissue pieces were digested with 30 U/ml papain (Worthington PAP2) in ACSF for 30 minutes at 30°C. Due to the short incubation period in a dry oven, we set the oven temperature to 35°C to compensate for the indirect heat exchange, with a target solution temperature of 30°C. Enzymatic digestion was quenched by exchanging the papain solution three times with quenching buffer (ACSF with 1% FBS and 0.2% BSA). Samples were incubated on ice for 5 minutes before trituration. The tissue pieces in the quenching buffer were triturated through a fire-polished pipette with 600-µm diameter opening approximately 20 times. The tissue pieces were allowed to settle and the supernatant, which now contained suspended single cells, was transferred to a new tube. Fresh quenching buffer was added to the settled tissue pieces, and trituration and supernatant transfer were repeated using 300-µm and 150-µm fire polished pipettes. The single cell suspension was passed through a 70-µm filter into a 15-ml conical tube with 500 µl of high BSA buffer (ACSF with 1% FBS and 1% BSA) at the bottom to help cushion the cells during centrifugation at 100 x g in a swinging bucket centrifuge for 10 minutes. The supernatant was discarded, and the cell pellet was resuspended in the quenching buffer. We collected 1,508,284 cells without performing FACS. The concentration of the resuspended cells was quantified, and cells were immediately loaded onto the 10x Genomics Chromium controller.

To enrich for neurons or live cells, cells were collected by fluorescence-activated cell sorting (FACS) (BD FACSAria II or FACSAria Fusion, running FACSDiva v8 software) using a 130-µm nozzle. Neuronal enrichment was achieved by sorting RFP+ cells from Snap25-IRES2-Cre/wt;Ai14/wt transgenic mice counterstained with DAPI to exclude dead or dying cells. To enrich for live cells, samples were stained and sorted for Hoechst+ or Calcein+/Hoechst+ signal. Cells were prepared for sorting by passing the suspension through a 70-µm filter. Sorting strategy was as previously described (Tasic et al 2018). 30,000 cells were sorted within 10 minutes into a tube containing 500 µl of quenching buffer. We found that sorting more cells into one tube diluted the ACSF in the collection buffer, causing cell death. We also observed decreased cell viability for longer sorts.

Instrument	FACSAria II or FACSAria Fusion
Software	FACSDiva v8
Cell population abundance	Abundance of sorted cell populations for 10x scRNA-seq were determined by hemocytometer post-FACS.
Gating strategy	For sorting RFP+ cells, the morphology gate (SSC-A vs FSC-A) included all events that passed FSC threshold to allow profiling of all possible RFP+ cells. SC-FSC and SC-SSC were used to exclude doublets, and RFP+ cells were sorted from the rest of the cells based on the RFP+ DAPI- phenotype. Gating strategy for RFP+ mouse neurons is described in more detail here: Allen Institute for Brain Science 2020, FACS Single Cell Sorting, protocols.io https://dx.doi.org/10.17504/protocols.io.be4cjgsw. Live cells were sorted using a similar strategy. The morphology gate included all events that passed FSC threshold to allow profiling of all possible live cells. SC-FSC and SC-SSC were used to exclude doublets, and live cells were sorted from the rest of the cell population based on the Hoechst+ or Calcein+/Hoechst+ phenotype.

☒ Tick this box to confirm that a figure exemplifying the gating strategy is provided in the Supplementary Information.